Slope and shelf processes associated with upwelling in the northern California Current system

Thomas P. Connolly

A dissertation
submitted in partial fulfillment of the
requirements for the degree of

Doctor of Philosophy

University of Washington

2012

Reading Committee:

Barbara M. Hickey, Chair

Parker MacCready

Neil S. Banas

Program Authorized to Offer Degree:
UW School of Oceanography

University of Washington

Abstract

Slope and shelf processes associated with upwelling in the northern California Current system

Thomas P. Connolly

Chair of the Supervisory Committee:
Professor Barbara M. Hickey
School of Oceanography

The northern California Current system (CCS) experiences relatively weak upwelling-favorable wind stress during summer months, but high nutrient concentrations and hypoxic conditions occur seasonally. This study examines 1) the relative contribution of physical and biological processes to seasonal dissolved oxygen (DO) declines, 2) the role of coastal trapped waves in setting up the California Undercurrent (CUC) and a poleward alongshelf pressure-gradient force over the slope, 3) the role of submarine canyons in the upwelling of water from the slope onto the shelf.

The physical processes of upwelling and changes in source water contribute to interannual variability in hypoxic conditions, but cannot solely account for seasonal oxygen decreases. Mass balances of DO and nitrate show that biochemical processes in the water column and sediments each contribute ∼50% to the total consumption of DO in near-bottom water. Alongshelf advection of sharp gradients induced by localized respiration leads to variability at event (2–10 d) time scales on the inner shelf.

The dynamics of the CUC and alongshore pressure gradient over the slope are explored using the Navy Coastal Ocean Model and a linear coastal trapped wave model. In the linear model, alongshore winds drive poleward flow events over the slope, but a persistent undercurrent in the northern CCS is dependent on the use of San Diego sea level at the southern boundary. In the northern CCS, alongshore density gradients over the slope lead to a pole-

ward pressure-gradient force within the undercurrent that often opposes an equatorward force associated with coastal sea level.

To examine how water is transported from the slope to the shelf, a regional model hindcast is used to isolate the dynamics and impacts of canyon upwelling. Canyon upwelling occurs during periods of southward flow over the shelf which occur throughout the upwelling season. Water is transported from depths of ∼150–250 m over the slope to the near-bottom water at mid shelf. Canyon-enhanced fluxes in the bottom portion of the water column are large enough to influence changes in salinity over the shelf at seasonal time scales.

TABLE OF CONTENTS

LIST OF FIGURES

LIST OF TABLES

ACKNOWLEDGMENTS

I sincerely thank Barbara Hickey for her support and high level of involvement in my graduate research. As an advisor, she has encouraged me to pursue important and interesting topics, and has also challenged me every step of the way with her extensive level of knowledge and experience. Her open mind has allowed my research to span a broad range of techniques and disciplines. Her careful and consistent approach has been a fine example, and I know that working with her has provided me with a solid foundation to become a successful scientist.

I have also benefited immensely from the involvement of my reading committee. Working with Parker MacCready has greatly improved my knowledge of fluid dynamics, skills in numerical modeling and approach to formulating and tackling scientific questions. The modeling tools that he has developed over the years have allowed me and other students to avoid many pitfalls and take on ambitious projects. Neil Banas is a relatively new member of my committee, but inspired me to learn more about biological modeling and graphical presentation of scientific results early in graduate school. He has also been an important contributor to the tools that I have used in numerical modeling.

Evelyn Lessard has been a valuable member of committee because of her genuine interest in physical processes which leads her to ask the fundamental, although sometimes difficult, questions. She has been a great person to work with on cruises and learn from in the discussions that take place at project meetings. Cliff Mass not only took time to be the GSR on my committee, but has also taught me and many others a great deal about regional atmospheric processes through his extensive and successful outreach campaigns.

Working with Dr. Hickey has allowed me to become part of an excellent team of scientists who have assisted me throughout graduate school and taught me valuable skills that will stay with me throughout my career. Sue Geier and Nancy Kachel have amazed me with

their technical and scientific expertise. Their organization and dedication always ensures that everything gets done the right way. I would also like to thank Ryan McCabe and Amy MacFadyen for always taking time to discuss problem with me, even after their own graduations.

The coastal modeling group (a.k.a. MoSSea User Group or MUG), led by Parker MacCready, has been a valuable forum for discussion, sharing of tools and presentation of preliminary results. It has been a great experience to work with all of the post-docs that have contributed to the regional modeling effort: Yonggang Liu, Dave Sutherland, Sarah Giddings, Kristen Davis and Samantha Siedlecki.

Many individuals and groups, from the University of Washington as well as other institutions in the U.S. and Canada, contributed to the collection of data presented in this dissertation. Chapter 1 would not have been possible without the efforts of Jim Postel (UW) who originally compiled the historical data set, Nancy Kachel (UW) who was responsible for cruise logistics and processing hydrographic data, Katherine Krogslund and Aaron Morello (UW) who assisted with DO samples and Julian Herndon (RTC/SFSU) who performed and processed all the nutrient analyses. Previous measurements and analyses of sediment fluxes over the Washington shelf and slope by Al Devol (UW) and colleagues formed were extremely valuable. Chapters 2 and 3 greatly benefited from the availability of mooring data from the British Columbia slope and Washington shelf. Mooring data from the A1 site was provided by Richard Thomson (IOS), who has performed the remarkable feat of maintaining a mooring at this location for over 20 years. Dr. Thompson's group also participated in the collection of ECOHAB-PNW mooring data. Sue Geier (UW) was responsible for processing of ECOHAB-PNW moored data and also handled many of the logistics of deployment and recovery. RISE mooring data was provided by Edward Dever (OSU). Finally, special thanks is extended to the entire sea-going ECOHAB-PNW and RISE teams who were responsible for the massive data collection efforts on multiple cruises.

Numerical modeling work presented here also benefited from the hard work of many scientists. Kenneth Brink (WHOI) provided software for calculating the structure and

properties of coastal trapped wave modes used in Chapter 2. Igor Shulman (NPS) provided NCOM model output, which is analyzed extensively in Chapter 2 and used for open boundary conditions in Chapter 3. For the model used in Chapter 3, Cliff Mass (UW) provided output from the regional MM5 model for atmospheric forcing and Mike Foreman (IOS) provided the inputs for tidal forcing. Parker MacCready (UW) and Dave Sutherland (UO) provided MoSSea model output for the eastern boundary in the Strait of Juan de Fuca, in addition to their invaluable assistance and support in using ROMS. This study used bathymetric data compiled and processed by USGS, as well as the CCMP wind product developed by NASA.

The work presented in this dissertation was supported by numerous research grants and fellowships. Research for Chapter 1 was supported by the PNW Center for Human Health and Ocean Sciences (National Institutes of Health (NIH)/National Institute of Environmental Health (NIEHS): P50 ES012762 and National Science Foundation (NSF): OCE 0434087), by the Coastal Ocean Program of the National Oceanic and Atmospheric Administration (NOAA) (NA17OP2789) and NSF (OCE 0234587) as part of the ECOHAB-PNW project. Additional support was provided by NOAA (NA17RJ1232) as part of the GLOBEC Northeast Pacific program. Mooring data were collected under National Marine Sanctuary Permits OCNMS-2003-002 and OCNMS-2006-004. RISE data were collected with support from NSF (OCE 0239089). Research for Chapters 2 and 3 was supported by grants from the NOAA Coastal Ocean Program (NA09NOS4780180) and NSF (OCE0942675) as part of the PNWTOX (Pacific Northwest Toxin) project. One academic quarter of graduate study was supported by a Theodore and Marie Sarchin fellowship. One year of graduate study was supported by a fellowship from the American Meteorological Society, sponsored by the Office of Naval Research.

Finally, I would also like to thank my office-mates in OSB 343 for creating a pleasant and productive work environment throughout graduate school: Sally Warner, Noel Pelland, Nick Beaird and Mark Carson. Enjoying the company of the people you see every day cannot be taken for granted. I look forward to seeing, and hopefully working with, all of

them in the future.

Most of all, I would like to thank Colleen Durkin for being with me every step of the way during graduate school, and continuing the journey with me to the east coast.

INTRODUCTION

The continental shelves of Oregon, Washington and British Columbia are situated in the northern California Current system (CCS), a region of high seasonal productivity that serves as a confluence of water masses from across the Pacific Ocean. Primary productivity in this region is associated with high chlorophyll-*a* concentrations (Perry et al., 1989), which in turn has been linked to high levels of zooplankton biomass and fish yield (Ware and Thomson, 2005). However, the deep upwelled water that provides high concentrations of macronutrients to the surface is also associated with low concentrations of dissolved oxygen and high partial pressures of CO_2, which can have detrimental effects on marine organisms through hypoxia and dissolution of calcite structures in low-pH waters. High productivity has long been associated with coastal upwelling regions such as the CCS (Ryther, 1969), but productivity in the northern CCS is relatively high in spite of the fact that local upwelling wind stress is relatively weak (Hickey and Banas, 2008). Distributions of nutrients, dissolved gases and other tracers are strongly linked to physical dynamics near the coast, as well as broader scales over the ocean gyres. The research presented herein focuses on processes that influence water properties in the subsurface water column, below the euphotic zone, in the northern CCS: physical and biochemical processes associated with hypoxia (Chapter 1), dynamics of the large-scale California Undercurrent (Chapter 2), and exchange between continental slope and shelf (Chapter 3).

The California Current system (CCS) encompasses the coastal regions of North America from British Columbia to Baja California, and extends offshore into the eastern limb of the clockwise subtropical gyre in the North Pacific. The California Current itself flows southward throughout the year and its offshore boundary is often taken to be ∼1000 km offshore of the coast (Hickey, 1979; Strub and James, 2000). This area is characterized by greater variability in the dynamic height of the sea surface compared with locations further in the interior of the gyre (Wyrtki, 1975). In addition to the strong southward coastal

currents present over the shelf, a maximum in the southward flow in the California Current is present ∼500 km offshore and varies seasonally with the local wind stress curl (Hickey, 1979).

Subarctic water is transported into the northern end of the CCS by the West Wind Drift, which flows across the North Pacific along the boundary between the subarctic and subtropical gyres. Subarctic water, subducted into the ocean interior at higher latitudes, is generally characterized by low salinity, cold temperatures and high dissolved oxygen at a given density (Lynn and Simpson, 1987). In the density range σ_t = 26.5–26.7, which is found over the upper slope and outer shelf in the northern CCS, decadal variability and long-term trends in dissolved oxygen have been observed in the subarctic water of the North Pacific (Emerson et al., 2004; Whitney et al., 2007). Decadal variability has been associated with changes in the circulation and residence time of subarctic water (Deutsch et al., 2006), which may also be linked to observed long-term changes in dissolved oxygen at coastal locations in the northern CCS (Whitney et al., 2007; Pierce et al., 2012). Decreased ventilation due to anthropogenic warming is expected to further decrease dissolved oxygen in the subarctic North Pacific (Bopp et al., 2002; Frölicher et al., 2009). Such changes would also be associated with increased nitrate concentrations in the source waters for upwelling in the CCS, promoting increased primary productivity (Rykaczewski and Dunne, 2010). Associated increases in the partial pressure of CO_2 in the subarctic water would exacerbate the ecosystem impacts of increased CO_2 concentrations in the atmosphere.

Water mass characteristics in the northern CCS are also strongly influenced by the California Undercurrent, which flows northward over the upper continental slope from Baja California to Vancouver Island. The undercurrent transports water from the tropics, characterized by high salinity and high temperatures (Lynn and Simpson, 1987). Equatorial water is low in oxygen due to high productivity associated with equatorial upwelling and weak retentive circulation offshore of central America (Karstensen et al., 2008). Nutrient concentrations in this water mass are high, but denitrification in suboxic equatorial waters results in deviations from typical "Redfield" stoichiometry in California Undercurrent water (Castro et al., 2001). Modeled decadal variability in the volume of suboxic equatorial water has been linked to fluctuations in productivity associated with the strength of equatorial

upwelling and the Pacific Decadal Oscillation (Deutsch et al., 2011). This process qualitatively explains observed decadal variability in dissolved oxygen off southern California (McClatchie et al., 2010; Deutsch et al., 2011), suggesting that the California Undercurrent communicates climate-driven oxygen variability to coastal regions in the CCS. Although lateral mixing processes dilute the equatorial component of the water mass as it is transported northward, it still influences the northern CCS. Thomson and Krassovski (2010) estimate that the core of the undercurrent is composed of $\sim$40% equatorial water off the Washington coast. Although surface-intensified poleward flows also exist in the CCS (the Davidson current, and the inshore countercurrent in the Southern California Bight, e.g.) the California Undercurrent is associated with the most pronounced maximum in equatorial water mass properties (Lynn and Simpson, 1987).

Coastal currents in the CCS are largely driven by wind forcing near the coast, which varies spatially with latitude and temporally at weather-band, seasonal and interannual time scales. Equatorward winds in the CCS are associated with high atmospheric pressure over the ocean and lower atmospheric pressure over land. The high pressure system over the subtropical North Pacific is strongest during summer, a result of feedbacks between the ocean–land temperature difference and equatorward winds (Miyasaka and Nakamura, 2005). A thermal low pressure system over the warm, arid land of California is also strongest during summer. Wind stress during summer is favorable for upwelling throughout the California Current, and strongest at 39°N. The seasonal peak in upwelling-favorable wind stress occurs during July off Washington, and much earlier during April off Baja California (Hickey, 1979). During winter, the North Pacific high weakens and shifts southward. The Aleutian low pressure system, a seasonal mean signal associated with winter storm tracks, forms over the North Pacific ocean and southern Bering Sea. As a result, alongshore wind stress in the CCS is downwelling-favorable in the northern CCS during winter. In addition to alongshore variability, wind stress curl is also present throughout the system. Areas of strong positive wind stress curl are located near near Point Conception, where the coastline bends sharply, and near Cape Mendocino off northern California, where the strongest equatorward wind stress is located (Bakun and Nelson, 1991).

Like many other eastern ocean boundaries, wind-driven coastal upwelling associated

with equatorward wind stress is a central process in the physical dynamics. The most basic response of alongshore currents to upwelling-favorable wind stress near the coast is the generation of equatorward flow in geostrophic balance with low sea level near the coast, as described for a steady unstratified system by Ekman (1905). When stratification is present, the divergence of Ekman transport at the coast results in vertical velocity and an upward tilt of the pycnocline near the coast, as shown for a transient two-layer system by Yoshida (1955). Modeling of the two-dimensional upwelling problem, with no alongshore variability in wind stress, has been extended to include effects such as continuous stratification, non-linear dynamics and turbulence closure (Allen et al., 1995), yielding insights into the structure of the upwelling front and the depth of the onshore flow that compensates for surface Ekman transport. However, upwelling is a fundamentally three-dimensional process due to alongshore variations in wind stress, topography and freshwater input.

Models with alongshore variability in the wind field with scales typical of the CCS introduces a poleward alongshore pressure gradient and allows for the development of a poleward undercurrent, as shown for a two-layer system by Yoshida (1967) and a continuously stratified system by McCreary (1981). The modeled poleward flow is enhanced by positive wind stress curl and the β-effect (Philander and Yoon, 1982; McCreary and Chao, 1985). However, even though the undercurrent is a robust feature of models with large-scale structure in upwelling-favorable wind stress, numerous other mechanisms for the undercurrent have been proposed, as summarized by Hill et al. (1998). Thus, even as models of the CCS improve to the point where they can be used to study complex interdisciplinary problems such as coastal productivity and hypoxia, research is still needed clarify the forcing mechanisms for important transport pathways such as the California Undercurrent.

Exchange between the slope and shelf must be present for the low-oxygen, high-nutrient water properties of the California Undercurrent water to influence hypoxia and productivity over the continental shelf. The presence of California Undercurrent water on the shelf in the northern CCS has been demonstrated by water mass analysis (Mackas et al., 1987; MacFadyen et al., 2008). However, the mechanism for cross-isobath transport is not clear. Sloping topography inhibits the cross-shelf transport associated with steady flow, even when stratification is present (Brink, 1998). Low subinertial frequencies and large alongshore

scales make the alongshore currents associated with wind-driven currents approximately geostrophic. Since poleward flow is favorable for downwelling in the bottom boundary layer of the California Undercurrent, the breaking of geostrophy by friction does not provide a mechanism for transport onto the shelf. However, submarine canyons are locations where the alongshore length scale of the bathymetry becomes comparable to the cross-shore scale of the shelf width. When the alongshore length scale becomes small as in the case of canyons, geostrophic balance of the alongshelf flow breaks down and cross-shelf flow can become as large as the alongshelf flow (Trowbridge et al., 1998). Therefore submarine canyons are potentially sites of enhanced cross-isobath exchange betwen the slope and shelf, compared with locations where bathymetry is relatively uniform in the alongshelf location. However, the small alongshore scales and complex dynamics of submarine canyons make it challenging to gauge their impacts on surrounding shelf regions. It has been estimated that the flux of deep water through submarine canyons are an important component of nutrient supply to the continental shelves in the northern CCS (Hickey and Banas, 2008).

In addition to the complex physical dynamics associated with transport, the properties of subsurface waters can be influenced by biochemical processes associated with the high productivity of coastal regions such as the northern CCS. Blooms of phytoplankton result in sinking particles of organic matter that are broken down by bacteria below the euphotic zone. Aerobic respiration, either in the water column or in the sediments, consumes dissolved oxygen and produces both nitrate and CO_2. Studies of hypoxia must also consider respiration in sediments in order to model the magnitude and location of changes in dissolved oxygen and nitrate (Hetland and DiMarco, 2008; Bianucci et al., 2011). These non-conservative processes introduce further spatial and temporal complexity on top of the multi-scale physical problems of water mass transport and upwelling dynamics, and must be addressed in interdisciplinary studies of hypoxia, ocean acidification and coastal productivity.

In Chapter 1 (Connolly et al., 2010), observations are used to distinguish between the physical and biochemical processes that contribute to the seasonal reduction in dissolved oxygen concentrations. Analysis of historical data indicates that dissolved oxygen concentrations well below typical definitions of hypoxia are a common feature associated with the

productive waters of the northern CCS. Non-conservative consumption of DO over the shelf is estimated by comparing dissolved oxygen with tracers that are conserved in the subsurface water column, such as salinity and temperature. It is shown that between July and September, after isopycnals have transitioned to the summer state of tilting upward toward the coast, respiration dominates the seasonal decrease in dissolved oxygen during late summer. Alongshore gradients associated with patches of high dissolved oxygen consumption contribute to variability on the inner shelf, where alongshore currents respond most quickly to local upwelling favorable winds. Deviation of nitrate and dissolved oxygen concentrations from the ratios expected during aerobic respiration of organic matter are used to show that respiration in sediments are an important part of the decrease. Interannual variability is associated with both the strength of upwelling favorable winds, and the contribution of regional water masses such as the California Undercurrent.

In Chapter 2, dynamics of the California Undercurrent in the northern CCS are investigated at seasonal and higher-frequency time scales. In order to identify the most important processes, two numerical models are used: a complex non-linear model that is designed to be as realistic as possible, and a simplified linear model that is designed to capture the effects of alongshore variability associated with coastal trapped waves. Unlike previous studies of the undercurrent, the models are validated by comparing with time series of velocity within the core of the undercurrent. Both models are able to reproduce event scale variability in the undercurrent, as well as the seasonal cycle of equatorward flow during spring and poleward flow during late summer and fall. However, the presence of a persistent undercurrent in the linear model is dependent on the southern boundary condition, which incorporates sea level at San Diego. This implies that the seasonality of the undercurrent is either linked to larger scale processes, or dynamics that are missing from the simple model such as wind stress curl or the variation of the Coriolis parameter with latitude. In both models, the structure of the mean alongshore pressure gradient during summer is found to vary with latitude, depth and distance offshore. Near the coast, the modeled sea surface slopes downward towards the north through most of the CCS as described by Hickey and Pola (1983), and either weakens or slopes upward to the north in the northern CCS. Over the slope, where alongshore pressure gradients are difficult to observe, the upward displacement of isopycnals

peaks at ∼42°N off southern Oregon, north of the strongest upwelling favorable wind stress. North of this latitude, alongshore density gradients allow for a baroclinic poleward pressure gradient force at undercurrent depths. Further south, the direction of the alongshore pressure gradient is determined by the sloping of the sea surface. This structure is similar to that predicted by the early studies of Yoshida (1967) and McCreary (1981), and places the northern CCS in a dynamical regime similar to the regions poleward of the wind stress in their idealized scenarios.

Chapter 3 addresses the problem of shelf-slope exchange in the northern CCS. A regional numerical model is developed that resolves the complex topography of the region and includes realistic atmospheric forcing and boundary conditions in a hindcast of summer 2005, when an extensive observational data set is available for validation. Modeled circulation near submarine canyons is found to be consistent with previous observations in the region. Fluctuations in density near canyon heads are correlated with fluctuations in the equatorward coastal jet, and closed cyclonic eddies form at the depth of the canyon rims. Passive particles and tracer budgets are used to demonstrate the impact of submarine canyons on shelf-slope exchange. Passive particles are preferentially upwelled onto mid shelf near canyons. Canyons allow for source depths of mid-shelf particles that are deeper than the shelf break depth, which does not occur elsewhere. Salt budgets on the Washington and British Columbia shelves are three-dimensional, but show that cross-isobath fluxes over the shelf are important for determining the total increase in salinity over the shelf during summer. These fluxes are associated with offshore transport of relatively fresh water in the surface Ekman layer, and onshore transport of relatively salty water just above the depth of the shelf break. The onshore flux of deep water is confined to the south sides of canyons and topographic depressions. Cross-shelf momentum balances indicate that ageostrophic forces directed across isobaths are associated with momentum advection. Submarine canyons therefore provide a way to break the constraints of geostrophy over the continental slope, allowing for significant fluxes across the shelf break, including water masses associated with the California Undercurrent.

Chapter 1

PROCESSES INFLUENCING SEASONAL HYPOXIA IN THE NORTHERN CALIFORNIA CURRENT SYSTEM[1]

Abstract

This chapter delineates the role of physical and biological processes contributing to hypoxia, or low dissolved oxygen (DO) < 1.4 mL L^{-1}, over the continental shelf of Washington State in the northern portion of an eastern boundary system, the California Current System (CCS). In the historical record (1950–1986) during the summer upwelling season, hypoxia is more prevalent and severe off Washington than further south off northern Oregon. Recent data (2003–2005) show that hypoxia over the Washington shelf occurred at levels previously observed in the historical data. 2006 was an exception, with hypoxia covering $\sim$5000 km^2 of the Washington continental shelf and DO concentrations below 0.5 mL L^{-1} at the inner shelf, lower than any known previous observations at that location. In the four years studied, upwelling of low DO water and changes in source water contribute to interannual variability, but cannot account for seasonal decreases below hypoxic concentrations. Deficits of DO along salinity surfaces, indicating biochemical consumption of DO, vary significantly between surveys, accounting for additional decreases of 0.5–2.5 mL L^{-1} by late summer. DO consumption is associated with denitrification, an indicator of biochemical sediment processes. Mass balances of DO and nitrate show that biochemical processes in the water column and sediments each contribute $\sim$50% to the total consumption of DO. At shorter than seasonal time scales on the inner shelf, alongshelf advection of hypoxic patches and cross shelf advection of seasonal gradients are both shown to be important, changing DO concentrations by 1.5 mL L^{-1} or more over five days.

---

[1]Connolly, T. P., B. M. Hickey, S. L. Geier, and W. P. Cochlan, Processes influencing seasonal hypoxia in the northern California Current System, *J. Geophys. Res.*, *115*, C03021, 2010.

1.1 Introduction

Recent time series studies in the Northeast Pacific have found long-term decreases in dissolved oxygen (DO) at oceanic and neritic locations (Whitney et al., 2007; Bograd et al., 2008). Such a broad-scale trend could intensify impacts of low DO (or "hypoxic") events in the northern California Current system, particularly over the inner continental shelf (Grantham et al., 2004; Chan et al., 2008). Coastal upwelling regions along eastern boundaries like the California Current system (CCS) receive high inputs of nutrients from depth and are characterized by high rates of primary productivity (Ryther, 1969; Pauly and Christensen, 1995). Organic matter degradation in the water column and sediments consumes DO in near bottom water, but differences in near bottom DO concentrations between different regions, and between seasons, can also be influenced by physical processes. Before long term impacts can be adequately modeled and even forecasted, it is necessary to understand past conditions and the processes that contribute to hypoxia.

In this paper, historical data (1950–1986) are used to describe local and regional patterns in the timing and severity of hypoxia off the coasts of Washington and Oregon. Recent interdisciplinary survey data from the Washington shelf (2003–2006) are used to assess the relative contributions of seasonal upwelling, interannual source water variability and biochemical consumption of DO in both the water column and sediments. The importance of alongshelf and cross-shelf advection in response to wind events over the inner shelf is assessed using data from moored sensors.

The continental shelf of Washington (Fig. 1.1) is located in the northern CCS. The seasonal cycle of upwelling favorable wind stress peaks in summer, though downwelling and relaxation events still occur throughout this season (Hickey, 1979, 1998). During the annual spring transition, oceanographic conditions change over the course of several days to weeks from the mean winter state of predominantly poleward flow and level isopycnals to the mean summer state of predominantly equatorward flow and isopycnals that tilt upward towards the coast (Strub et al., 1987). Previous studies have shown that, like all other water properties, DO concentrations exhibit strong seasonality in this region (Landry et al., 1989). Seasonal minima in subsurface DO concentrations over the Washington and Oregon

shelves, in the bottom depth range 70–130 m, are coincident with denser water and high macro-nutrients. The permanent oxygen minimum zone in the North Pacific, where pelagic DO concentrations fall below 0.5 mL L^{-1}, intersects the slope between depths of ∼600–1300 m (Sverdrup et al., 1942), well below the source of upwelled water. Though dissolved oxygen concentrations have been related to hypoxia on the Oregon shelf (Grantham et al., 2004; Hales et al., 2006; Chan et al., 2008), previous descriptions of DO concentrations on the Washington shelf have not discussed hypoxia.

The magnitude and direction of coastal currents vary with distance from shore and depth from the bottom. A baroclinic equatorward coastal jet is present over the shelf throughout the summer and the poleward California Undercurrent develops at the shelf break and slope during late summer to early fall (Hickey, 1979, 1989). The California Undercurrent is characterized by relatively warm, high salinity, low DO equatorial water (Hickey, 1979; Lynn and Simpson, 1987). Over the inner shelf, the surface and bottom Ekman layers interact, allowing for divergence of cross shelf transport and, consequently, upwelling and downwelling (Lentz, 1995). Poleward flow is more common on the inner shelf than on the mid and outer shelf, especially near the bottom (Hickey, 1989). In the cross shelf direction, current meter observations have shown that the onshore flow compensating for offshore Ekman transport often occurs in the interior region away from the bottom boundary layer, both in mean summer profiles and during individual upwelling events (Smith, 1981; Huyer, 1983; Hickey, 1989).

Mesoscale features are an important source of spatial variation in the alongshelf direction in the northern CCS. Fresh water from the Columbia River influences both the Washington and Oregon shelves during summer (Hickey et al., 2005, 2010), though nutrient concentrations in the plume are typically low compared with upwelled water (Hill and Wheeler, 2002; Bruland et al., 2008). Juan de Fuca canyon separates the Washington shelf from the British Columbia shelf, and the cyclonic Juan de Fuca eddy appears as a persistent summer feature with ∼50 km horizontal scale (Freeland and Denman, 1982; MacFadyen et al., 2005, 2008). Off Oregon, Heceta Bank deflects the summertime equatorward coastal jet offshore, with increased retention on the south side of the bank closer to shore (Castelao and Barth, 2005; Barth et al., 2005).

The term "hypoxia" describes low DO conditions, defined here as concentrations < 1.4 mL L^{-1} ($= 2$ mg $L^{-1} = 62.5$ μM $\sim 20\%$ saturation for S = 32 psu and T = 7°C), that can potentially cause physiological stress in marine organisms. In general, the ecosystem impacts of hypoxia vary depending on the typical seasonal cycle of DO, the persistence of hypoxic conditions, and the types of organisms at a specific location (Davis, 1975; Diaz and Rosenberg, 1995). Diaz and Rosenberg (1995) suggest that, in areas with strong seasonality, mortality begins when DO concentrations fall below 1.0 mL L^{-1} and mass mortality occurs at concentrations less than 0.5 mL L^{-1}. Fish and crustaceans may be able to avoid hypoxic regions, but are typically less tolerant to low oxygen concentrations than annelids or bivalves, especially during prolonged hypoxic conditions (Gray et al., 2002). Inner shelf near bottom water in the northern CCS provides habitat for commercially important species such as Dungeness crabs and English sole (Botsford et al., 1989). Here, we define "severe hypoxia" as 0.5 mL L^{-1}, consistent with Chan et al. (2008).

Depletion of DO in hypoxic environments can be caused by biochemical consumption in the water column and within the bottom sediment. Isolating water column and sediment sinks in a regional numerical model can greatly affect the vertical structure of DO in the water column and the location of hypoxia over the shelf, as shown for the Gulf of Mexico by Hetland and DiMarco (2008). Surface sediment over the Washington shelf is characterized by a north-northwest oriented silt deposit of Columbia River origin that lies between the 60 and 120 m isobath at the latitude of Grays Harbor, and sandy sediment on the inner shelf which is part of a transgressive layer formed by rising sea levels (McManus, 1972; Nittrouer, 1978). On the mid to outer shelf, irrigation by benthic infauna enhances fluxes of DO from near bottom water to sediments (Archer and Devol, 1992; Devol and Christensen, 1993). Aerobic respiration and oxidation of reduced inorganic species both contribute to sedimentary oxygen demand. Anaerobic forms of respiration, such as denitrification, also occur in the pore waters of shelf sediments. Denitrification consumes nitrate rather than oxygen and does not occur in the water column unless DO concentrations are suboxic, less than 0.1–0.2 mL L^{-1} (Codispoti et al., 2005). On the Washington shelf, aerobic respiration and denitrification both take place in the upper 10 mm of the sediments, primarily in discrete sites surrounding particles of organic matter (Brandes and Devol, 1995). Fluxes of both DO and

nitrate during summer, measured using benthic flux chambers, are always directed into the sediment (Devol and Christensen, 1993; Hartnett and Devol, 2003). Stoichiometric evidence for denitrification is therefore a potential indicator of sedimentary DO consumption.

In this paper, we first describe the available data sets (Section 1.2), followed by the historical (1950–1986) spatial and temporal distribution of hypoxia in the bottom water of the northern CCS (Section 1.3). Next, recent survey data (2003–2006) are used to describe spatial distributions of late summer near bottom DO and corresponding seasonal wind forcing conditions (Section 1.4.1). Hydrographic data from this time period are used to evaluate the contribution to the seasonal evolution of hypoxia by a) upwelling; b) variability of DO in source waters; c) biochemical DO consumption; and d) the specific role of sedimentary DO consumption (Section 1.4.2). Last, the higher frequency response of DO to event scale physical forcing over the inner shelf is examined using time series from moored DO sensors (Section 1.4.3). In the final section, we relate our results to previous studies in the California Current system and other upwelling systems.

1.2 Data

1.2.1 Historical water property data

Historical data for the Washington and Oregon continental shelves from the years 1950–1986 were obtained from archived data at the University of Washington and from the National Oceanographic Data Center's World Ocean Database (Boyer et al., 2006). Bottom depths in the historical data, if not recorded, were determined by interpolating from the National Geophysical Data Center 3 arc-second US coastal relief model (Divins and Metzger, 2008). Stations with large discrepancies between recorded bottom depth and the interpolated topography (20 m + 20% of interpolated value) were discarded from the analysis. A summary of hydrographic data collected in the region during this time period is given by Landry et al. (1989). DO measurements were determined by Winkler titration, accurate to ∼0.1% under ideal experimental conditions (Carpenter, 1965a). However, Carritt and Carpenter (1966) have demonstrated the potential for significant analytical errors through the mid-1960s, ±1 mL L^{-1} at high saturated concentrations (∼5 mL L^{-1}) and overestimation by 100% or

greater at low concentrations ($\sim$0.2 mL L^{-1}).

1.2.2 Recent water property data

During the summers of 2003–2006, temperature (T), salinity (S) and DO data were obtained in the northern CCS as part of two multidisciplinary programs: ECology and Oceanography of Harmful Algal Blooms Pacific Northwest (ECOHAB-PNW) and River Influences on Shelf Ecosystems (RISE) programs (Table 1). Data are available between 44°26'N and 49°08'N for the ECOHAB-PNW cruises, and between 46°15'N and 47°50'N for the RISE cruises. This study primarily uses ECOHAB-PNW data from the Washington shelf between Juan de Fuca Canyon and Grays Harbor (see study area, Fig. 1); RISE data are included for a repeated Grays Harbor transect (GHR, Fig. 1). Maximum cast depths were typically 500 m during ECOHAB-PNW cruises and 200 m during RISE cruises. All hydrographic data from these cruises were collected with a calibrated Sea-Bird Electronics (SBE) 911*plus* conductivity, temperature and depth (CTD) system. Samples for chlorophyll *a* (Chl *a*) were collected in Niskin bottles attached to the instrumented rosette, and Chl *a* determined using non-acidification in vitro fluorometric analysis (Welschmeyer, 1994) after filtration onto Whatman GF/F filters (0.7 μm nominal pore size). Inorganic nutrient samples were collected in polypropylene tubes from rosette bottles and analyzed using a flow injection Lachat autoanalyzer for nitrate plus nitrite ($NO_3^- + NO_2^-$, hereafter referred to as nitrate or "N") and ortho-phosphate (PO_4^{3-}), hereafter referred to as phosphate or "P") (Smith and Bogren, 2001; Knepel and Bogren, 2002).

Recent DO data were primarily obtained with profiling SBE 43 sensors. During the September 2006 EH6 cruise, sensor measurements of DO were compared to bottle concentrations determined by Winkler titration (Carpenter, 1965b). Residuals between the in situ calibration and the factory calibration one year earlier are -0.05, 0.05, 0.12, and 0.35 mL L^{-1} at 0, 1, 2, and 5 mL L^{-1}, respectively (Fig. a). Data from the R/V Wecoma during summer 2005 were corrected using a linear regression of sensor and Winkler titration values presented in Lohan and Bruland (2008). Factory calibrations from successive cruises on the R/V Wecoma (Seabird Electronics, Bellevue, USA) resulted in small corrections at low

concentrations, with residuals of 0.08, 0.21, and 0.68 mL L^{-1} for DO values of 1, 2, and 5 mL L^{-1}, respectively.

To improve the accuracy of the data from ECOHAB-PNW cruises 1–5, sensors that were not calibrated in situ have been adjusted using stations seaward of the shelf in the historical data set. The mean and standard deviation of DO at temperatures in increments of 0.4°C were calculated for each recent cruise, and for each month in the historical data, at stations with bottom depth >1000 m for data between 42°N and 49°N and east of 126°W. Least-squares linear regressions of mean DO values, at temperatures where the standard deviation of DO did not exceed 0.25 mL L^{-1} in the recent or historical measurements, were then used to correct the sensor data; coefficient of determination values, r^2, were ≥ 0.995 for these relationships during each cruise. To reveal possible biases, the regression obtained from this method was compared with the in situ calibration obtained during the September 2006 EH6 cruise (Fig. 1.2b). Differences between the two methods were 0.05, 0.02, and 0.09 at DO concentrations of 1, 2, and 5 mL L^{-1}, respectively. A different SBE 43 sensor, also calibrated with bottle samples, gave nearly identical results, (historical = 0.965 × calibrated + 0.06 mL L^{-1}) during a cruise in July 2007 (not shown or used in the results presented here). Intercepts at 0 mL L^{-1} ranged from −0.04 to 0.06 mL L^{-1}, consistent with factory and in situ calibrations.

1.2.3 Moored sensors

Moored sensors were deployed on the Washington shelf as part of the ECOHAB-PNW program during summer and early fall of 2005 and 2006 in water depths ∼45 and 35 m (E2, E4, see Fig. 1). At E2, temperature, conductivity and fluorescence were sampled near the surface (4 m). At E4, temperature, conductivity, pressure, fluorescence and DO were sampled 3 m above bottom (32 m). An SBE 16*plus* measured temperature and conductivity; a WETLab ECO-FL measured fluorescence and an SBE 43 measured DO. Fluorescence was converted to units of Chl *a* concentration (μg L^{-1}) using factory calibrations. Mooring fluorescence are compared to bottle samples of Chl *a* and/or shipboard fluorescence profiles that have been calibrated with bottle samples when possible ($r^2 = 0.59$, $n = 585$

during EH5; $r^2 = 0.78$, $n = 769$ during EH6). Velocity profiles with 2 m spacing were obtained from an upward looking Teledyne RD Instruments Workhorse Sentinel acoustic Doppler current profiler (ADCP) positioned 9 m above bottom (28 m) on the E4 mooring. Unless otherwise stated, all water property and velocity data were low-pass filtered using a cosine-Lanczos filter with a half power point of 46 hr in order to remove tidal and other higher frequency signals. ADCP data were rotated into a coordinate system in which the alongshelf, y (cross-shelf, x), direction has been aligned with the local isobath direction, 20 degrees counterclockwise from true north. The sensitivity of results to this coordinate system rotation will be addressed.

To assess whether biofouling affected moored DO sensors, shipboard DO profiles were obtained within 100 m of the mooring site during 2006. Calibrated shipboard sensor DO concentrations exceeded mooring sensor DO concentrations by 0.15 to 0.31 mL L^{-1} in three separate casts at the mooring site over a two week period. The residuals (ship - mooring) are likely attributable to DO gradients in the 1 to 2 m vertical distance separating the two sensors. The largest of these residuals occurred when vertical gradients of 0.3 to 0.5 mL L^{-1} m^{-1} were observed near the bottom (not shown). In 2005, residuals from the nearest stations occupied (located 4.8, 3.6, and 11.4 km from the E4 mooring, respectively) ranged from -0.16 to 0.75 mL L^{-1}, with the highest residuals occurring during periods of rapid temporal changes and small residuals -0.1–0.1 mL L^{-1} occurring over two months after deployment. DO sensors on the moorings did not suffer from serious biofouling; large residuals >0.2 mL L^{-1} between mooring and shipboard measurements result from their vertical and horizontal separation.

1.2.4 Calculation of spatial gradients in DO

Data from CTD surveys and moorings were used to calculate horizontal gradients of DO (ΔDO/Δy, ΔDO/Δx). Cross shelf gradients were calculated from pairs of CTD stations. Alongshelf gradients were calculated from near-simultaneous shipboard near bottom measurements and values from the filtered mooring time series. To remove errors due to vertical gradients between the depths of the shipboard sensor and the mooring sensor, casts with

vertical DO gradients greater than 0.1 mL L^{-1} m^{-1} at the bottom of the cast were excluded from the alongshore analysis. However, contamination by cross shelf variations in DO may still be present. Differences between remaining shipboard measurements and values from the filtered mooring time series cover a range up to 0.5 mL L^{-1} as alongshelf distance approaches zero, with shipboard estimates being higher in most cases (not shown). An error estimate E = (0.5 mL L^{-1})/Δy, where Δy is alongshelf distance, represents the potential bias in calculations of alongshelf gradients and will be shown as error bars on appropriate figures.

1.2.5 Wind

Hourly wind speed and direction were obtained from the National Data Buoy Center buoy off Cape Elizabeth, Washington (46041, B41; Fig. 1.1). These data were rotated into the same coordinate system as the velocity measurements. Alongshore wind stress was computed using the drag coefficient from Large and Pond [1981]. These time series were subsequently low pass filtered and decimated in the same manner as the velocity measurements. As a supplement to direct wind measurements, seasonal wind forcing is described using an upwelling index (1967–2006, www.pfeg.noaa.gov), a measure of offshore Ekman transport computed from gridded atmospheric pressure fields (Bakun, 1973; Schwing et al., 1996). A cumulative upwelling index (CUI) was obtained by integrating daily upwelling index values over the climatological upwelling season 27 April to 26 September (Schwing et al., 2006). An alternative method of calculating summer CUI, integrating from the spring minimum of the annual CUI (Pierce et al., 2006), was also utilized.

1.3 Hypoxia in the historical data record

The historical record of near bottom DO over the continental shelf covers a broad geographic region (Fig. 1.1). Because the physical setting varies with cross shelf location, data were separated into three bottom depth ranges: the inner shelf (0–40 m), mid shelf (40–80 m) and outer shelf (80–130 m). The 40 m isobath boundary between the inner shelf and mid shelf was chosen based on the principle axis orientation of velocity time series over the Washington shelf in 2005 and 2006 (not shown). An interior region, with no counterclockwise veering of

the principle axes with depth, was present at E2 (45 m) but not at E4 (35 m), indicating that the boundary layer interaction is restricted to the region inshore of the 45 m isobath. Over the Oregon shelf we use the same 40 m isobath inner shelf boundary, consistent with the cross shelf transport calculations of Kirincich et al. (2005). Historical near bottom DO data from the inner shelf of Oregon are limited to 59 stations, mostly concentrated on the northern Oregon shelf where the shelf width transitions from broad to narrow, compared with 266 stations over the Washington inner shelf.

The historical data show that low DO in bottom water (10 m from the bottom or less) has occurred in the past over a broad region on northern CCS shelves (Fig. 1.1), in particular, over much of the Washington shelf. Off the Washington coast, nearly all hypoxic stations occur south of Quinault Canyon. On the southern half of the Washington shelf, from the Copalis Beach line to the Columbia River mouth, hypoxic bottom water has been observed across the entire width of the shelf. Over the northern Oregon shelf, hypoxic bottom water has been observed at several sites on the outer and mid shelf, but at only one station on the inner shelf, located near the 40 m isobath at the Columbia River mouth. Further south at the Newport Harbor line, hypoxic stations occur at mid shelf and, again, at one on the inner shelf. Three hypoxic stations are located south of Newport at the outer and mid shelves. The geographic distribution of hypoxia in the historical data may be strongly influenced by the seasonal distribution of measurements at different latitudes (Fig. 1.3a). The southern Washington shelf and the Newport Harbor line have better seasonal coverage than other locations. The northern Washington shelf, north of 47°30'N, and the Heceta Bank region, south of 44°30'N, have poor coverage, particularly during July through September. Recent studies have shown that the Heceta Bank region is characterized by weaker circulation and higher Chl *a* than the Newport Harbor line, and therefore Heceta Bank may be more susceptible to hypoxia (Grantham et al., 2004; Barth et al., 2005).

Hypoxia is observed only during June–September throughout the region (Fig. 3b,c). In the available data, the seasonal minimum of near bottom DO is lower off Washington than off Oregon over the outer shelf, mid shelf and the inner shelf (Fig. 1.3b,c). Off the Washington coast, minimum DO values at these locations (0.71, 0.49, and 0.62 mL L^{-1}) were observed on the outer and mid shelf during July, and on the inner shelf during August.

Off the Oregon coast, minimum values (0.97, 0.99, and 1.32 mL L^{-1}) were observed during September on the outer shelf, and during July on the mid and inner shelves. The difference between minimum summer DO concentrations off Washington and Oregon is greater at the mid and inner shelves than over the outer shelf.

DO concentrations over the inner shelf are more variable than over the mid and outer shelves during summer (Fig. 1.3b,c). Over the inner shelf of Washington, summer concentrations range from well below hypoxic to the higher concentrations more typical of winter further offshore (Fig. 1.3b). The Oregon inner shelf shows evidence of this broad range at six stations in August (Fig. 1.3c). Higher concentrations over the inner shelf during summer, which are not observed at mid shelf, are consistent with surface water influencing near bottom concentrations. A comparison of near bottom T vs. DO shows that, while these two properties are similar off Washington and Oregon over the mid shelf, inner shelf water with DO < 4 mL L^{-1} is often warmer off Washington than off Oregon (Fig. 1.4).

An interannual view of inner shelf data (Fig. 1.5) shows that hypoxic concentrations have been measured throughout the historical record. Over the Washington inner shelf, hypoxia was measured in all decades where data were collected, except the less frequently sampled 1950s. The higher inner shelf concentrations off Oregon are not a result of sampling different decadal time periods since there are data from both Washington and Oregon in the early–mid 1960s. Taking temporal and spatial sampling limitations into account, historical observations indicate periods of borderline hypoxic concentrations on the inner shelf of Oregon north of Heceta Bank and concentrations well below hypoxic thresholds on the inner shelf of Washington.

1.4 Processes affecting hypoxia on the Washington shelf: 2003–2006

1.4.1 Late summer hypoxia and seasonal wind forcing

Hypoxia was present in bottom water over the Washington shelf during September of all four years in the period 2003–2006, under a variety of local seasonal wind forcing conditions (Fig 1.6). During these surveys, concentrations below 1 mL L^{-1} were measured in all years except 2004, but concentrations below 0.5 mL L^{-1} were only observed in 2006. Temporal

changes on scales of 5–7 days or less are contained within each map, especially closer to shore. However, as discussed in Section 1.4.3, "patchiness" in space can also occur. The locations of DO minima in the alongshore and cross shore directions vary between surveys. During September 2003, concentrations below 1 mL L^{-1} were observed over the mid to outer shelf, but not over the inner shelf, where concentrations did, however, fall below 1.5 mL L^{-1}. During September 2004, DO concentrations below 1.5 mL L^{-1} were only observed over the mid to outer shelf, with concentrations increasing toward shore. During September 2005, concentrations below 1 mL L^{-1} were observed across the entire shelf inshore of Quinault Canyon, and at the mid to outer shelf farther south. In September–October 2006, concentrations below 0.5 mL L^{-1} were present on the mid and inner shelf, but not on the outer shelf. During this cruise, minimum values were close to 0.1 mL L^{-1} over the mid shelf and close to 0.3 mL L^{-1} over the inner shelf. We note that hypoxia has been frequently observed in the bottom water on the southern Vancouver Island shelf, also shown by Freeland and Denman (1982).

Minimum DO concentrations observed over the Washington shelf in September are consistent with the CUI integrated from the spring minimum to the end of the summer (Fig. 1.6e). The lowest (highest) minimum concentrations were observed following the strongest (weakest) seasonal upwelling favorable winds during 2006 (2004). Intermediate minimum DO concentrations between 0.5 and 1.0 mL L^{-1} were observed following CUI closer to average levels during September 2003 and September 2005. However, as discussed in Section 1.4.2, different combinations of local and remote physical forcing, and biochemical DO consumption, are involved in the seasonal development of hypoxia during these two intermediate years.

Concentrations of DO between 0.5 and 1 mL L^{-1}, observed in three of four recent years, have previously been observed in the historical record over the outer, mid and inner shelves of Washington (Fig. 1.3). In the context of the historical data, only the lowest concentrations measured during September 2006 appear to be unprecedented. The presence of concentrations less than 1 mL L^{-1} in September and October also appears to be unusual; these concentrations are more common during July and August in the historical record (Fig. 1.3).

1.4.2 Seasonal development of hypoxia in shelf bottom waters

In this section we explore the role of three processes in the seasonal draw down of near bottom DO concentrations over the Washington shelf: seasonal upwelling circulation, source water variability and respiration. In particular, we differentiate between DO demand in shelf sediments and respiration that occurs in the overlying water column.

1.4.2.1 Upwelling of low DO water over the outer and mid shelf

Hydrographic transects across the central Washington shelf during the summer of 2005 capture the seasonal evolution of the intensity and cross shelf distribution of hypoxia, along with related water properties (Fig. 1.7). DO contours transitioned from flat to tilted between late May and mid June, similar to isopycnals. The first section was taken six days after a late spring transition was observed off Oregon on 24 May (Kosro et al., 2006). Isopycnals were level in the middle of the water column over the shelf and slope, with tilting isopycnals only observed near the bottom over the shelf. During June and July, under intermittent upwelling favorable winds (Fig. 1.7b), the isopycnals in the mid water column (σ_t = 25–26 kg m^{-3}) became more tilted over the mid and outer shelf, along with DO contours 4–6 mL L^{-1} (Fig. 1.7a). In August, upwelling favorable winds intensified (Fig. 7b) and isopycnals outcropped at the surface (Fig. 1.7a). Through August and September, decreasing DO concentrations at mid shelf continued with tilting of mid water column isopycnals; the σ_t = 26.5 kg m^{-3} isopycnal approached shore and its height above the bottom increased through 8 September, with slight relaxation apparent between 8 September and 14 September. Thickening DO contours between 2 and 4 mL L^{-1} from 8 September to 14 September were associated with decreased stratification, as seen in the spreading of density contours $>$ 26.0 kg m^{-3}. Throughout the summer, DO contours followed the tilting and vertical separation of isopycnals in the water column.

Minimum DO concentrations over the shelf during 2005 were observed near the bottom, but were not always associated with the densest water (Fig. 1.7a). On 17 June, 17 July, 23 August, 8 September, and 14 September, minimum near bottom concentrations were observed inshore of the shelf break. This pattern suggests that respiration draws down DO

as water moves shoreward across the shelf from the outer shelf to the mid shelf. However, DO concentrations over the mid and outer shelf did not consistently decrease in time through early September as density increases. At the 100 m isobath, near bottom DO increased from 9 July to 17 July to 5 August, indicating that hypoxia there is either spatially patchy, temporally sporadic, or both. Patterns of DO in near bottom water are therefore more complex than can be attributed to upwelling of low DO slope water alone.

1.4.2.2 Source water variability

In this section, water properties from the Washington shelf and slope are used to address variability in the composition of water masses in the source water at the shelf break as an additional potential factor in the seasonal development of hypoxia. Stations between the 130 and 1000 m isobaths are defined as "slope" water; stations west of the 1000 m isobath, excluding stations directly within Quinault Canyon, are defined as "offshore" water to represent background properties. For each cruise, the 10–19 offshore casts were averaged into one water property profile (Fig. 1.8). Discrete samples from standard depths offshore and over the slope, and from near bottom over the outer shelf and mid shelf, are included for all stations where nutrient data are available (see Fig. 8f inset). Near bottom shelf water occurs in T, S and σ_t ranges 7–8°C, 33.4–34.0 psu and 26.1–26.6 kg m^{-3}, respectively (Figs. 1.8, 1.9a).

Offshore water properties vary on seasonal and interannual time scales. Average profiles during the beginning (June) and end (September) of summer 2003 demonstrate an increasing presence of lower DO, higher T and higher S water as the season progresses (Fig. 1.8a,b). Water properties during this year closely resemble those of historical means (Hickey et al., 2006; Landry et al., 1989), and these changes are consistent with a higher proportion of equatorial water in late summer (MacFadyen et al., 2008; Lynn and Simpson, 1987). Seasonal changes offshore during 2005 suggest the opposite progression; average profiles have higher DO, lower T and lower S in during September 2005 than July 2005 (Fig. 8c,d). Seasonal variability during 2003 and 2005 is associated with changes in T of less than 0.5°C (Figs. 1.8b,d, 1.9b). Larger differences in background properties are associated with

interannual variability; low DO in offshore water during September 2006 is associated with a warm anomaly, up to 1°C warmer than 2003 or 2004 at salinities between 33 and 34 psu (Figs. 1.8e, 1.9b), consistent with a greater influence of low DO equatorial water. Near bottom shelf water during this period is also relatively dense (Fig. 1.8f), suggesting that seasonal upwelling of deep, low DO water is an additional factor in the severe hypoxia during summer 2006. In the range of physical properties occupied by near bottom shelf water, corresponding offshore DO concentrations are not hypoxic (Figs. 1.8, 1.9a). Variability in offshore water masses can therefore only account for seasonal decreases to concentrations as low as $\sim$1.5 mL L^{-1} in near bottom water.

DO concentrations over the slope differ from those offshore, particularly during late summer (Fig. 1.8), and we next address whether these lower concentrations are associated with a difference in water mass composition over the slope, or biochemical depletion of DO. In the 7.0–8.0°C range, slope DO concentrations reached a minimum of 1.04 mL L^{-1}, 1.41 mL L^{-1}, 0.83 mL L^{-1} and 0.97 mL L^{-1} in 2003, 2004, 2005 and 2006, respectively (Fig. 1.8). However, there is no evidence of significantly higher T or S over the slope than the offshore averages during 2003, 2004 or 2006 (Figs. 1.9b,f). During 2005, higher T and S do occur over the slope, resembling the offshore properties earlier that summer in June when slope DO concentrations were higher (Fig. 1.9d). These water properties suggest that, in general, hypoxic DO concentrations over the slope result from respiration near the shelf in the northern CCS, not physical transport of equatorial water by the California Undercurrent.

1.4.2.3 Biochemical depletion of DO

Evidence of DO depletion due to biochemical processes is present over the slope and in near bottom water over the continental shelf during late summer. In particular, relationships between DO, T and S at these locations do not follow the structure of the offshore properties, especially during late summer (Fig. 1.8, 1.9a). In order to quantify the amount of respiration that has influenced each sample over the slope and shelf, we define the DO deficit as the difference between a sample's DO concentration and the average offshore concentration at

the same salinity for that cruise. Average offshore relationships between DO and S are not greatly affected by water mass composition, and are similar throughout all six cruises during summers 2003–2006, with $\leq$0.5 mL L^{-1} difference at constant S (Fig. 1.9a). In the range of salinity that occurs in shelf bottom water (33.4–34.0 psu), offshore DO concentrations range from 1.5–4.0 mL L^{-1}. This relationship represents the potential contribution to the seasonal draw down of DO by the combination of physical processes already discussed, either seasonal upwelling or an enhanced California Undercurrent, since these processes are both associated with high S and low DO.

Differences in DO deficits between cruises can reveal the contribution to hypoxia not associated with physical processes. For example, there is >0.5 mL L^{-1} difference in DO deficit between September 2003 and 2004, even though mid shelf bottom water occurs in the same range of salinity (33.4–33.8) for both cruises (Fig. 1.9a,f). The larger DO deficits in 2003, in a similar range of S, suggest that stronger DO consumption in 2003 is the primary factor causing lower DO concentrations (<1 mL L^{-1}) that year.

In contrast, similar DO deficits are observed under varying degrees of hypoxia. For example, DO deficits approached magnitudes of 2.5 mL L^{-1} during September 2003, September 2005 and September 2006, although the minimum DO was significantly lower during 2006 (Fig. 1.9a,f). Bottom water salinity was similar in 2005 and 2006, but high DO concentrations were present in offshore water at these salinity values during 2005 (Fig. 1.9a). Of these three years, mid shelf bottom water salinity was lowest in 2003 (Fig. 1.9a), consistent with average upwelling favorable winds (Fig. 1.6f) and a lack of equatorial influence compared with the other years (Fig. 1.6b). Therefore, physical processes, the enhanced upwelling and the enhanced California Undercurrent described previously, significantly contributed to the extremely low DO concentrations observed in 2006, in addition to biochemical processes.

1.4.2.4 DO demand in sediments

To distinguish between the water column and sediments as sinks of DO, we use denitrification as an indicator of sedimentary DO consumption, combining measurements from this study and previously published benthic fluxes in order to formulate mass balances of DO

and N. We use two separate methods to calculate N deficits, which quantify the amount of N that has been lost to denitrification. Denitrification does not occur in the water column unless DO concentrations fall below ~0.2 mL L^{-1}, close to the minimum concentrations observed in September 2006, but not typically associated with hypoxia in the northern CCS. We show that N deficits are correlated with the DO deficits caused by biochemical processes in both the water column and sediments. This relationship, along with benthic fluxes of DO and nutrients from previous studies over the Washington shelf (Devol and Christensen, 1993), are incorporated into a simple mass balance of DO and N in the bottom mixed layer, providing estimates of DO consumption separately in the water column and sediment.

The amount of denitrification that has influenced a water parcel can be quantified by comparing the relationships of observed inorganic nutrient and DO concentrations to those predicted by the stoichiometry of organic matter. The stoichiometry involved in aerobic respiration can be described approximately by the equation (Anderson, 1995)

$$C_{106}H_{175}O_{42}N_{16}P + 150\,O_2 = 106\,CO_2 + 16\,HNO_3 + H_3PO_4 + 78\,H_2O, \qquad (1.1)$$

which implicitly includes an intermediate step in which ammonium (NH_4^+) is oxidized to nitrate during nitrification in the presence of oxygen. In equation (1.1), 16 moles of N are produced for every 1 mole of P produced and every 150 moles of DO consumed. Assuming the same chemical composition of organic matter, Gruber and Sarmiento (1997) describe the stoichiometry of denitrification using the equation

$$C_{106}H_{175}O_{42}N_{16}P + 104\,NO_3^- = 4\,CO_2 + 102\,HCO_3^- + 60\,N_2 + 36\,H_2O + HPO_4^{2-}, \qquad (1.2)$$

in which 104 moles of N are consumed for every mole of P produced. In Washington shelf sediments, denitrification consumes nitrate that is supplied by fluxes from the overlying water column and nitrate that is produced during nitrification; some portion of ammonium produced during organic matter degradation escapes as a flux out of the sediments (Devol and Christensen, 1993; Hartnett and Devol, 2003). Deviations from offshore N-P and N-DO ratios in slope water and near bottom shelf water (Fig. 1.9c,d) are consistent with the influence of sedimentary denitrification.

Nutrient and DO data from ECOHAB-PNW cruises are used to calculate N deficits, which quantify the amount of N that has been removed from the water by denitrification. The first definition of N deficit, based on N and P concentrations, is similar in form to the N deficit used by Codispoti et al. (2001) in the Arabian Sea and also to the negative of Gruber and Sarmiento (1997)'s N* used in their global N budget

$$\mathrm{N\,deficit} = \left[\left(r_{aer}^{N:P}\mathrm{P} + c_{aer}^{N:P}\right) - \mathrm{N}\right] * \left(\frac{r_{denitr}^{N:P}}{r_{denitr}^{N:P} - r_{aer}^{N:P}}\right), \tag{1.3}$$

where $r_{aer}^{N:P}$ is the stoichiometric ratio of N and P during aerobic respiration as in (1.1), the constant $c_{aer}^{N:P}$ accounts for limitation of either N or P, and $r_{denitr}^{N:P}$ is the stoichiometric ratio of N and P during denitrification as in (1.2). We assume $r_{denitr}^{N:P} = 104$, following Gruber and Sarmiento (1997), who estimate an uncertainty of 15 in this value. We assume that ammonium concentrations are negligible in the calculation of total inorganic nitrogen and its deficit because average ammonium concentrations over the Washington shelf during summer are <1 μM, with maximum values at the inner shelf, away from the stations we are considering in this portion of the analysis (Landry et al., 1989). Values for $r_{aer}^{N:P}$ and $c_{aer}^{N:P}$, which describe the relationship between N and P away from the influence of denitrification, were determined from a linear regression of offshore N and P data for each ECOHAB-PNW cruise (Fig. 1.9b). With the exception of the two cruises in 2005 (EH4, EH5), was within the range 14.9–15.7.

To incorporate N deficits into mass balances of N and DO, we have compared N deficits as calculated above with those calculated using an alternate method that uses the N-DO rather than N-P relationships. In the absence of denitrification, Equation (1.1) suggests that 9.375 moles of DO should be consumed for every mole of N remineralized. Based on this concept, Broecker (1974) developed the tracer

$$\mathrm{NO} = c_{aer}^{DO:N} * \mathrm{N} + \mathrm{DO}, \tag{1.4}$$

where $c_{aer}^{DO:N}$ is the ratio at which DO and N are consumed and remineralized during aerobic respiration. N deficit can be expressed as

$$\text{N deficit} = \frac{[\text{NO}_{expected} - NO]}{c_{aer}^{DO:N}}, \tag{1.5}$$

where $\text{NO}_{expected}$ is the value of NO away from the influence of denitrification. We utilize the average offshore NO in the salinity range $32.8 < \text{S} < 34.0$ psu for each cruise, which results in values of $\text{NO}_{expected} = 425 \pm 14$ μM. Our two methods of calculating N deficit agree, except for the two cruises in 2005 where offshore relationships between DO, N and P appear to be anomalous (Fig. 1.9c–1.9e). We utilize the NO method in the following analysis and test the sensitivity of our results to the anomalous 2005 data.

N deficits and DO deficits in near bottom water and 100–200 m slope water for all six ECOHAB-PNW cruises are linearly related (Fig. 1.9f). The linear regression ($r^2 = 0.77$, $p < 0.01$) was calculated using a geometric mean functional technique (Ricker, 1984). The slope of the regression decreases slightly from 11.1 to 10.9 when anomalous 2005 data are removed. While there is some evidence of N and DO deficits in slope water, their largest values are $\sim$1/2 as high as those over the mid- to outer shelf (Fig. 1.9f).

Simplified mass balances of N and DO can be used to calculate the relative importance of respiration in the water column and sediments. In a bottom mixed layer overlying the sediment, biochemical changes in N and DO can be expressed as

$$\frac{dN}{dt} = \frac{1}{h_{BML}}\left(f_{sed}^{NO_3^-} + f_{sed}^{NO_2^-} + f_{sed}^{NH_4^+}\right) - \frac{1}{c_{aer}^{DO:N}} k_{wc}^{DO} \tag{1.6a}$$

$$\frac{dDO}{dt} = \frac{1}{h_{BML}}\left(f_{sed}^{DO} - \frac{1}{2} f_{sed}^{NO_2^-} - 2 f_{sed}^{NH_4^+}\right) + k_{wc}^{DO}, \tag{1.6b}$$

where d/dt is the material derivative following a parcel of near bottom water, f_{sed} represents a flux from the sediment into the water column, h_{BML} is the bottom mixed layer height, and k_{wc}^{DO} is the water column rate of aerobic respiration. These equations assume that all nitrite and ammonium that escape the sediment are oxidized to nitrate. Utilizing the chain rule and applying equations (1.4) and (1.5),

$$\frac{d(DO\,\text{deficit})}{d(N\,\text{deficit})} = \frac{dDO}{dt} \Big/ \left(\frac{1}{c_{aer}^{DO:N}} \frac{dDO}{dt} + \frac{dN}{dt}\right), \tag{1.7}$$

gives an expression for the water column rate,

$$k_{wc}^{DO} = \left[k_{sed}^{N} \frac{d(DO\,\text{deficit})}{d(N\,\text{deficit})} + k_{sed}^{DO} \left(\frac{1}{c_{aer}^{DO:N}} \frac{d(DO\,\text{deficit})}{d(N\,\text{deficit})} - 1 \right) \right], \tag{1.8}$$

where k_{sed}^{N} and k_{sed}^{DO} are the rates of change of N and DO in the bottom mixed layer due to sediment fluxes, including those associated with oxidation of nitrite and ammonium. Means and 95% confidence intervals for all parameters used to estimate k_{wc}^{DO} are shown in Table 1.2. The bottom mixed layer height h_{BML} is estimated as the height over the bottom at which vertical DO gradients exceed 0.1 mL L^{-1} m^{-1} (a temperature gradient criterion of 0.01 °C m^{-1} gives similar results). The relationship $d(DO\,\text{deficit})/d(N\,\text{deficit})$ is given by the slope of the regression in Fig. 1.9f. Sediment fluxes from previous studies were measured using benthic tripods over the Washington shelf and slope during June and July of 1989 and 1991 (Devol and Christensen, 1993). Published flux values used for this analysis are from bottom depths < 200 m to capture only processes occurring on the continental shelf and upper slope. The shallowest benthic flux measurement was at 42 m bottom depth off Grays Harbor, and bottom water DO concentrations were 1.5–2.5 mL L^{-1} (Devol and Christensen, 1993). The standard error (2σ) of the mass balance results are calculated using a Monte Carlo method (10^6 runs), with parameters having Student t-distributions as described in Table 1.2.

The mass balances of DO and N can indicate whether the observed relationship between DO and N deficits are consistent with a significant contribution to aerobic respiration from the sediment. The calculated water column rate, k_{wc}^{DO}, is -0.021 ± 0.007 mL L^{-1} d^{-1}, or 0.92 ± 0.30 μM d^{-1}; the sedimentary DO flux into the bottom mixed layer results in a similar rate, -0.020 ± 0.005 mL L^{-1} d^{-1}, or -0.90 ± 0.21 μM d^{-1}; and oxidation of the ammonium flux from the sediments contributes a small amount, -0.002 mL L^{-1} d^{-1}; or 0.09 μM d^{-1}. The mass balance also results in a small N increase, 0.032 ± 0.020 μM d^{-1}, which suggests that the combination of the ammonium flux from the sediments and the mineralization of N during water column respiration balances the loss of near bottom N to denitrification in sediments.

Results from the mass balance indicate that DO consumption in the water column and sediments contribute similarly, 40–60% each, to the rate of decrease of DO in near

bottom water. Further support for these estimates of DO consumption is obtained from time series of DO from moored sensors. The data display a significant downward trend over several weeks during both 2005 and 2006 (Fig. 1.10a). Since this trend is not coincident with decreasing temperatures (Fig. 1.10b), declining DO at this location is likely due to respiration, not upwelling of progressively colder water from further offshore. The total DO consumption calculated from the mass balance agrees well with the observed downward trends in both years. The DO decline during 2006 follows a bloom in the surface layer (Fig. 1.10c), which occurred before the start of the DO time series. A period of relatively high surface fluorescence, confirmed by Chl *a* concentrations 6.5–17.0 μg L^{-1} in bottle samples, continued through the DO time series (Fig. 10c). During 2005, satellite data indicate a transition from negative to positive Chl *a* anomalies during July (Thomas and Brickley, 2006), which precedes the start of the DO decline in early August (Fig. 1.10c).

1.4.3 Event time scale variability in DO of shelf bottom water

In addition to seasonal trends, DO time series from moored sensors exhibit significant shorter period fluctuations (Fig. 1.10a). During late August–September 2005, four events with amplitude 0.6–1.0 mL L^{-1} are observed, each lasting 5 to 10 days. During 2006, there are fewer events of this magnitude and duration. There are, however, two relatively sharp decreases of DO over the course of the 2006 time series starting 11 September and 28 September, as well as a peak above 5 mL L^{-1}. This section will explore the short time scale processes that result in these DO fluctuations. The rate of change in DO concentration due to horizontal advection is given by the equation

$$\frac{\partial O}{\partial t} = -u\frac{\partial O}{\partial x} - v\frac{\partial O}{\partial y}, \tag{1.9}$$

where $\partial O/\partial t$ is the time rate of change of DO; u, v are the cross shelf and alongshelf components of the velocity; and $\partial O/\partial x$, $\partial O/\partial y$ are the cross shelf and alongshelf components of the spatial gradient of DO. In the following, we use hydrographic data and moored sensor data to provide estimates of the individual contributions from these two components to DO variability over time scales of several days.

During mid August through late September 2005, upwelling favorable winds were frequently interrupted by relaxation and weak downwelling events, in contrast to the persistent upwelling that characterized the preceding period from mid July through mid August (Fig. 1.6e). From 24 August to 14 September, the phase relationship between $\partial O/\partial t$ and v is out of phase; increasing (decreasing) DO concentrations coincided with equatorward (poleward) flow (Fig. 1.11a). After 14 September, the phase relationship between $\partial O/\partial t$ and v shifted to be in phase; increasing (decreasing) DO concentrations coincided with poleward (equatorward) flow. Overall, the time series are consistent with alongshore advection of a low DO patch that begins south of the mooring, then moves north of the mooring during a period of prolonged poleward flow and relatively weak winds (Fig. 1.11a,b).

This period of alternating upwelling and downwelling conditions over the inner shelf was accompanied by the appearance of higher near bottom fluorescence at E4 (Fig. 1.11c). Calibrated shipboard fluorescence data from nearby stations E2, KB02, and KB01 are consistent with the moored sensor (Fig. 1.11c); no casts were taken exactly at the mooring site. Although peaks in near bottom fluorescence are small compared to values typically observed with a bloom in the euphotic zone, the presence of photosynthetic pigment near the bottom suggests that organic matter, and the potential for respiration, has been introduced to the bottom water, either by sinking, advection, or resuspension of particles.

To further assess whether the advection of an alongshore patch can account for the magnitude and timing of DO fluctuations during this period in 2005, we have estimated time integrals of the advective terms on the right hand side of (1.9), for direct comparison with the DO time series. In the cross shelf calculation, gradients are taken from the KB line, the transect closest to the mooring, and the integral evaluated forwards and backwards in time until the integrated cross shelf velocity exceeds the distance to KB stations on the shelf. Gradients at the KB line are small during this period; we also use the largest gradient shown in Fig. 1.11d in order to generate larger cross shelf fluctuations and compare their timing to observations. In the alongshelf direction, both positive and negative gradients occur, supporting the idea of an alongshelf minimum in DO (Fig. 1.11d). The largest observed gradient is applied, positive poleward of the patch center and negative equatorward of a patch center. This choice ensures that gradients are not underestimated during periods

when the hypothesized patch is between the mooring and ship. The integration is started on 22 August, soon after the appearance of near bottom fluorescence (Fig. 1.11c).

In the cross shelf direction, the modeled fluctuations show no significant correlation with the observed data, and the magnitude of the fluctuations are far too small, even with the relatively large non-local gradient (Fig. 1.11e). Because the cross shelf velocity is sensitive to the direction in which the coordinate system is rotated, results using a coordinate system rotated 10 degrees in either direction are also shown (Fig. 1.11e), with little improvement of the results. The alongshelf integration is far more successful in reproducing the observed time series (Fig. 1.11f). In this case, modeled fluctuations have the correct timing to account for the observations. Additional results are shown with a constant trend, the total respiration calculated in Section 1.4.2.4 (Fig. 1.10a), to account for large scale respiration over the shelf, and also with a reduction of velocity by 50% to account for the effects of bottom friction in reducing the velocity between the current meter and the DO sensor. Though a strictly linear interpolation with a no-slip condition would result in a 75% reduction in velocity, a realistic velocity profile has more of a logarithmic shape; at E2, the difference between v at 13 m and 7 m above the bottom is never more than 10% during this time period (not shown). While the simple trend improves agreement with the data, the velocity reduction results in a slight underestimate of the magnitude of the fluctuations (Fig. 1.11f). In addition, the observed DO increase starting on 14 September occurs too late in the model, which predicts an increase when the patch passes by the mooring site on 18 September. This inconsistency may be a consequence of downward vertical advection during prolonged poleward flow on the inner shelf (Fig. 1.11a).

Fluctuations in DO concentration during 2006 are typically much weaker than in 2005, with the exception of one high DO event (Fig. 1.10). During this event, DO concentrations increase beginning 15 September, along with acceleration to poleward flow which later peaks in excess of 20 cm s^{-1} (Fig. 1.12a). DO concentrations return to hypoxic levels beginning 23 September, within days after upwelling winds resume (Fig. 1.12b). On this date, flow 12 m above the bottom is poleward and offshore, which is inconsistent with upwelling. However, since temperature also dropped by >2 °C (Fig. 1.10b), the decrease in DO is likely due to unresolved onshore transport in the bottom boundary layer, not biochemical consumption.

Two additional notable decreases in DO during 2006, ∼0.4–0.6 mL L^{-1} d^{-1}, occur on 11 September and 28 September (Fig 1.12a). These events occur during strong upwelling favorable winds (Fig. l2b) and also follow peaks in near bottom fluorescence (Fig. 1.12c), although the magnitude of the fluorescence peaks is not as great as in 2005 (Fig. 1.11c). Shipboard measurements at the mooring site confirm low background fluorescence levels (Fig. 1.12c); Chl *a* concentrations from bottle samples exceed the mooring values by 1–2 μg L^{-1}, and the shipboard fluorometer agrees more closely with the mooring. Cross shelf transport was integrated in a similar manner as the 2005 analysis, using spatially variable gradients from the KB line near the mooring. These KB transects have strong positive gradients at the two stations closest to shore (Fig. 1.12d), and weak negative gradients DO further offshore corresponding to mid shelf minima (Fig. 1.6d, e.g.). The cross shelf models reproduce the decreases in DO beginning 11 September and 28 September, and the gradual increase in DO beginning 30 September (Fig. 1.12e). The models fail to predict the onset of the large peak in DO, and the timing of the return to hypoxia following the peak.

Alongshelf advection does not appear to be as important during 2006 as 2005. The only strong alongshelf gradients are positive and appear during the onset of the strong poleward wind event after 15 September; those measured closest in time to the decreasing DO events are smaller, between 0–0.015 mL L^{-1} km^{-1}, at the same time when large cross shelf gradients are observed (Fig. 1.12d). An alongshore integration with a gradient of 0.05 mL L^{-1} km^{-1} increasing northward results in increasing DO concentrations during the three periods where observations show significant decreases (Fig. 12f). Using a smaller alongshore gradient of 0.015 mL L^{-1} km^{-1}, with a 50% velocity reduction and trend as in the 2005 analysis, eliminates event scale variability and more accurately reproduces longer term variability (Fig. 1.12f). The lack of alongshore variation in DO during 2006, in contrast to 2005, suggests that the bloom observed in the surface layer (Fig. 1.10c) resulted in DO consumption over a greater alongshelf scale during 2006. A large region of low DO in the near bottom water along the mid shelf, consistent with the 2006 survey map (Fig. 1.6d), allowed for rapid return to severe hypoxia over the inner shelf within several days, even after strong downwelling favorable winds.

1.5 Summary and discussion

In this paper, historical and recent hydrographic data, as well as moored sensors, are used to investigate spatial patterns of hypoxia in the northern CCS and its temporal variability from days to decades. In particular, we show that, off Washington 1) hypoxia occurs under a wide range of wind forcing conditions and source water properties; 2) biochemical DO consumption in both the water column and sediments is a significant factor in the development of hypoxia; 3) advection of patches with spatial scales ∼10–50 km can lead to short term variability; and 4) in contrast to historical measurements over the Oregon shelf, DO concentrations below 1 mL L^{-1} are a recurring feature in the historical record, including the inner shelf.

The results of this study emphasize the fact that hypoxia is a seasonal feature of the northern CCS. Hypoxia is present in near bottom water throughout the historical record (Fig. 1.4), and was observed off the Washington shelf during all four recent September surveys with different seasonal wind forcing (Fig. 1.6). The strength of the seasonal upwelling favorable winds appears to be an important factor in the severity of hypoxia at the mid-outer shelf, with stronger upwelling favorable winds associated with lower minimum DO concentrations over the Washington shelf, as seen most dramatically during 2006.

Over the Washington shelf, interannual differences in near bottom DO are related in part to the biological response to upwelling. Not only do upwelling events increase phytoplankton standing stock in the euphotic zone by supplying nutrients, persistent upwelling may also promote near bottom respiration by retaining sinking material closer to the shelf (Hales et al., 2006). Furthermore, hypoxic bottom waters promote increased concentrations of iron (II) in near bottom water, which could enhance primary production if that water is upwelled to the euphotic zone (Lohan and Bruland, 2008). Our results from recent data demonstrate that cross shelf transport of offshore water and interannual changes in its water mass composition can only account for decreases to concentrations as low as ∼1.5 mL L^{-1}; shelf DO concentrations at salinity between 33.4 and 34.0 psu indicate that biochemical consumption typically decreases concentrations by an additional 0.5–2.5 mL L^{-1}, depending on the year and location (Fig. 1.10a). Weak upwelling favorable winds during late August

and September 2004 (Fig. 1.9) likely kept DO deficits, which indicate biochemical depletion of DO, relatively low by limiting primary productivity and subsequent respiration. Although much of the September 2004 data were collected during a period of strong downwelling favorable winds (MacFadyen et al., 2008), such events primarily replenish DO on the inner shelf (Section 1.4.3, Fig. 1.12).

During summer 2006, several factors coincided to allow severe hypoxia to occur over the Washington shelf. Compared with September 2003, near bottom shelf water during September 2006 had similar DO deficits but higher salinity (Fig. 1.9a), consistent with lower DO source water due to enhanced seasonal upwelling favorable winds (Fig. 1.6) and a strong California Undercurrent as indicated by a warm anomaly (Fig. 1.9c,d). It may be surprising that DO deficits do not indicate a stronger biological response in September 2006 following strong seasonal upwelling favorable winds. However, it is possible that stronger DO deficits in September 2006 were not observed only because low DO concentrations inhibited additional respiration in the water column and/or sediments. Compared with 2005, which was characterized by strong upwelling during the later part of the season only, near bottom shelf water during 2006 was characterized by similar decreasing DO trends in mooring time series (Fig. 1.10), but less "patchiness". Water column respiration may have been responsible for the observed patchiness during 2005, since a stationary patch of enhanced sediment respiration is less likely to form a well defined patch in the overlying moving water column. Strong upwelling winds throughout the entire summer of 2006, instead of just the late season, may have created conditions where fresh organic matter was readily available to be processed by respiration over the entire shelf, instead of in isolated locations.

The presence of N-P and N-DO relationships in near bottom water that have been influenced by denitrification in sediment pore water (Fig. 1.9c–f) indicate that DO consumption in shelf sediments is an important biochemical contribution to the development of seasonal hypoxia, in addition to respiration in the water column. Simple mass balances of DO and N relate recently collected water column data to previously published fluxes at the Washington shelf during early summer (Devol and Christensen, 1993). There do not appear to be seasonal changes in the relationship between near bottom DO deficits and N deficits from early to late summer during 2003 and 2005 (Fig. 1.9f), but it is possible high N deficits

observed during September 2006 are associated with changes in sediment processes during severely hypoxic conditions. As DO concentrations decrease, fluxes of DO into the sediments should theoretically decrease due to reduced pore water irrigation by benthic macrofauna (Archer and Devol, 1992), and fluxes of nitrate should increase (Middelburg et al., 1996). Our estimated average water column respiration rate, 0.021 mL L^{-1} d^{-1} (or 0.92 μM d^{-1}), is consistent with measurements of water column respiration in coastal upwelling regions of the Eastern Atlantic; which indicate that respiration rates below 1 μM d^{-1} commonly occur at water depths >50 m, even below highly productive surface waters, though rates can sometimes reach as high as 3 μM d^{-1} in this depth range (Robinson et al., 2002).

Over the inner shelf of Washington, DO concentrations do not always respond to wind as expected by simple two dimensional dynamics, particularly when respiration results in significant alongshelf gradients. During 2005, low DO concentrations on the inner shelf appeared during both upwelling and downwelling favorable winds, and were controlled by the alongshore advection of an isolated patch of low DO rather than by cross shelf transport (Fig. 1.11e,f). It is possible that patchiness may be more prevalent off Washington than Oregon. Since inner shelf hypoxia is present under a broader range of temperatures in the historical measurements off Washington than Oregon (Fig. 1.4), patches of low DO may be able to persist under a wider range of short term wind forcing rather than just the strongest upwelling events and therefore may account for a greater portion of the event scale variability.

The lower DO concentrations off Washington compared with Oregon in the historical record (Figs. 1.3, 1.4) are likely related to differences in physical and biological dynamics. Ware and Thomson (2005) and Hickey and Banas (2008) show that the coast of Washington and the southern coast of British Columbia are the most highly productive regions along the western coast of North America. Greater shelf width, nutrients from the Juan de Fuca eddy, mixing in estuaries, enhanced upwelling over submarine canyons, coastal trapped waves and differential impacts of grazing may play a role in maintaining this higher productivity despite stronger upwelling winds to the south (MacFadyen et al., 2008; Hickey and Banas, 2008; Banas et al., 2009). Recent observations show that microzooplankton consume an average of 66% of primary production during summer in the northern CCS, and are therefore a strong

regulator in the fate of organic matter (Lessard and Frame, 2008). Thus, the physical and biological dynamics which lead to hypoxia off the coast of Washington, while linked to processes occurring over the broader California Current region, are also uniquely determined by the specific setting.

Despite the seasonal presence of hypoxia, and extremely low DO concentrations in 2006, the Washington shelf is not typically anoxic like many other upwelling systems. Anoxic conditions elsewhere have arisen from several sets of unique conditions, and demonstrate the sensitivity of hypoxia in upwelling systems to changes in local productivity and largescale physical forcing. Anoxia on the Peru shelf is less prevalent during El Niño years, which are associated with warm anomalies and decreased primary productivity (Barber and Chavez, 1983; Arntz et al., 1991). Anoxia in Peru also appears to be sensitive to declines in planktivorous fish populations because reduction in grazing allows more organic material to accumulate and degrade (Walsh, 1981). On the Namibian shelf off southwest Africa, upwelling occurs yearround, but anoxia is generated alongside a seasonal shift in the proportion of high DO (>4 mL L^{-1}) and hypoxic (<1 mL L^{-1}) source waters (Monteiro et al., 2006). In this case, equatorward flow associated with stronger upwelling can actually inhibit the formation of anoxia by increasing the proportion of high DO and low nutrient source water, and also by decreasing the residence time over which respiration acts (Brüchert et al., 2006). Over the western Indian shelf, upwelling of nutrients forced by remote winds occurs simultaneously with reduced ventilation and anthropogenic nutrient loading from monsoon river runoff, leading to seasonally anoxic conditions (Naqvi et al., 2006). Off the Washington coast, advection and respiration create a situation where summer DO concentrations are typically hypoxic, rather than anoxic, supporting a benthic ecosystem that ranks between the severely hypoxic Peru shelf and the relatively high DO northwest Africa shelf in abundance of benthic macrofauna (Jumars and Banse, 1989).

An important question is whether hypoxic events are becoming more severe in the northern California Current system. It has been hypothesized that an increase in upwelling favorable wind stress, in response to warming temperatures, could push upwelling systems past a tipping point where anoxia becomes prevalent (Bakun and Weeks, 2004). The specific mechanism proposed by Bakun and Weeks (2004) is that intense and persistent upwelling

favorable winds would push zooplankton out of the shelf region before they are able to consume faster-growing phytoplankton, which, in the absence of planktivorous fish, would cause more organic matter to reach the shelf sediments. Although intensified equatorward winds do not appear to be strongly influencing the northern CCS when compared with the central and southern California coasts to the south (Schwing and Mendelssohn, 1997), the presence of an intrusion of nutrient rich subarctic water during a hypoxic event off Oregon in 2002 (Grantham et al., 2004), not present in 2006, shows that there are several different potential mechanisms leading to severe hypoxia. Bograd et al. (2008) have observed significant declines of DO between the years 1984 and 2006 in the CalCOFI region, including California Undercurrent water. With the highest productivity on the US west coast, and a history of seasonal hypoxia, the northern CCS may be particularly sensitive to a comparable decline of DO in this same water.

Table 1.1: Summary of ECOHAB-PNW (EH) and RISE (R) shipboard data from 2003-2006.

Study	Cruise ID	Ship	Start	Finish
EH1	W0306A	R/V *Wecoma*	2 Jun 2003	23 Jun 2003
EH2	W0308C	R/V *Wecoma*	30 Aug 2003	19 Sep 2003
EH3	AT11-17	R/V *Atlantis*	8 Sep 2004	28 Sep 2004
R2-W	W0505C	R/V *Wecoma*	29 May 2005	21 Jun 2005
EH4	AT11-30	R/V *Atlantis*	7 Jul 2005	27 Jul 2005
R3-W	W0508C	R/V *Wecoma*	4 Aug 2005	27 Aug 2005
EH5	TUIM14VM	R/V *Melville*	2 Sep 2005	22 Sep 2005
EH6	TN200	R/V *Thompson*	11 Sep 2006	4 Oct 2006

Table 1.2: Mean values ± 95% confidence intervals for parameters in Equation (1.8). Number of samples is given by n_s. For h_{BML} and $d(DO\,\text{deficit})/d(N\,\text{deficit})$ data are from this study; flux data are from upper 200 m in (Devol and Christensen, 1993).

Parameter	Value	n_s
h_{BML}	11.8 ± 0.9 m	155
$d(DO\,\text{deficit})/d(N\,\text{deficit})$	11.1 ± 0.9	114
f_{sed}^{DO}	-0.236 ± 0.050 (mL L^{-1}) m d^{-1}	13
	(-10.54 ± 2.25 mmol m^2 d^{-1})	
$f_{sed}^{NO_3^-}$	-1.33 ± 0.11 mmol m^2 d^{-1}	13
$f_{sed}^{NH_4^+}$	0.48 ± 0.21 mmol m^2 d^{-1}	13
$f_{sed}^{NO_2^-}$	0.07 ± 0.06 mmol m^2 d^{-1}	13

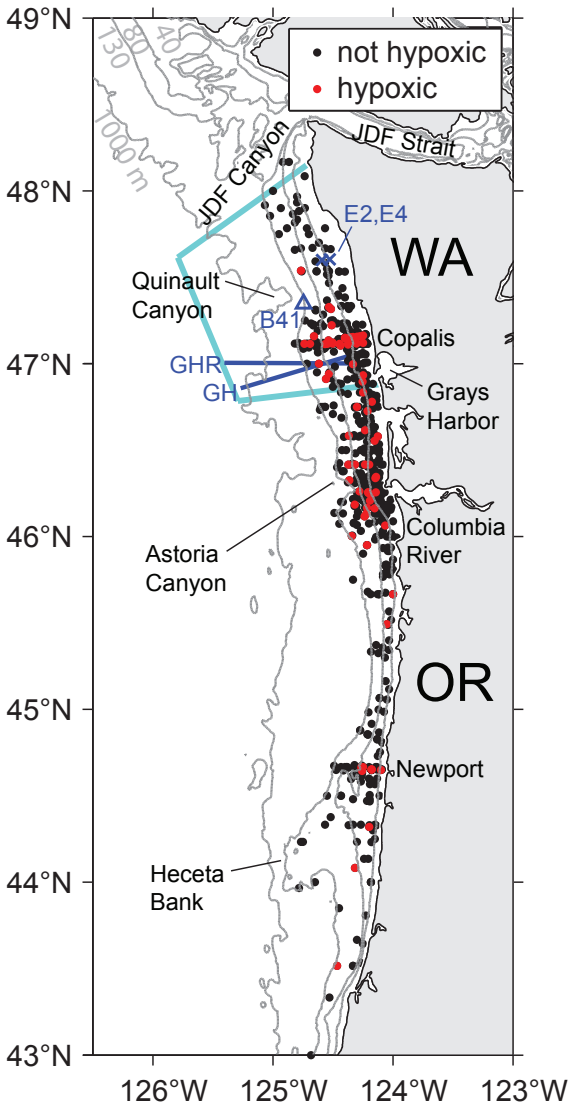

Figure 1.1: Bathymetry of the Washington (WA) and Oregon (OR) continental shelf region. The 40, 80, 130 and 1000 m isobaths are shown. The blue triangle indicates the location of NDBC wind buoy 46041 (B41). The blue x's indicate locations of the E2 and E4 moorings. The GH and GHR hydrographic lines are shown as solid blue lines. Light blue encloses the study region on the Washington shelf. Also shown are the locations of historical near bottom, continental shelf (10 m from bottom or less, 130 m bottom depth or less) stations for Washington and Oregon. Historical observations of near bottom hypoxia are red; all others black.

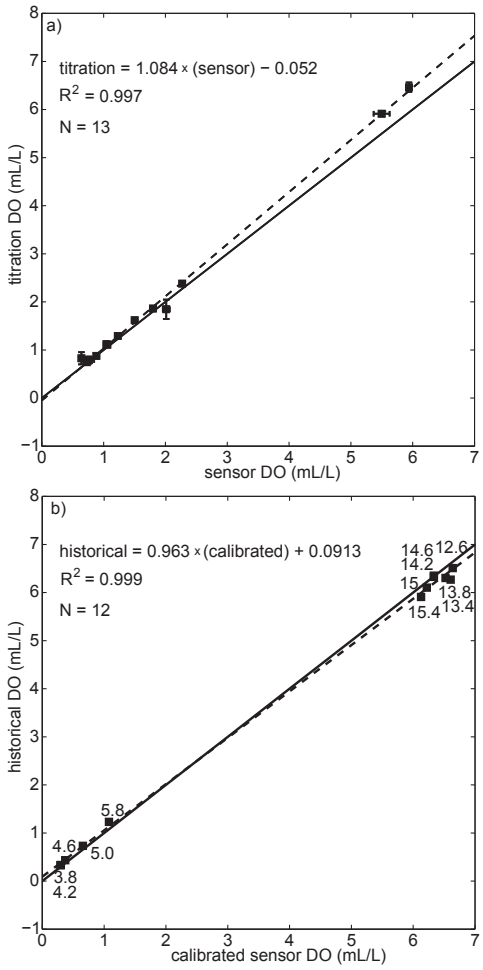

Figure 1.2: a) Least-squares linear regression (dashed line) between DO concentrations measured by factory calibrated SBE 43 sensor (x-axis) and Winkler titration (y-axis) during the EH6 cruise in September 2006. Error bars, where visible, are standard deviations from triplicate samples. b) Regression between mean DO at selected temperatures from the calibrated sensor during the EH6 cruise and the historical data set, as described in the text. Numbers beside points are the center of the temperature bins. Solid lines designate 1:1 slope.

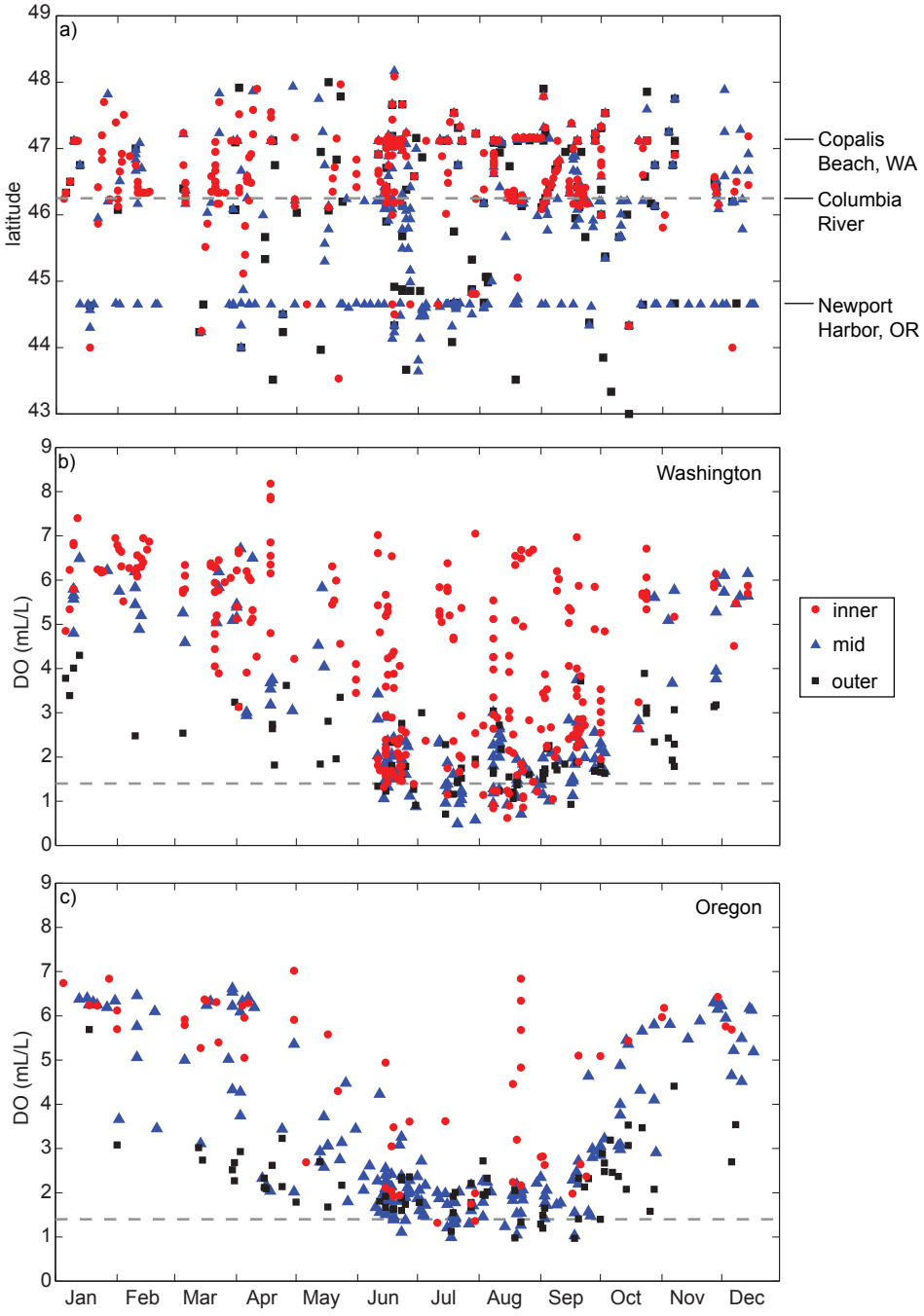

Figure 1.3: a) Seasonal distribution of near bottom DO measurements by latitude. Data is divided into three depth categories: inner shelf 0–40 m (red circles), mid shelf 40–80 m (blue triangles), and outer shelf 80–130 m (black squares). The dashed lines indicate the division between Washington and Oregon data. b) Seasonal cycle of historical near bottom DO over the Washington shelf. Symbols as in a. Dashed line indicates the 1.4 mL L^{-1} definition of hypoxia. c) Seasonal cycle of historical near bottom DO over the Oregon shelf, as in b.

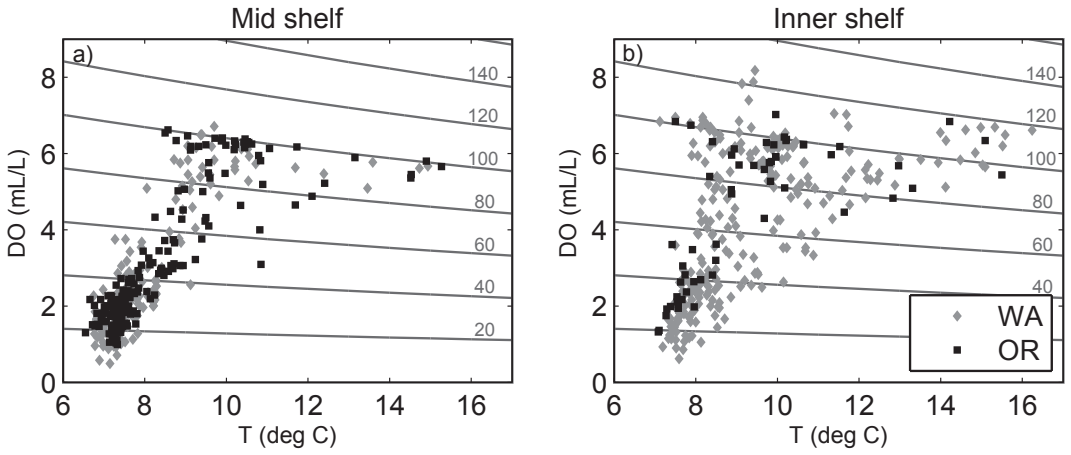

Figure 1.4: Temperature vs. DO for near bottom measurements over a) the mid shelf (40–80 m bottom depth), and b) the inner shelf (40 m bottom depth or less) of Washington (grey diamonds) and Oregon (black squares). Contours indicate percent saturation at 33 psu.

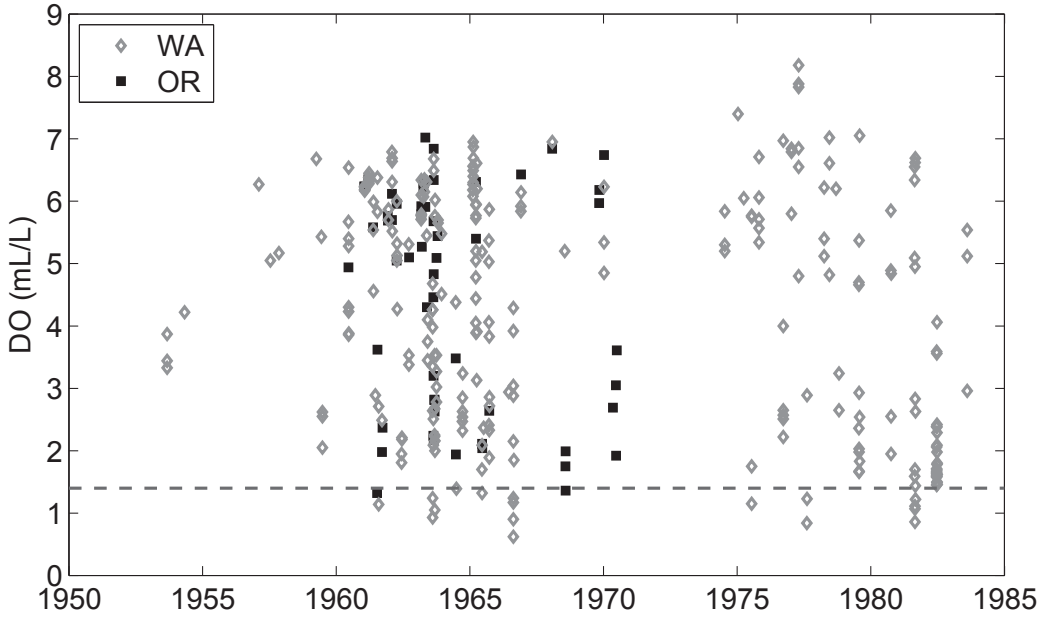

Figure 1.5: Near bottom, inner shelf (10 m from bottom or less, 40 m bottom depth or less) DO measurements for Washington (grey diamonds) and Oregon (black squares). The 1.4 mL L^{-1} definition of hypoxia is indicated by a horizontal dashed line.

Figure 1.6: Near-bottom dissolved oxygen during late summer/early fall from four different years: a) 2003, b) 2004, c) 2005, and d) 2006. DO contours, shown in the color bar in d), represent increments of 0.5 mL L^{-1}. Isobaths are indicated by grey contour lines. Station locations are shown as black dots. Abbreviations of selected transect names are shown along the Washington coast. e) Cumulative upwelling index (CUI) for the years 2003 (green), 2004 (gold), 2005 (red) and 2006 (blue). The curves show the CUI integrated from the start of the climatological upwelling season. Solid dots on the right side indicate the CUI that is obtained by integrating from the spring minimum to 26 September. The mean CUI for the years 1967–2006 is shown in solid black. The mean CUI +/- one standard deviation (σ) are shown in dashed black.

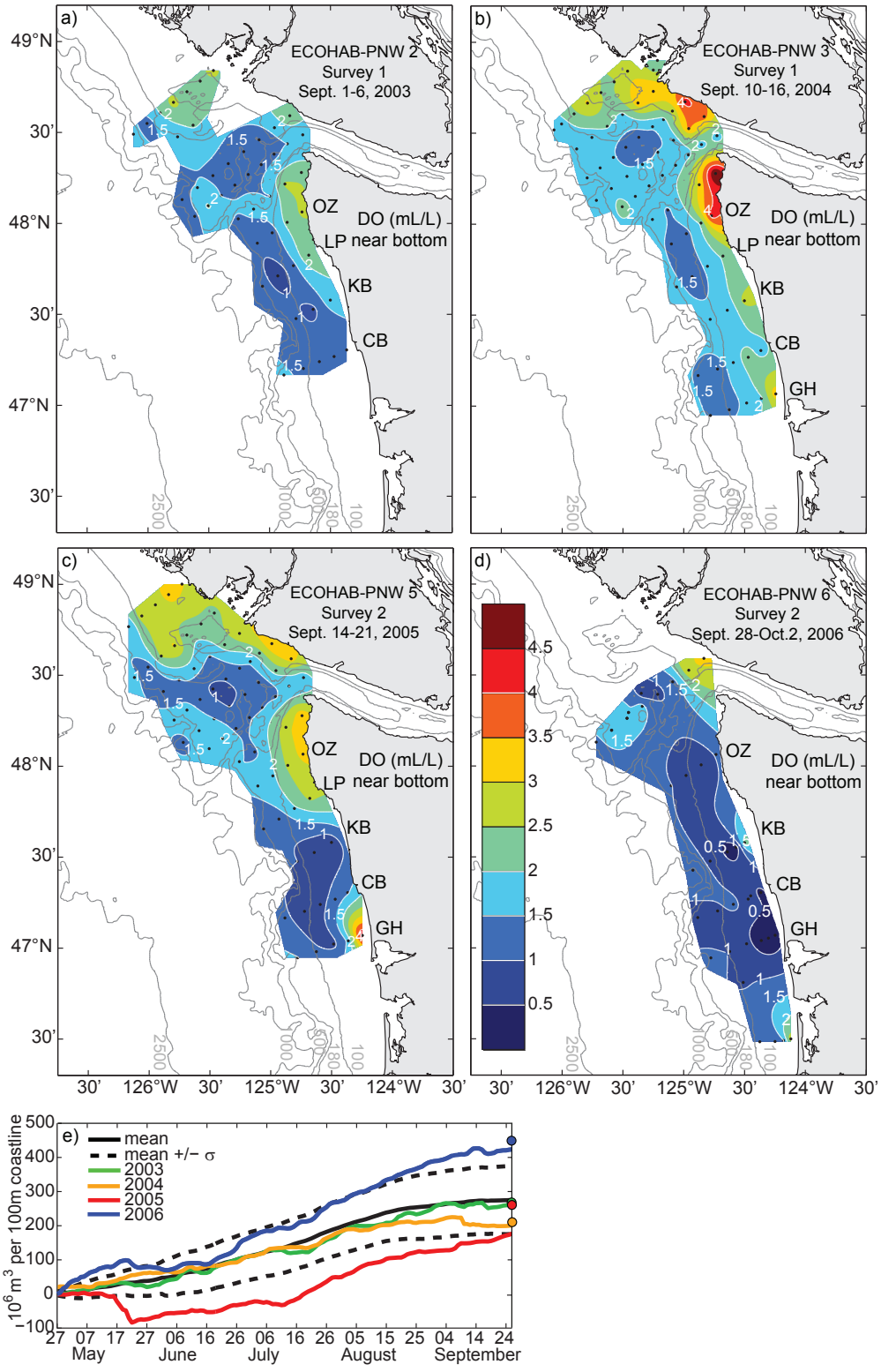
a)
ECOHAB-PNW 2
Survey 1
Sept. 1-6, 2003
b)
ECOHAB-PNW 3
Survey 1
Sept. 10-16, 2004
c)
ECOHAB-PNW 5
Survey 2
Sept. 14-21, 2005
d)
ECOHAB-PNW 6
Survey 2
Sept. 28-Oct.2, 2006
DO (mL/L)
near bottom
OZ
LP
KB
CB
GH
49°N
48°N
47°N
30'
126°W
125°W
124°W
4.5
4
3.5
3
2.5
2
1.5
1
0.5
e)
mean
mean +/− σ
2003
2004
2005
2006
10^6 m^3 per 100m coastline
500
400
300
200
100
0
−100
27 07 17 27 06 16 26 06 16 26 05 15 25 04 14 24
May
June
July
August
September

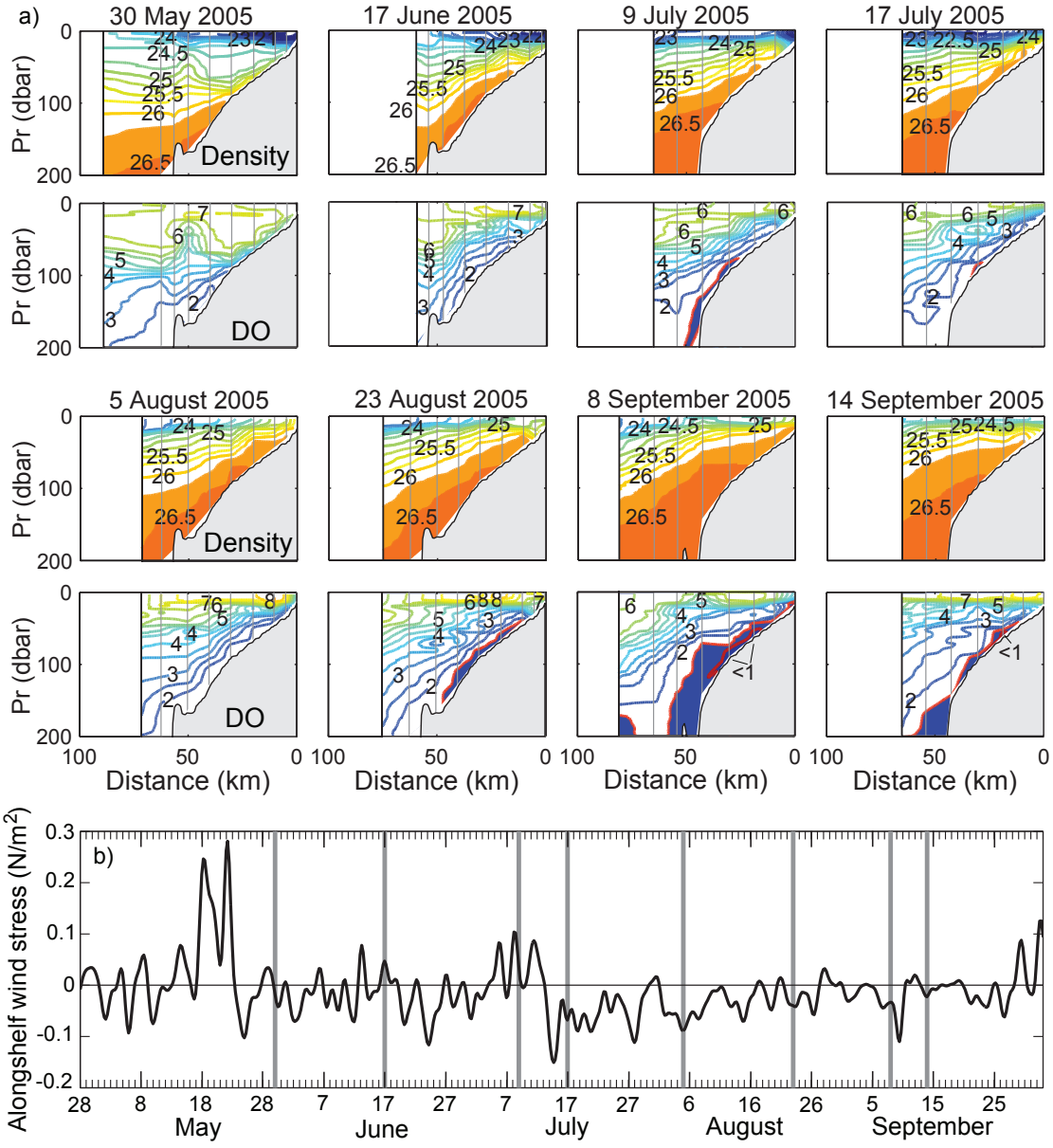

Figure 1.7: a) Seasonal progression of density (first and third row) and DO (second and fourth row) off Grays Harbor during late May through mid September 2005. Grey vertical lines indicate cast locations. Contour intervals are 0.25 kg m^{-3} and 0.5 mL L^{-1}. The 1.5 mL L^{-1} and 1.0 mL L^{-1} DO contours are highlighted in red; DO concentrations below 1.5 mL L^{-1} are shaded in dark blue. b) Wind stress at NDBC Cape Elizabeth buoy 46041 during mid May through late September 2005. Downwelling favorable wind stress is plotted as positive; upwelling favorable wind stress is negative. Grey vertical lines indicate the timing of sections.

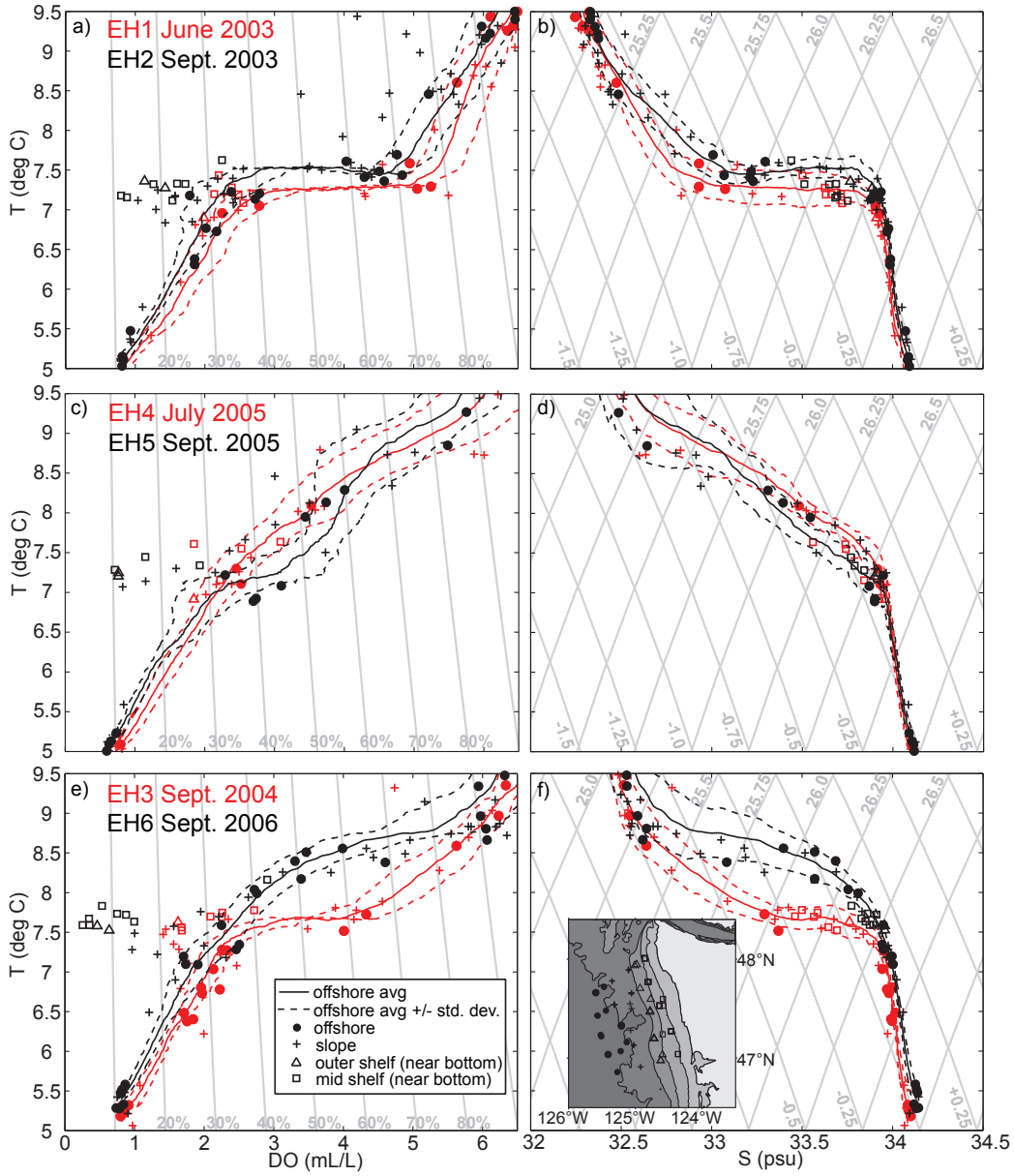

Figure 1.8: Temperature vs. DO (a,c) and temperature vs. salinity (b,d) for six different cruises over the Washington shelf: June 2003 (a,b–red), September 2003 (a,b–black), July 2005 (c,d–red), September 2005 (c,d–black), September 2004 (e,f–red) and September 2006 (e,f–black). Solid and dashed lines represent a mean profile +/- the standard deviation of DO (a,c) and T (b,d) at >1000m bottom depth. Circles and crosses represent discrete values at standard depths (50, 100, 200, 500 m) at offshore (>1000 m bottom depth) and slope (130–1000 m bottom depth) stations. Triangles and squares represent discrete near bottom values at outer and mid shelf stations. Contours in a and c represent percent saturation. Contours in b and d represent σ_t and spice. Inset map in d shows station locations for discrete samples used from ECOHAB-PNW cruises 1–6.

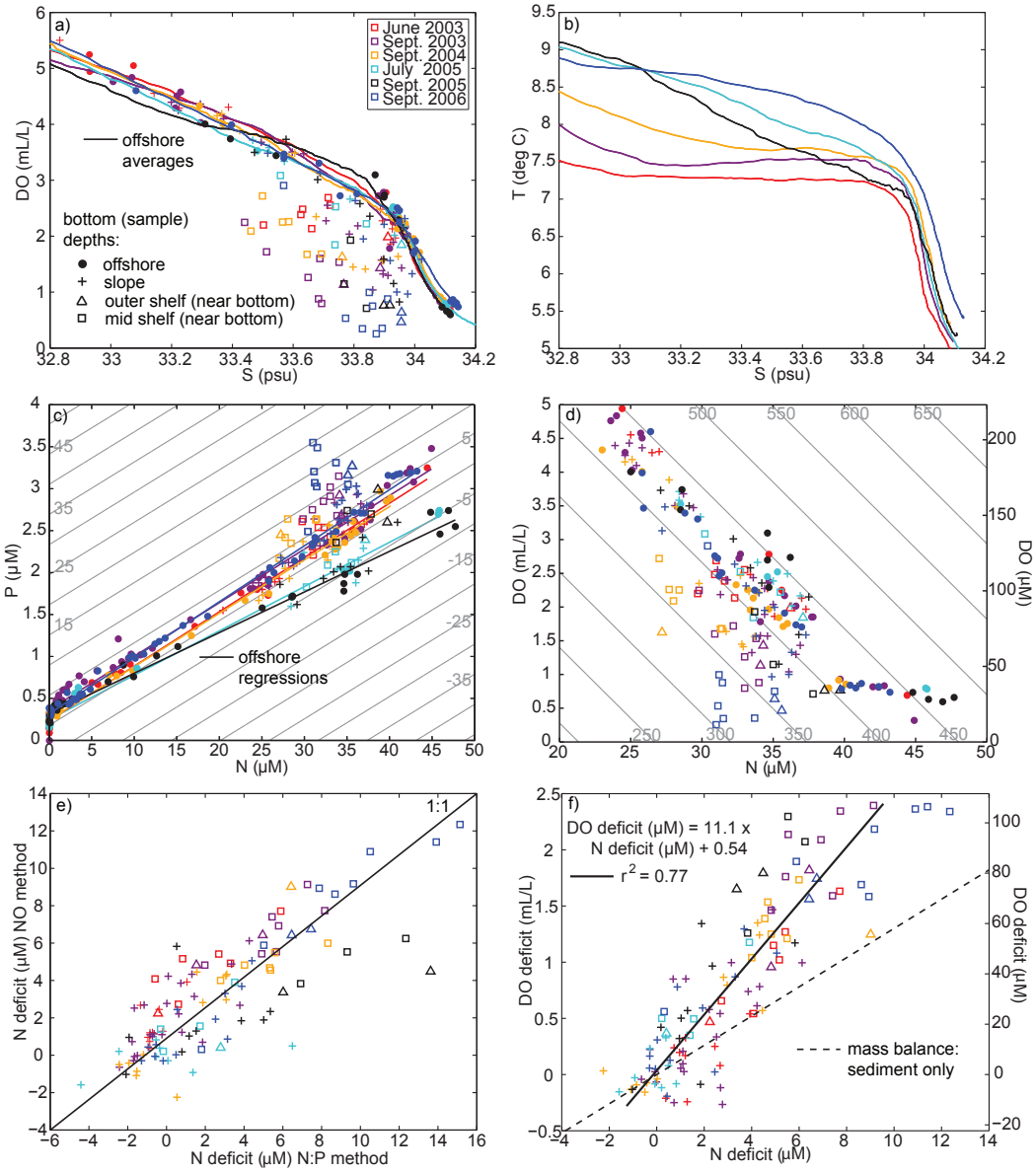

Figure 1.9: a) Salinity and DO for offshore water, slope (100–200 m) water, and near bottom shelf water. Symbols represent same range of bottom depths as Fig. 1.8. Solid lines indicate mean offshore profiles and colors represent different cruises. DO deficits are the vertical distance between discrete points and the mean offshore profile. b) Average offshore T and S relationships, same colors as in panel a. c) N and P, same colors and symbols as in panel a. Solid lines are linear regressions from offshore samples. Background contours represent constant $-$N*. N deficits are approximately equal to the distance across these contours between discrete points and the offshore regression. c) N and DO, same colors and symbols. Background contours represent constant NO. e) N deficit as calculated from the quantity NO compared with an alternate calculation based on N and P. d) Regression of DO and N deficits for slope source water and near bottom shelf water.

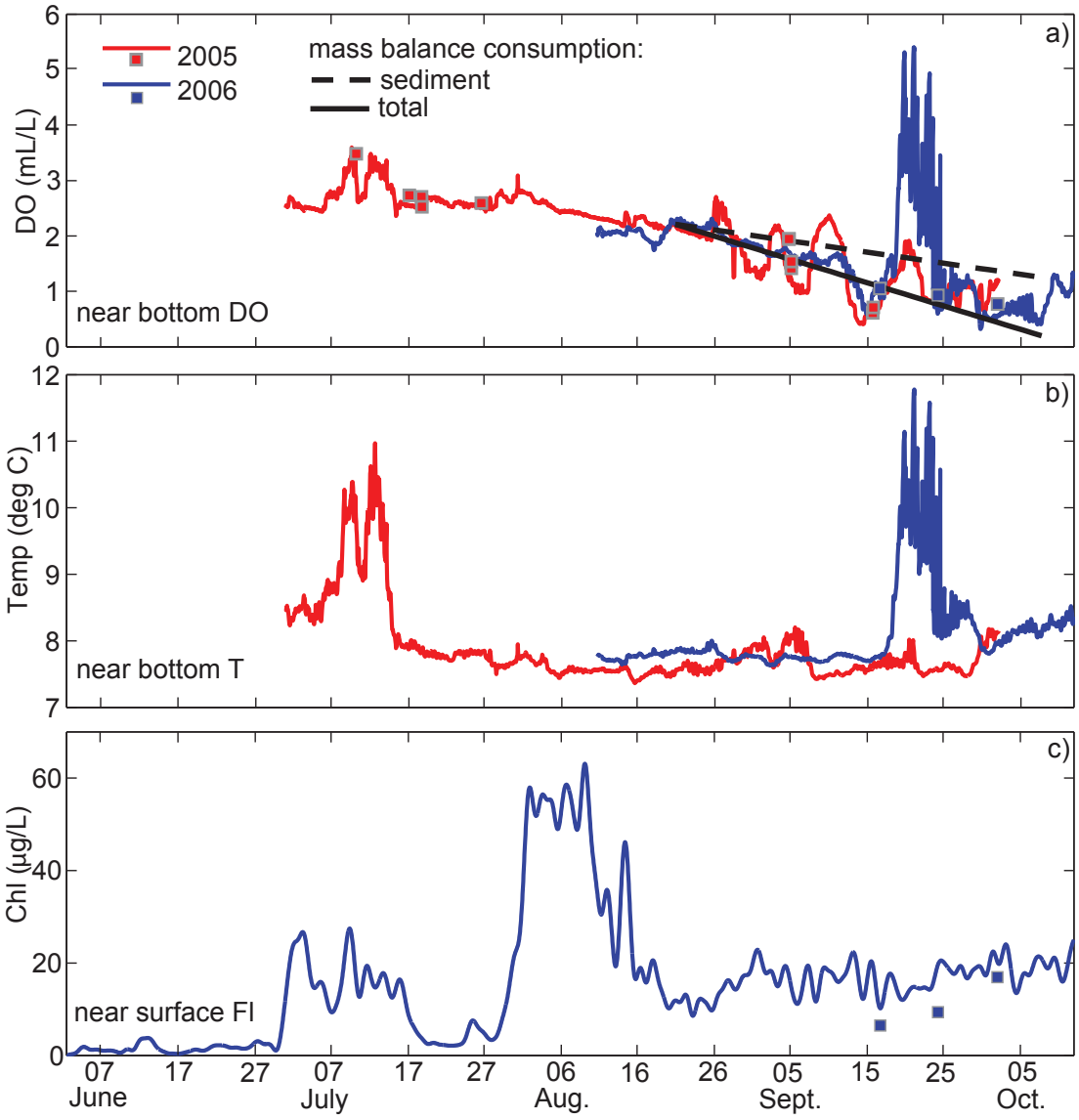

Figure 1.10: Hourly time series of near bottom DO (a) and temperature (b) at the E4 mooring location for 2005 (red lines) and 2006 (blue lines). Near bottom DO concentrations from shipboard profiles are shown as squares. Dashed black line represents consumption of DO due to sediment demand calculated in Section 1.4.2.4; solid black line represents total DO consumption. c) Near surface fluorescence at the E2 mooring for 2006. Chl *a* concentrations from bottle samples are shown as squares.

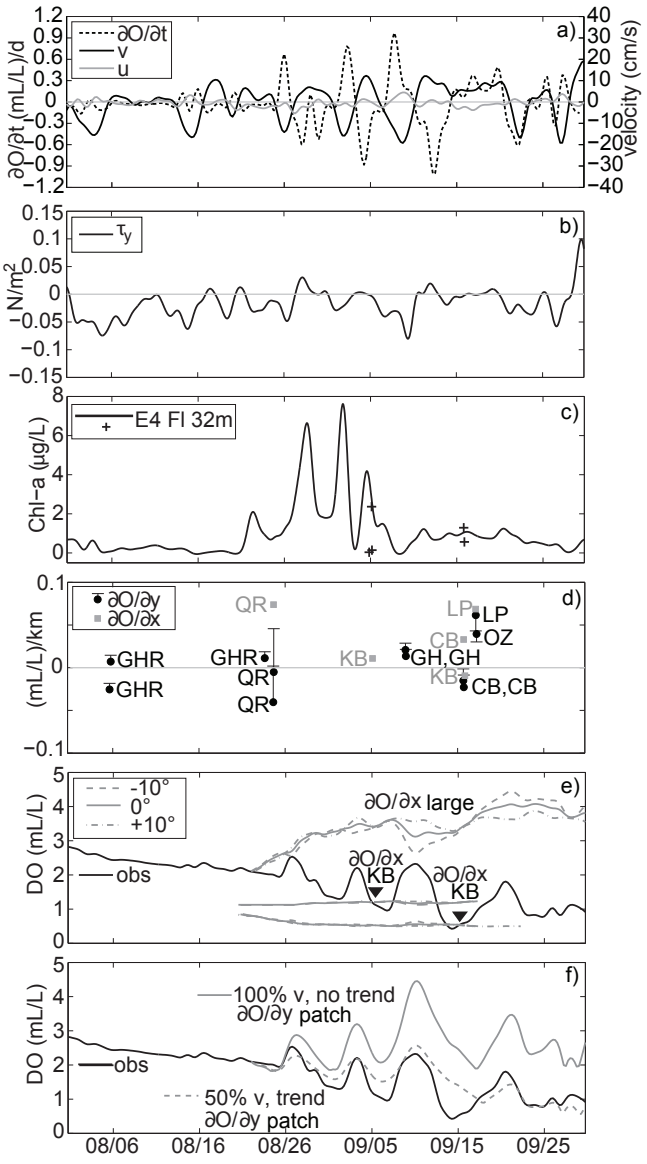

Figure 1.11: Time series during the period 31 July – 29 September 2005. a) Near bottom DO time derivative and u,v velocity components 12m above bottom at E4. b) Wind stress at NDBC Cape Elizabeth buoy 46041. c) Near bottom fluorescence at E4,with near bottom values from shipboard fluorescence profiles (crosses). d) DO spatial gradients in the x, y (grey, black) direction, with estimated error, E (see text, Section 2.4). e) Measured DO (black) compared to that predicted (grey) by both spatially variable gradients from the KB line, and a large constant cross shelf gradient, with measured u. The dash-dot and dashed lines utilize velocity coordinate systems rotated $\pm 10°$. f) Measured DO time series (black) compared to that predicted (grey) by a constant alongshelf gradient on both sides of a patch with measured v. Dashed line includes total respiration calculated from the mass balance in Section 1.4.2.4, and the velocity reduced by 50% to account for bottom friction.

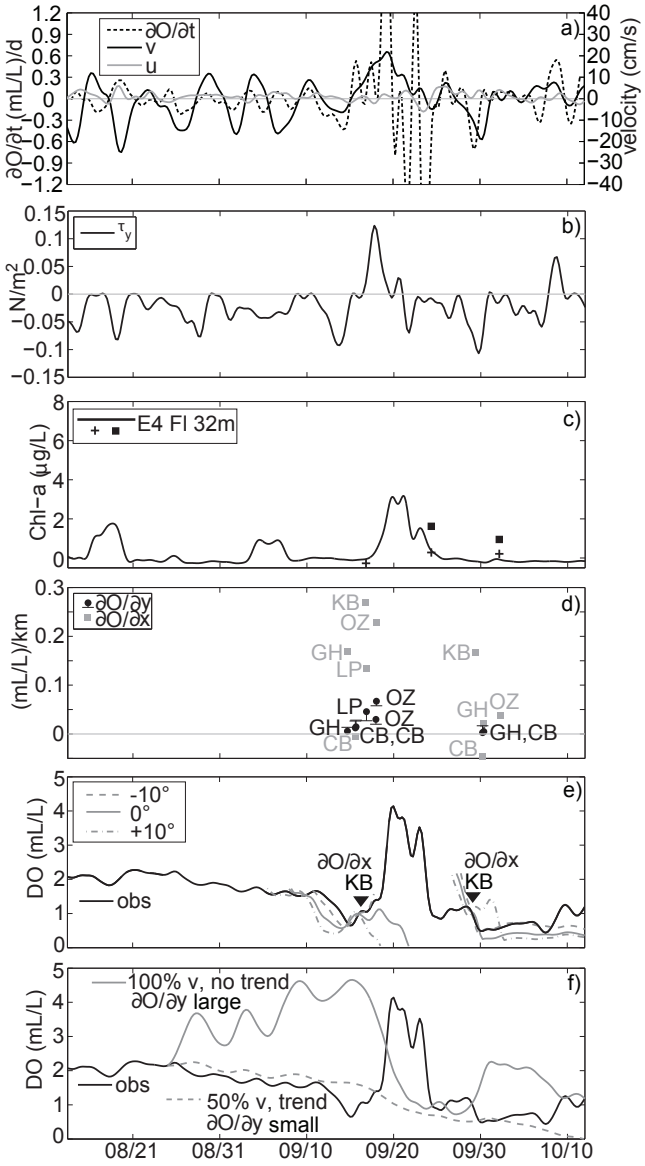

Figure 1.12: Time series during the period 13 August – 12 October 2006. a) Near bottom DO time derivative and u, v velocity components 12 m above bottom at E4. b) Wind stress at NDBC Cape Elizabeth buoy 46041. c) Near bottom fluorescence at E4,with near bottom values from shipboard fluorescence profiles (crosses) and Chl a bottle samples (squares). d) DO spatial gradients in the x, y (grey, black) direction, with estimated error, E. e) Measured DO (black) compared to that predicted (grey) by both spatially variable gradients from the KB line with measured u. The dash-dot and dashed lines utilize velocity coordinate systems rotated $\pm 10°$. f) Measured DO time series (black) compared to that predicted (grey) by a constant alongshelf gradient and measured v. Solid line uses a large positive gradient. Dashed line uses a smaller gradient, includes total respiration calculated from the mass balance in Section 4.2 d, and velocity reduced by 50% to account for bottom friction.

Chapter 2

COASTAL TRAPPED WAVES, ALONGSHORE PRESSURE GRADIENTS, AND THE CALIFORNIA UNDERCURRENT

Abstract

The California Undercurrent, a poleward-flowing feature over the continental slope, is a key transport pathway along the west coast of North America and an important component of regional upwelling dynamics. This study examines the poleward undercurrent and alongshore pressure gradients in the northern California Current System (CCS), where local wind stress forcing is weak. The dynamics of the undercurrent are compared in the primitive equation Navy Coastal Ocean Model and a linear coastal trapped wave model. Both models are validated using hydrographic data and current meter observations in the core of the undercurrent in the northern CCS. In the linear model, alongshore winds along the U.S. west coast generate poleward flow events over the slope, but reproducing the persistent poleward undercurrent during summer requires the inclusion of San Diego sea level as a southern boundary condition. The depth structure of the modeled alongshore pressure gradient varies with latitude and distance offshore. The mean baroclinic response to summer wind forcing in the CCS is strongest near 42°N, north of the strongest wind forcing. In the northern CCS, alongshore density gradients over the slope lead to a poleward pressure-gradient force within the undercurrent that often opposes an equatorward force associated with coastal sea level.

2.1 Introduction

The California Undercurrent (CUC) flows poleward over the continental slope along the eastern boundary of the North Pacific ocean, transporting heat, chemical tracers and organisms over alongshore distances of thousands of kilometers. Relatively warm, saline, oxygen-depleted water is associated with the CUC from Baja California to Alaska (Hickey,

1979; Thomson and Krassovski, 2010). These equatorial water properties are transferred into the interior of the North Pacific by eddies formed from instabilities within the CUC (Huyer et al., 1998; Garfield et al., 1999). The CUC modifies nutrient concentrations along its path by transporting water with low ratios of nitrate to phosphate (Liu and Kaplan, 1989; Castro et al., 2001), and also influences the distribution of marine organisms such as zooplankton (Swartzman et al., 2005). Poleward undercurrents similar to the CUC are common in eastern boundary current systems, and their presence can greatly affect the physical dynamics of coastal upwelling (Hill et al., 1998).

The CUC is a seasonal feature in the northern California Current System (CCS), which includes the coastal waters offshore of northern California (CA), Oregon (OR), Washington (WA) and southern British Columbia (BC). At these latitudes, the CUC has a typical volume transport of 0.5–1.5 Sv, with a 10–20 km wide subsurface core over the upper slope (Hickey, 1979; Pierce et al., 2000). In the seasonal cycle, poleward flow appears over the upper slope during July and strengthens through late October (Hickey, 1979; Thomson and Krassovski, 2010). As the upwelling season progresses from late April–early October, the core of the undercurrent shoals from below 500-m depth to the upper slope (Pelland et al., 2012, manuscript submitted to *J. Phys Oceanogr.*), and the relatively warm and saline CUC water mass forms a greater percentage of water over the shelf (MacFadyen et al., 2008). During winter, winds are downwelling-favorable, contributing to the surface-intensified poleward flow over the slope commonly known as the Davidson Current (Hickey, 1979). The spring transition to equatorward flow precedes the transition to upwelling-favorable wind stress, and seasonal flow over the upper slope becomes predominantly equatorward at all depths during April–June (Thomson and Krassovski, 2010). The equatorward coastal jet near the surface and local upwelling-favorable wind stress both peak during July.

The CUC influences the seasonal dynamics of coastal upwelling in the CCS because of its relationship to the alongshore pressure gradient and the bottom boundary layer. In the northern CCS, the alongshore pressure-gradient force (APF) inferred from observations of coastal sea level is directed equatorward during winter and spring, and becomes poleward during the summer upwelling season (Hickey and Pola, 1983). Imposing a poleward APF in two-dimensional models of coastal upwelling produces a poleward undercurrent over the

slope and shifts the depth of onshore flow from the bottom boundary layer to the interior (Werner and Hickey, 1983; Federiuk and Allen, 1995). Similarly, Pringle and Dever (2009) found that incorporating a realistic CUC into a three-dimensional regional hindcast model leads to shallower source depths for upwelling. During spring, the APF at the coast is directed equatorward, in the same direction as the wind stress (Hickey and Pola, 1983), which results in equatorward flow throughout the water column (Werner and Hickey, 1983). Idealized modeling studies of upwelling ecosystems and biogeochemistry often use an externally applied poleward APF to incorporate undercurrent dynamics (Lathuilière et al., 2010; Siedlecki et al., 2012), but the appropriate spatial variation of the APF in the vertical and cross-shore directions remains unconstrained.

Despite the prevalence and importance of eastern boundary poleward undercurrents like the CUC, their dynamics are not fully understood. Hill et al. (1998) groups proposed mechanisms for their existence into three major classes: 1) a response to wind stress near the coast, 2) pressure gradients originating in the open ocean, and 3) rectification of oscillating flow over complex topography. The first two mechanisms depend on a large-scale poleward APF. In idealized wind driven models with stratification, a poleward APF and undercurrent can be generated if the upwelling favorable winds have an alongshore structure, an idea first recognized by Yoshida (1967). However, an open-ocean pressure gradient associated with a poleward decrease in temperature and sea surface height can also be associated with a poleward flow over the slope (Huthnance, 1984; Csanady, 1985). In the third mechanism, shelf wave propagation leads to an asymmetrical distribution of pressure across topographic features in the time mean, generating poleward mean flow at eastern ocean boundaries through topographic drag (Haidvogel and Brink, 1986). The absence of a clearly defined mechanism for undercurrent generation continues due to the low number of velocity time series over the slope and the difficulty in obtaining measurements of the APF.

In the theoretical work that emphasizes wind forcing of poleward undercurrents, coastal trapped waves (CTWs) play an important role. CTWs can be thought of as hybrids of internal Kelvin waves and barotropic continental shelf waves (Wang and Mooers, 1976). In Kelvin waves, over a flat bottom, alongshore pressure gradients accelerate alongshore motions near a coastal wall. In shelf waves, cross-shelf motions act to conserve potential

vorticity over a sloping bottom. CTWs take on more "Kelvin-like" characteristics with increasing bottom slope and stratification and decreasing latitude, devoting a greater portion of energy to the vertical displacement of fluid than "shelf-like" waves (Brink, 1982, 1991). Higher modes also tend to be more Kelvin-like than lower modes, and propagate more slowly.

The undercurrent is a robust feature of models forced by wind stress in a region of limited alongshore extent. In stratified models with a coastal wall and flat bottom, Kelvin waves are generated at the southern edge of the forcing region, and the poleward APF that accelerates the undercurrent is set up in their wake after a few days (McCreary, 1981; Philander and Yoon, 1982). In the forced region and at low frequencies, these waves propagate with phase speeds twice as fast as free waves (Philander and Yoon, 1982). In a two-layer model, the introduction of a continental shelf leads to two CTW modes: a shelf wave associated with vortex stretching that strengthens the coastal jet near the coast, and a slower mode associated with interface displacement that accelerates the undercurrent (Suginohara, 1974). The response is similar with continuous stratification; a poleward undercurrent develops in the time interval between the arrivals of first and second mode CTWs (Suginohara, 1982). The passage of the second mode wave reduces the acceleration of alongshore currents and brings the mass balance closer to two-dimensional. Eventually, higher modes shut down the undercurrent entirely, although the undercurrent persists longer in the northern part of the forcing region, where both poleward and equatorward flow are stronger (Suginohara and Kitamura, 1984). In some cases, wave propagation extends the undercurrent north of the forcing region, although the inclusion of shelf topography has been shown to weaken its strength and limit its northward extent (McCreary, 1981; McCreary and Chao, 1985).

The essential ingredients for wind-driven poleward undercurrents are alongshore structure in the wind forcing, which creates alongshore pressure gradients, and stratification, which allows vertical shear in the alongshore currents. With these basic factors included, the two-layer analytical model of Yoshida (1980) produces a poleward undercurrent in nearly the entire range of length scales and frequencies. Exceptions include an infinitely long forcing length scale corresponding to the two dimensional case, extremely short forcing length scales approaching the deformation radius, and resonance between propagating wind forcing

and the barotropic Kelvin wave. The β-effect is not essential for undercurrent formation, but offshore Rossby wave propagation can lead to a shallowing and intensification of the undercurrent (Suginohara and Kitamura, 1984; McCreary and Chao, 1985; Marchesiello et al., 2003). Positive wind stress curl near the coast on a β-plane can also strengthen the undercurrent by inducing poleward Sverdrup transport (McCreary and Chao, 1985; Batteen, 1997).

The seasonal acceleration of the CUC in the northern CCS shown by Thomson and Krassovski (2010) is qualitatively consistent with the seasonal cycle of the alongshore pressure gradient inferred from sea level (Hickey and Pola, 1983). Hickey and Pola (1983) attributed the sea level gradient in the northern CCS to the alongshore structure of wind stress using the steady barotropic model of Csanady (1978). This structure in wind stress, with a maximum off northern CA, has been linked to the CUC and a poleward APF in the idealized models described above. However, direct comparisons with observed variability in the CUC have been limited, making it difficult to rule out other mechanisms of producing poleward flow. Furthermore, because the APF is difficult to measure away from the coast, its structure and variability over the slope remain poorly understood.

The goals of of this paper are to investigate the spatial and temporal structure of 1) the poleward slope undercurrent and 2) the alongshore pressure gradient along the U.S. west coast. Emphasis is placed on the development of the CUC in the northern portion of the CCS, where local wind stress forcing is weak. The analysis uses two numerical hindcasts with different levels of complexity. The spatially complex Navy Coastal Ocean Model of the CCS (NCOM-CCS) is used to more fully understand the pressure field over the continental slope. In addition, a linear coastal trapped wave (CTW) model is used, which is forced by time variable winds along the coast but excludes the effects of complex topography, open-ocean forcing, wind stress curl and the β-effect. In spite of its limitations, this model can be directly compared with observations and includes the basic ingredients in wind-driven theories of undercurrent generation (e.g. McCreary, 1981): alongshore structure in wind stress, alongshore pressure gradients and stratification. The northern CCS is an ideal location for testing an f-plane model forced by alongshore wind stress because it is thought to be located north of latitudes where seasonal Rossby wave propagation occurs (Pares-

Sierra and O'Brien, 1989; Clarke and Shi, 1991; Kelly et al., 1993) and wind stress curl is relatively weak (Bakun and Nelson, 1991).

Both models are compared with an extensive array of observations, including currents from moored sensors and hydrographic data (Section 2.3). The configuration of the CTW model is adjusted to show sensitivity of the seasonal cycle to friction, number of modes, local wind stress and the southern boundary condition (Section 2.4.1). The modeled APF is then examined near the coast and over the slope (Section 2.4.2). Finally, the dynamics of the CUC and the large scale APF are connected through analysis of the alongshore momentum balance (Section 2.4.3).

2.2 Methods

2.2.1 Observations

2.2.1.1 Coastal sea level

Coastal sea level time series were obtained for 11 tide gauge locations (Fig. 2.1a) for the year 2005 and at San Diego for the years 1987-2008. Tide gauge heights were adjusted by adding equivalent sea level pressure (0.01 m per mbar atmospheric pressure) measured at nearby stations (Fig. 2.1a) in order to estimate subsurface pressure. Hourly time series were low pass filtered using a cosine Lanczos filter with half power point of 46 hours and decimated every six hours. Mean values are removed so that time series represent anomalies, not absolute displacement from a geopotential surface. Tide gauge data were obtained from the U.S. National Ocean Service and the Canadian Tides and Water Levels Data Archive. Atmospheric pressure data were obtained from the National Buoy Data Center for U.S. locations and the National Climate Data Center for Canadian locations.

2.2.1.2 Mooring time series

Velocity data are used from two locations on the British Columbia slope and the Washington shelf (Fig. 2.1b). The A1 mooring, where data has been collected 1985 through the present, is located on the 500-m isobath at 48°32'N, 126°12'W (Thomson and Krassovski, 2010). During 2004 and 2005, velocity data were collected at nominal depths of 35 m, 100 m,

175 m and 300 m using Aanderaa RCM8 current meters, although actual current meter depth and data availability vary between deployments. Velocity components were rotated 25° counter-clockwise, parallel to the local isobath orientation, and time series were filtered using a Kaiser low pass filter with 30 hour cutoff and decimated to daily intervals. The RN mooring is located on the 70-m isobath at 47°00'N, 124°30'W. Velocity components at the RN site were rotated 10° clockwise, and time series were filtered and decimated in the same manner as coastal sea level.

2.2.1.3 Geostrophic velocity

Conductivity, temperature and depth (CTD) measurements were obtained during September 2005 as part of the Ecology and Oceanography of Harmful Algal Blooms-Pacific Northwest (ECOHAB-PNW) project (MacFadyen et al., 2008). Geostrophic velocity, referenced to 500 dbar, was calculated using the method of Reid and Mantyla (1976).

2.2.2 Models

2.2.2.1 Navy Coastal Ocean Model

We present numerical hindcast results for 2005 from the Navy Coastal Ocean Model for the California Current System (NCOM-CCS), a data-assimilating primitive equation model. The domain covers the region 30-49°N, 135-115°W at 9-km horizontal resolution (Fig. 2.1a,b). Atmospheric forcing is provided by the Coupled Ocean / Atmosphere Mesoscale Prediction System (COAMPS) model (Hodur, 1997). There is no tidal forcing or river input, and the Strait of Juan de Fuca, which connects the Pacific Ocean to Puget Sound and the Strait of Georgia, is closed off by a strait coastline. The model uses satellite-derived sea surface temperature for data assimilation and open boundary information is provided by the 1/8° resolution global NCOM model (Kara et al., 2006). Schulman et al. (2003) provide a detailed description of the NCOM-CCS model, including sensitivity to different formulations of atmospheric forcing and boundary conditions. In the version used here, the vertical coordinate system is comprised of 40 levels total, 19 σ (terrain-following) levels on top of 21 z (constant depth) levels (Barron et al., 2006). Use of z levels below 137 m, approximately

the depth of the shelf break, avoids errors in calculation of the pressure gradient that can arise near steep topography when using σ coordinates (Haney, 1991).

2.2.2.2 Coastal trapped wave model

A CTW model is used to further isolate mechanisms for subinertial variability in velocity and sea level along the west coast. Derivation and application of CTW theory is discussed extensively by Clarke and Van Gorder (1986), and will only be summarized briefly here. Time dependent effects of alongshore wind stress and the APF are included in the model, along with rotation, continuous stratification, bottom slope and weak bottom friction. Wind stress curl and the β-effect are neglected. The flow is assumed to be linear and Boussinesq, with gradually varying topography in the alongshore direction.

The coordinate system is aligned such that x is cross-shore distance from the coast (positive onshore), y is alongshore position (positive north) and z is vertical position (positive upward). The problem is greatly simplified in the long wave limit, in which cross-shelf scales are assumed to be much shorter than alongshelf scales ($\partial^2/\partial y^2 \ll \partial^2/\partial x^2$) and time scales of variability much longer than the inertial period ($\partial^2/\partial t^2 \ll f^2$, where f is the Coriolis frequency). Turbulent stresses are restricted to infinitesimally thin boundary layers at the surface and bottom. The equations of motion in the inviscid interior water column are given by

$$-fv = -\frac{1}{\rho_o} p_x \tag{2.1}$$

$$v_t + fu = -\frac{1}{\rho_o} p_y \tag{2.2}$$

$$0 = -p_z - g\rho' \tag{2.3}$$

$$0 = u_x + v_y + w_z \tag{2.4}$$

$$0 = \rho'_t + w\bar{\rho}_z \tag{2.5}$$

where u is cross-shore velocity, v is alongshore velocity, w is vertical velocity, p is pressure and g is the acceleration due to gravity. Subscripts denote partial differentiation. Density

is separated into a constant background density ρ_o, a vertically-varying background state $\bar{\rho}(z)$, and perturbations $\rho'(x, y, z, t)$. In terms of pressure, this system can be written as

$$p_{xxt} + f^2(p_{zt}/N^2)_z = 0 \tag{2.6}$$

where $N(z)$ is the buoyancy frequency. Boundary conditions for the system are given by

$$p_z + \frac{N^2}{g}p = 0 \text{ at } z = 0, \tag{2.7}$$

$$p_{xt} + \frac{rp_x}{h} + fp_y = \frac{f\tau^y}{h} \text{ at } x = 0, \tag{2.8}$$

$$\frac{f^2 p_{zt}}{N^2} + h_x(p_{xt} + fp_y) + (rp_x)_x - h_x r p_{xz} = 0 \text{ at } z = -h(x), \text{ and} \tag{2.9}$$

$$p_x = 0 \text{ as } x \to \infty, \tag{2.10}$$

where where $\tau^y(y, t)$ is the alongshore component of wind stress, $h(x)$ is bottom depth, and r is a linear friction coefficient such that the bottom stress $\tau_b^y = \rho_o r v$. These boundary conditions represent a free surface (2.7), no net transport at the coastal wall (2.8), Ekman transport and no normal flow at the bottom (2.9), and coastal trapping (2.10).

Solutions for pressure are separated into orthogonal components,

$$p(x, y, z, t) = \sum_{n=1}^{\infty} F_n(x, z)\phi_n(y, t), \tag{2.11}$$

where F_n is the free-wave structure of the nth mode, and ϕ_n is the amplitude of the nth mode response. The free-wave structure of each mode is obtained by solving the frictionless eigenvalue problem,

$$F_{n_{xx}} + f^2(F_{n_z}/N^2)_z = 0, \tag{2.12}$$

with boundary conditions

$$F_{n_z} + \frac{N^2}{g}F_n = 0 \text{ at } z = 0, \tag{2.13}$$

$$F_{n_x} + f{c_n}^{-1}F_n = 0 \text{ at } x = 0, \tag{2.14}$$

$$F_{n_z} + \frac{N^2}{f^2}h_x(F_{n_x} + f{c_n}^{-1}F_n) = 0 \text{ at } z = -h(x), \text{ and} \tag{2.15}$$

$$F_{n_x} = 0 \text{ as } x \to \infty, \tag{2.16}$$

where c_n is the phase speed of the nth mode. The amplitude of the propagating wave response for each mode satisfies

$$\phi_{ny} - \frac{1}{c_n}\phi_{nt} + a_{nn}\phi_n + \sum_{\substack{m=1 \\ m\neq n}}^{\infty} a_{nm}\phi_m = b_n \tau^y(y,t), \tag{2.17}$$

where b_n is a wind coupling coefficient, a_{nn} is a frictional decay coefficient, and a_{nm} are coefficients for frictional coupling to the mth mode. The free wave properties F_n, c_n, b_n and a_{nm} are calculated using the bottom topography $h(x)$ and mean stratification $N^2(z)$ at ten coastal segments (Fig. 2.1c) using MATLAB programs provided by Dr. Kenneth Brink (WHOI), which are similar to the FORTRAN software described by Brink and Chapman (1987). In this version of the CTW software, wind coupling coefficients b_n and frictional coefficients a_{nm} are calculated using the energy-conserving normalization of Brink (1989).

Mean $N^2(z)$ profiles were computed from CTD data in the World Ocean Database (Boyer et al., 2006), using casts offshore of the 1000-m isobath but no further than 400 km offshore in the area closest to each segment. Previous studies have shown that varying stratification produces small ($< 10\%$) changes in F_n, c_n and b_n in the long-wave limit, but can change a_{nm} by up to 100% (Battisti and Hickey, 1984; Chapman, 1987). Bottom topography is from the National Geophysical Data Center coastal relief model (Divins and Metzger, 2008). Wind stress was calculated using the formula of Large and Pond (1981) from wind velocity interpolated to the inshore 50 km of each segment from the Cross Calibrated Multiplatform Product (Fig. 2.1c), which incorporates data from the QuikScat scatterometer and coastal buoys (Atlas et al., 2010).

Solutions to the coupled equations in (2.17) are obtained numerically by integrating along wave characteristics using the trapezoidal method described by Clarke and Van Gorder (1986). Using $\Delta y = 2.5$ km and $\Delta t = 6$ hours resolves the slowest phase speed in the model (0.39 m s^{-1} for the fourth mode off southern California). The CTW model is run for the years 1988–2008, with results from 1988 discarded as spin-up. Unless otherwise stated, the infinite sums in (2.11) and (2.17) are approximated using four modes. A constant linear friction coefficient $r = 2.5 \times 10^{-4}$ m s^{-1} is used for the calculation of a_{nm}, the value

used for the continental slope by Chapman (1987). At the southern boundary, $\phi_1(0,t) = \rho_0 g\eta(t)/F_1(0,0)$, where ρ_0 is a reference density and adjusted sea level at San Diego is used for $\eta(t)$. This relationship assumes that San Diego sea level is dominated by the first mode. Sensitivity to the number of modes, friction coefficient, presence of local wind stress and the use of sea level data at the southern boundary will be explored.

2.3 Model validation

This analysis uses results from two different numerical hindcast models. The NCOM-CCS model is fully nonlinear and three-dimensional, incorporating large-scale dynamics, complex bathymetry, β-plane dynamics, and wind stress curl on a 9-km grid. The CTW model is restricted to linear, f-plane, coastally-trapped dynamics with gradual variations in bottom topography and alongshore wind stress. Before using the models to extend prior work on the dynamics of the CUC and structure of the APF, the models will be carefully validated with observations. The models are first compared with observed time series of alongshore velocity at the RN mooring over the WA mid shelf (Fig. 2.1b), where previous studies have demonstrated the importance of CTW dynamics (Battisti and Hickey, 1984). To assess the variability and strength of the modeled California Undercurrent, the models are also compared with time series at the A1 mooring over the British Columbia slope (Fig. 2.1b). The CTW model seasonal cycle, averaged over two decades, is compared with observational studies of the seasonal cycle over the British Columbia slope (Thomson and Krassovski, 2010; Pelland et al., 2012, manuscript submitted to *J. Phys Oceanogr.*).

2.3.1 Mid shelf: equatorward coastal jet

During June–September 2005, observed currents were predominantly equatorward in the middle of the water column over the WA shelf (Fig. 2.2a). During 2005, an anomalously late spring transition in local wind stress occurred during late May, with relatively weak upwelling-favorable winds continuing through mid-July (Hickey et al., 2006; Kosro et al., 2006). During 15 June–15 September, the NCOM-CCS model shows equatorward depth-averaged currents over the broad continental shelves of the northern CCS, unlike other locations with narrower shelves where depth-averaged flow is poleward near the coast (Fig.

2.1b). Reversals to poleward flow do occur during this period over the WA shelf, becoming more frequent during September (Fig. 2.2a).

Statistical agreement between the models and observations is quantified using both correlation coefficients (CC) and Willmott skill (WS). Time series were detrended before computing correlation coefficients and significance levels were determined using effective degrees of freedom (Emery and Thomson, 2004, p. 260). The WS metric is designed to compare different models, and accounts for errors due to model bias and differences in variance. WS varies between 0–1 and is defined as

$$\mathrm{WS} = 1 - \frac{\langle (m-o)^2 \rangle}{\langle (|m - \langle o \rangle| + |o - \langle o \rangle|)^2 \rangle}, \tag{2.18}$$

where m is a modeled variable, o is an observed variable, and $\langle\rangle$ denotes an average over the series (Willmott, 1981).

Correlations between the NCOM-CCS model and RN observations are similar throughout the water column (CC = 0.68–0.74) (Fig. 2.3a). Correlation with the CTW model is strongest in the lower half of the water column (CC = 0.61–0.66) (Fig. 2.3a). All correlations are significant at the 95% confidence level. A similar increase with depth in the correlation between a CTW model and observations was reported by Chapman (1987) over the California shelf. Profiles of WS from the two different models indicate that the CTW model generally has weaker skill, particularly in the lower part of the water column (Fig. 2.3a). The CTW model most accurately predicts the timing of fluctuations near the bottom, but the magnitude of the modeled velocity agrees more closely with observations near the surface.

2.3.2 Slope: California Undercurrent

During 2005 at the A1 site on the continental slope, the strongest equatorward flows at 300-m depth were observed during late May, following the transition in local wind stress (Fig 2.2b). By mid-July, the flow is predominantly poleward, but with considerable event-scale variability throughout the time series. Both models show a transition from equatorward to poleward flow at this depth during summer 2005, although the CTW model tends to

overestimate the magnitude of the equatorward flow (Fig. 2.2b). To provide further context for seasonal variability, observations and CTW model time series are shown over a greater depth range for the full year 2004. The time series indicate a similar seasonal progression as in 2005, with the strongest equatorward flow observed during April at 100 m (Fig. 2.4). However, at 35 m, observed equatorward velocities exceed 0.2 m s^{-1} during July. The summer maximum in equatorward velocity at 35 m is not reproduced in the CTW model, in which velocity patterns are similar for all depths.

Model-observation comparisons were quantified over the slope using the same statistics as over the shelf in the previous section. Once again, all correlations shown are significant at the 95% confidence level. Three subsets of the model runs shown in Fig. 2.2 and Fig. 2.4 are directly compared: 2005 NCOM-CCS, 2005 CTW and 2004 CTW. In Fig. 2.3b, statistics were calculated wherever observational data is available; comparisons therefore extend over time periods several months longer than the RN time series that are available over the shelf. For both models, largest correlation coefficients occur at 100 m (Fig. 2.3b). Both statistics indicate that the NCOM-CCS model outperforms the CTW model at 300 m.

If comparisons are restricted to the same time period as the 2005 RN measurements discussed in the previous section, the correlation with observations improves for both models at all depths, particularly the NCOM-CCS model (Fig. 2.3c). The WS metric indicates that both models have relatively strong skill ($\sim$0.8) at 300 m and weak skill ($\sim$0.3) at 35 m. The weak skill at 35 m indicates that the models do not accurately represent the strength and/or cross-shelf position of the equatorward shelf-break jet at the A1 site. At 300 m, the modeled seasonal progression from equatorward to poleward flow results in strong skill during this time period.

A hydrographic section offshore of Copalis Beach, WA (47° 18' N, 124° 22' W) shows the spatial distribution of alongshore velocity on 15 September 2005 (Fig. 2.5a). Over the slope, the observed core of the CUC is located at 200-m depth with velocity 0.06 m s^{-1}. Equatorward flow is present over the outer shelf and slope, and is strongest near the surface over the 100-m isobath. Although poleward flow is present over the slope in both models (Fig. 2.5b,c), only the NCOM-CCS model shows the appropriate distribution of

equatorward flow. The CTW model shows no evidence of the ∼0.3 m s^{-1} near-surface jet that extends over the outer shelf and slope, unlike the NCOM-CCS model off WA (Fig. 2.5b,c). The weak skill at 35 m over the British Columbia slope in the NCOM-CCS model (Fig 2.3c) may be related to the more complex topography near La Perouse Bank.

2.3.3 Seasonal cycle: 1989-2008

Bimonthly averages of the 1989-2008 alongshore velocity from the CTW model show spatial patterns of the modeled seasonal circulation across the British Columbia shelf and slope (Fig. 2.6), which can be compared with observed seasonal cycles over the British Columbia slope from the A1 mooring during 1985–2004 (Thomson and Krassovski, 2010) and glider transects during 2003–9 (Pelland et al., 2012, manuscript submitted to *J. Phys Oceanogr.*). Across the entire shelf and slope in the CTW model, alongshore currents transition from poleward during January–February to equatorward during March–April. This timing is consistent with bimonthly averages from the glider transects and the A1 mooring seasonal cycle. A poleward undercurrent develops in the CTW model during July–August. This timing of undercurrent development over the upper slope is consistent with a transition to poleward flow during early July at 175 m in the A1 mooring observations. Below this depth, the glider transects show poleward flow over the slope during May–June at depths >500 m, which does not appear in the CTW seasonal cycle. During September–October, mean poleward flow strengthens to 0.06 m s^{-1} within a subsurface core at 400 m. Although the strength of the modeled poleward flow is consistent with observations, glider transects show a shallower (∼250 m) undercurrent core. As noted in the previous section, the CTW seasonal cycle does not reproduce the observed equatorward shelf break jet over the slope, which reaches a seasonal mean velocity of −0.15 m s^{-1} at the A1 mooring location. The CTW seasonal cycle is most consistent with observations over the upper slope, where the CUC core is located.

2.4 Results

Comparisons with observations in the previous section indicate that the CTW and NCOM-CCS models capture key features of summer circulation, including equatorward flow at mid

shelf during summer and variability in the California Undercurrent at time scales from days to seasons. The weakest aspect of the models is the equatorward shelf break jet. This feature is completely absent from the CTW model but is present over the Washington slope in the NCOM-CCS model (Fig. 2.5). In order to gain insight into the linear dynamics of the modeled undercurrent, the CTW model is run under different configurations to explore sensitivity of the 2005 time series and the seasonal cycle to friction, number of modes, local wind forcing and the southern boundary condition (Section 2.4.1). Both models are then used to determine the large-scale structure of the APF during summer (Section 2.4.2) and the balance of alongshore momentum in the northern CCS (Section 2.4.3).

2.4.1 CTW model sensitivity analysis

2.4.1.1 Friction

Previous studies, which focused on the shelf, have shown that the value of the linear frictional coefficient can influence the amplitude and phase of modeled velocity fluctuations (Battisti and Hickey, 1984; Chapman, 1987). In order to examine how friction modifies the response over the shelf and slope, the original value of $r = 2.5 \times 10^{-4}$ m s^{-1} was reduced to $r = 1.0 \times 10^{-4}$ m s^{-1}, and also increased by the same amount to $r = 4.0 \times 10^{-4}$ m s^{-1}. The weaker frictional coefficient greatly enhances the modeled equatorward velocity in coastal jet over mid-shelf, which reaches -0.6 m s^{-1} during early June (Fig. 2.7a, first row), much larger than observed peak velocity of -0.3–0.4 m s^{-1} (Fig. 2.2a). An equivalent increase in r has a smaller effect on the strength of equatorward flow over mid shelf (Fig. 2.7a, first row). At 300 m over the slope, decreasing r enhances poleward flow and increasing r reduces the magnitude of poleward flow during late summer (Fig. 2.7b, first row), with resulting differences <0.05 m s^{-1}.

2.4.1.2 Number of modes

The number of modes used varies substantially between different studies. Battisti and Hickey (1984) used only one mode for the Washington shelf, but Clarke and Van Gorder (1986) required seven modes for convergence of velocity over the west Florida shelf. In this

study, convergence was found for three modes and more. During mid July–October 2005, the use of two or more modes enhances equatorward flow over the shelf (Fig. 2.7a, second row) and enhances poleward flow at 300 m over the slope (Fig. 2.7b, second row). During June and early July, the first mode dominates the response. Higher modes tend to be locally generated because they have greater values of a_{mn} and are preferentially damped as they travel away from the forcing region. Therefore the higher modes tend to be more important after the onset of strong local wind stress in mid-July.

2.4.1.3 Local wind stress

To further explore the role of local wind stress, the CTW model was run with wind forcing $\tau^y = 0$ at locations north of 42°N. This configuration retains the relatively strong wind forcing off northern California, and removes the relatively weak forcing north of Cape Blanco, OR (Fig. 2.1c). Over the shelf (Fig. 2.7a, third row), remote wind forcing causes strong equatorward flow ($v \simeq 0.4$ m s^{-1}) during early June. However, the remotely-driven shelf velocity later in the summer during August is weak, with more frequent poleward flow events. In contrast to the shelf, removing the local wind stress has little effect on the flow over the slope at 300 m, aside from introducing a lag of several days (Fig. 2.7b, third row). The difference between the shelf and slope can be understood by considering the role of the various modes described in the previous section. Removal of local equatorward wind stress weakens equatorward flow associated with the first mode over both the shelf and slope. However, the suppression of locally-generated higher modes results in weaker equatorward flow over the shelf and weaker poleward flow over the slope. These two effects counteract each other over the slope, but reinforce each other over mid shelf, resulting in greater sensitivity to local wind stress over the mid shelf.

2.4.1.4 Southern boundary condition

The CTW model includes signals created at the southern boundary of the model in addition to those generated by wind forcing along the west coast. The southern boundary condition relies on the assumption that fluctuations in adjusted sea level at San Diego are associated

with first mode coastal trapped waves. In order to show the effect of this southern boundary condition on the model results, we use an alternative boundary condition of $\phi_1(0,t) = 0$, representing zero wave energy at the southern boundary.

Over mid shelf, the southern boundary condition (Fig. 2.7a, fourth row) does not have as much of an effect on the modeled velocity as the local wind stress (Fig. 2.7a, third row). However, the southern boundary does have a significant effect on the modeled velocity over the slope (Figs. 2.7b, fourth row). Without using San Diego sea level at the southern boundary, the 300-m velocity time series lacks the observed persistence of equatorward flow during spring and poleward flow during late summer and early fall. Poleward flow events still occur, and are much more frequent than over the shelf, but equatorward flow events are also common during late summer.

In the seasonal mean, the modeled undercurrent at the British Columbia (BC) segment is much weaker with no wave energy at the southern boundary ($\sim$0.02 m s^{-1}) and remains confined offshore of the 400 m isobath (Fig. 2.8). The wintertime poleward flow and spring-time equatorward flow over the upper slope are also significantly weaker. Further south at the Humboldt Bay segment (HB, 40.8°), the undercurrent modeled with $\phi_1(0,t) = 0$ is stronger than at the BC segment, but mean poleward velocity still does not exceed 0.05 m s^{-1} (Fig. 2.9). At this location, alongshore wind stress produces the strongest undercurrent during May-June, when modeled equatorward flow near the coast is also strongest. In contrast, observations from Lagrangian floats show that the CUC is strongest during September and October throughout the CCS (Collins et al., 2003). With San Diego sea level included, the CTW model does have its strongest CUC during September–October at this latitude ($v \simeq 0.10$ m s^{-1}, not shown). Therefore, although wind forcing along the U. S. west coast alone can produce a poleward undercurrent in the CTW model, the magnitude and timing of its seasonal cycle are greatly improved with the use of San Diego sea level at the southern boundary.

2.4.2 Large scale structure of the APF during summer

Knowing the structure of the APF over the slope is important for understanding the CUC because a poleward APF allows for acceleration of poleward flow in the presence of equatorward wind forcing. In this section, we use the the NCOM-CCS and CTW models to gain insight into the structure and variability of the APF. Seasonal differences in the APF during 2005 are first examined near the coast, where tide gauge observations are available in addition to the model results. Analysis of the modeled APF is then extended offshore to the continental slope, where the models can provide a more complete view of its timing and spatial structure.

2.4.2.1 Alongshore variability in coastal sea level

The three month period January–March, when mean winds are downwelling-favorable, is compared with with 15 June–15 September, a period when winds are upwelling favorable and observed flow over the upper slope accelerates over the course of the season from predominantly equatorward to poleward (Fig. 2.2b). Between these two periods, which will be referred to as "winter" and "summer" conditions, observed sea level drops to lower values along the entire coastline from Point Conception to Vancouver Island (Fig. 2.10a), consistent with the development of equatorward geostrophic coastal currents near the coast. The magnitudes of the observed seasonal decreases in sea level vary along this section of the coast, from ∼0.06 m at Port San Luis, CA (PSL) to ∼0.17 m at Newport, OR (NH) and Neah Bay, WA (NB). The observed seasonal decrease in sea level is generally larger in the northern portion of the domain.

Modeled seasonal differences in sea level follow overall patterns similar to those of the observations, showing larger seasonal decreases in the northern CCS (Fig. 2.10a). The NCOM-CCS model underestimates the overall magnitude of the sea level decrease at all latitudes, but relative differences along the coast parallel those in the observations. The CTW model shows a weaker alongshore gradient in the seasonal differences. To reproduce the magnitude of the observed sea level gradient in steady barotropic model, Hickey and Pola (1983) used a smaller frictional coefficient of $r = 1 \times 10^{-4}$ m s^{-1}. Using this value of

r in the CTW model results in a larger alongshore gradient in sea level (Fig. 2.10a), which is associated with stronger equatorward flow over the shelf and stronger poleward flow over the slope in the northern CCS (Fig. 2.7, top rows).

Absolute alongshore gradients in coastal sea level are provided by the numerical models. During January–March 2005, the NCOM-CCS and CTW models both show higher average sea level in the northern CCS, with an overall difference of ∼0.05 m or less between TF to the north and the lowest sea level near 40°N (Fig. 2.10b). During June–August, coastal sea level in the NCOM-CCS model slopes ∼0.10 m downward from PSL to NH. Further north from NH to TF, the sea surface slopes upward, indicating an equatorward APF at the coast from northern OR to southern BC. In the CTW model north of NH, coastal sea level slopes either very weakly upward or downward to the north, depending on which drag coefficient is used. Both models are able to produce a realistic undercurrent in the northern CCS during 2005 (Section 2.3) without coastal sea level sloping downward to the north.

Because the CUC shows significant variability at time periods of days to weeks in addition to the seasonal cycle, it is also important to examine intra-seasonal variability in the large scale APF. At the coast, the observed surface APF ($-g\eta_y$, where η is sea surface height) between Newport and Neah Bay during 2005 is more correlated with remote wind stress to the south than with local wind stress (Fig. 2.11a). The highest correlation between τ and $-g\eta_y$ occurs near Humboldt Bay, CA (HB), over 400 km south of Newport, and the sign of the correlation indicates that the APF is directed most poleward following wind relaxations or reversals at HB (Fig. 2.12). The lags between τ and $-g\eta_y$ suggest a propagation speed twice as fast the free wave phase speed c_1 (Fig. 2.11b), consistent with a forced wave response. At the coast between NH and NB in the NCOM-CCS model, the magnitude of fluctuations in $-g\eta_y$ are weaker than observed (regression coefficient = 0.56), but are strongly correlated with the observations (CC = 0.87), indicating that the NCOM-CCS model accurately represents variability of the APF over the shelf (Fig. 2.12a,b).

2.4.2.2 The APF at undercurrent depths

Analysis of the modeled APF is now extended from the coast, where it is most readily observed, to the slope, where the CUC is located. Using the NCOM-CCS model, the large scale APF ($-\rho_o^{-1}p_y$) is calculated at the 309-m model z level, a typical undercurrent depth. Pressure is calculated from the model output by integrating density downward from the sea surface:

$$p(x,y,z,t) = g\int_z^{\eta(x,y,t)} \rho(x,y,z^*,t)dz^*, \tag{2.19}$$

where ρ is in-situ density. Perturbation pressure is defined as

$$p'(x,y,z,t) = p(x,y,z,t) - \bar{p}(z), \tag{2.20}$$

where $\bar{p}(z)$ is reference pressure calculated from a mean density profile, which does not contribute to horizontal gradients. In order to evaluate the large scale APF over the same scale as the coastal sea level gradients, two end points from the same latitudes as NB and NH are selected.

Comparing the modeled surface APF at the coast with the bottom APF at 309 m over the northern CCS slope (Fig. 2.12b) reveals several major differences. Fluctuations have smaller magnitude near the bottom at 309 m over the slope, as would be anticipated from the structure of a first mode CTW in which the amplitude of pressure decreases with depth and distance offshore. Furthermore, there is no significant correlation between the surface APF at the coast and the bottom APF at 309 m over the slope. This lack of correlation is likely due to the presence of higher modes. The spatial and temporal variability of bottom pressure at 309 m during this period shows poleward-propagating signals with phase speeds that vary between events. An example during late May 2005 is highlighted in which a low pressure signal propagates northward with the phase speed of a forced first mode wave ($2\times c_1$), followed by a high pressure signal with the phase speed of a forced second mode wave ($2\times c_2$). During this event, a poleward pressure gradient develops over the slope during the transition from low pressure to high pressure, and is enhanced by the poleward decay of the high pressure signal (Fig. 2.12b,c). Similar patterns can be found, for example, in

the time periods leading up to the next poleward APF event during early June and the strongest poleward APF event during mid-July.

In addition to being uncorrelated, the modeled surface APF at the coast and the bottom APF over the slope have different directions during summer in the northern CCS. The surface APF at the coast (Fig. 2.12b) is directed equatorward, as seen previously in the seasonal mean (Fig. 2.10b). At 309 m over the slope, the APF is generally directed poleward (Fig. 2.12b). The June 15–September 15 means of perturbation pressure and SSH are used to examine the large-scale spatial structure of the APF with depth and latitude over the slope (Fig. 2.13). South of 42°N, the mean SSH over the slope during this period is consistent with a large-scale poleward APF at the surface (Fig. 2.13a). North of 42°N, higher SSH to to the north indicates an equatorward surface APF over the slope. These large-scale patterns are consistent at multiple isobaths over the slope. Smaller scale variability (<1° latitude) is also present in the northern CCS. Distributions of mean bottom pressure over the slope (Fig. 2.13b) reveal a large scale poleward APF at all latitudes, from Point Conception to Vancouver Island. The large scale APF at the bottom is weaker at isobaths deeper and further offshore. The distribution of perturbation pressure in the water column over the 309-m isobath (Fig. 2.13c) shows that depths >150 m are characterized by lower pressure to the north at all latitudes, indicative of a poleward APF throughout the CCS at depths below the shelf break.

The pressure distribution over the slope during 15 June–15 September indicates that the summer mean poleward APF at undercurrent depths in the northern CCS is associated with alongshore density gradients, not a sea surface that slopes downward to the north. Over the upper slope, the $\sigma_t = 26.5$ isopycnal peaks at 42°N (Fig. 2.13d). North of this latitude, the alongshore density gradients are responsible for the poleward APF at undercurrent depths. Further south, the alongshore density gradients weaken the stronger poleward APF at the surface. Like the NCOM-CCS model, the CTW model density peaks near 42°N (Fig. 2.13e). The CTW density anomalies represent upward displacement of isopycnals from the background stratification at each segment. Because of the segmented construction of the CTW model, variations in density anomaly do not directly translate to alongshore density gradients. While the magnitude of these anomalies appears to be about an order of

magnitude less than in the NCOM-CCS model, this pattern provides additional evidence that the structure of the mean summer density field over the slope is part of the response to alongshore wind stress in the CCS.

The cross-shelf structure of the APF is more easily examined in the CTW model than the NCOM-CCS model, since the bathymetry is uniform in the alongshore direction within each segment. Consistent with the above analysis, the structure of the APF is examined during the period 15 June–15 September 2005, a period when poleward flow develops over the upper slope in both the NCOM-CCS (Fig. 2.14a–c) and CTW (Fig. 2.14d–f) models. During this time period, the poleward APF in the CTW model is strongest near the bottom at the shelf break, and an equatorward APF is present over the shelf near the coast (Fig. 2.14g). The stronger poleward APF at depth over the slope again highlights the importance of alongshore density gradients at this latitude. The CTW model does not have an equatorward surface APF over the northern CCS slope, a characteristic of the NCOM-CCS summer mean (Fig. 2.13a). The surface APF over the slope may be associated the equatorward shelf break jet, which is completely absent from the CTW model. As with the NCOM-CCS model, the equatorward surface APF at the coast and the importance of density gradients over the slope are unique to the northern CCS during this time period. Analysis of the APF further south in the CTW model, at the Humboldt Bay segment at 40.8°N e.g., indicate that the poleward APF is strongest at the surface and near the coast (not shown).

The pressure fields of the NCOM-CCS and CTW models share two major features in the northern CCS during summer: 1) an equatorward surface APF near the coast, and 2) enhancement of the poleward APF at depth over the slope by alongshore density gradients. However, in addition to being associated with the development of a poleward CUC, the poleward APF also associated with onshore flow through the Coriolis force. The CTW model indicates that the APF during this time period is largely balanced by the Coriolis force, fu (Fig. 2.14h), which is much greater than the mean acceleration, v_t, during this long seasonal time period (Fig. 2.14i). In the following section, low-frequency (>20 d period) variability in the alongshore momentum balance in this balance over the slope will be analyzed in order to show how linear wind-forced CTWs contribute to this balance.

2.4.3 Alongshore momentum balance

In this section, variability in the APF is related to the acceleration of alongshore currents and the Coriolis force by analyzing the modeled alongshore momentum balance in the interior of the water column. In a linear model, the alongshore momentum balance away from the frictional boundary layers is described by

$$v_t + fu = -\rho_o^{-1} p_y, \tag{2.21}$$

where poleward acceleration and the Coriolis force associated with onshore flow are balanced by a positive APF. The magnitude and timing of these terms is examined in the CTW and NCOM-CCS hindcasts. First, the validity of a linear alongshore momentum balance is assessed. It is then shown that the Coriolis force leads the APF over the slope in a manner consistent with wind-forced CTWs. A CTW model with idealized forcing is used to explain this phase relationship.

2.4.3.1 Momentum balance in NCOM-CCS and CTW hindcasts

The validity of the linear momentum balance (2.21) throughout the water column over the slope can be examined using the nonlinear NCOM-CCS model. In order to focus on time scales of several weeks or longer, time series have been filtered with a 20-d Hanning window. The alongshore direction is defined as the orientation of the 309-m isobath. In order to remove mesoscale variability and focus on the alongshore scale of the northern CCS slope, NCOM-CCS time series have been averaged over 44.5°N–48.5°N and 3 grid points offshore of this isobath.

The depth variation of the alongshore flow shows the acceleration and shoaling of the undercurrent during summer (Fig. 2.15a). The APF and Coriolis force resemble each other closely in timing, magnitude and depth structure (Fig. 2.15b,c). Although there is a mean baroclinic depth structure (Fig. 2.13c), a surface-intensified poleward APF is present during July (Fig. 2.15b). Agreement between acceleration and the residual of the Coriolis force and APF away from the surface boundary layer indicates that the linear balance holds reasonably well over the slope, especially at 100–300 m (Fig. 2.15d,e).

The velocity time series at the $z = -181$ m level shows that the two models are consistent with each other in representing low-frequency (>20 d period) slope currents over the entire year 2005 (Fig. 2.16a). As seen previously in the model-observation comparisons (Fig. 2.2b), equatorward flow is present during June and poleward flow develops over the summer. An earlier period of spring equatorward flow occurs in both models during April (Fig. 2.16a).

The Coriolis force and APF are highly correlated in the NCOM-CCS model (Fig. 2.16b). As anticipated from the idealized case in the previous section, the Coriolis force leads the APF, with a lag of two days between the two terms. In the CTW model, the Coriolis force and APF are weaker and not as strongly correlated (Fig. 2.16c). However, the timing of the APF is similar in the two models, with maxima in the poleward APF during late April and mid-July. In both models, the poleward APF is persistent during the period June–August. With wind forcing only, and no San Diego sea level at the southern boundary ($\phi_1(0,t) = 0$), the Coriolis term and the APF are more strongly correlated (Fig. 2.16d) and the Coriolis term leads the APF as in the idealized case. Even without persistent poleward velocity over the slope in this wind-only case(Fig. 2.7b, fourth row), the poleward APF is still persistent throughout June–September (Fig. 2.16d). It therefore appears that the poleward APF, and the phase relationship of the Coriolis force leading the APF by several days, is associated with wind-forced CTW dynamics.

2.4.3.2 CTW model with idealized forcing

The momentum balance over the slope in the models discussed above suggests that the Coriolis force and APF are equally important in balancing acceleration over the slope, and that the Coriolis force associated with onshore flow leads the APF. An idealized scenario with simplified wind forcing is now used to explain why this phase relationship occurs. The wind forcing is spatially uniform over a limited region 35–45°N and periodic in time, with 20-d period and 0.1-N m^{-2} amplitude. To simplify the model setup, the bottom topography and other CTW parameters for the entire coastline are taken from the northernmost BC segment.

Over the mid-shelf north of the wind forcing region, the magnitude of the acceleration

term is approximately the same as the APF with a short lag (Fig. 2.17a,b). The Coriolis term is smaller and lags the other two terms by ∼90°. Over the shelf, including the second mode increases the amplitude of the fluctuations, but does not significantly alter the phase of any of the terms. In contrast, the momentum balance over the slope is fundamentally altered from the shelf balance when two modes are included (Fig. 2.17d). All terms have similar amplitudes, and the APF leads acceleration. The Coriolis force associated with onshore flow leads the positive APF.

The inclusion of the second mode alters the phase difference between alongshore currents over the shelf and slope (Fig. 2.17e,f). With one mode, the currents vary together over the entire shelf and slope. With two modes, slope currents lead shelf currents, and poleward flow develops over the slope while equatorward flow is still present over the shelf. Poleward flow over the slope develops as part of the response to equatorward wind stress in the forcing region. Equatorward wind stress (days 30–40, e.g.), generates first mode waves that lower sea level and produce equatorward currents over the shelf. The response propagates with phase speed slightly faster than $2\times c_1$ in the forcing region, and reaches a maximum at the northern boundary of the forcing region several days following the strongest wind stress (Fig. 2.17g). Note that without damping, the phase speed in the forced region is exactly equal to $2\times c_1$ (not shown). North of the forcing region, the waves decay and propagate with phase speed c_1. The second mode waves, in which low sea level at the coast is associated with equatorward flow over the shelf and poleward flow over the slope, travel at slower speeds but still propagate twice as fast in the forcing region (Fig. 2.17h). The transition to poleward flow over the slope at 48°N occurs on day 40 when the equatorward wind stress in the forcing region has ended, the second mode wave generated by the equatorward wind stress is strongest, and the first mode wave has already started to relax.

The idealized scenario above, with multiple CTW modes and forcing at 20-d periods, explains why the Coriolis force, fu, leads the APF over the slope in the NCOM-CCS model. These dynamics contribute to the poleward flow events that occur over the slope, but less frequently over the shelf, when the CTW model is run with wind forcing only (Fig. 2.7, bottom rows). However, this wind-forced model setup does not address the development of the seasonal undercurrent, which arises through the southern boundary condition in the

CTW hindcast. This topic and others will be discussed in the following section.

2.5 Summary and discussion

This study uses two numerical models with different levels of complexity to examine the dynamics of the poleward CUC. Time series observations of alongshore velocity over the continental slope allow for a detailed assessment of modeled variability over time scales of days to seasons. Major results are summarized below:

- In a linear CTW model, seasonal development of a persistent CUC during late summer in the northern CCS was dependent on the use of San Diego sea level as a southern boundary condition (Section 2.4.1).

- Without San Diego sea level at the southern boundary, alongshore winds off the U.S. west coast do create poleward flow over the northern CCS slope at event time scales (Section 2.4.1). This response requires 2–3 modes, and is characterized by onshore flow leading the poleward APF over the slope by several days (Section 2.4.3).

- In the northern CCS, the modeled APF is directed equatorward near the coast during summer, with alongshore density gradients producing a baroclinic poleward APF at depth over the slope (Section 2.4.2). Further south, the surface APF is directed poleward near the coast and over the slope.

An unanticipated result of this study is the dependence of a persistent late summer CUC on the use of San Diego sea level at the southern boundary. Low adjusted sea level at San Diego during spring is associated with strong equatorward flow, and high adjusted sea level is associated with a poleward flowing inshore countercurrent (Reid and Mantyla, 1976). This near-surface poleward flow is evident in the mean NCOM-CCS sea surface height field during summer (Fig. 2.1a). This feature has been associated with an equatorward weakening of wind stress curl from the Southern California Bight to the northern coast of Baja (Oey, 1999). Model results have also shown that remote forcing from the equatorial Pacific contributes to the annual cycle of sea level in the CCS (Pares-Sierra and O'Brien,

1989). The importance of the southern boundary in the CTW model implies a dynamic link between poleward flows often considered to be separate: the undercurrent as far north as British Columbia and the inshore countercurrent in the southern CCS.

It is also possible that the persistent CUC during late summer arises from dynamics that occur along the U.S. west coast but are not included in the CTW model, such as wind stress curl north of Point Conception. Positive wind stress curl associated with wind stress decreasing towards the coast drives poleward Sverdrup transport. McCreary and Chao (1985) and Batteen (1997) have found that wind stress curl creates a stronger and shallower poleward undercurrent. This mechanism is distinct from the mechanism proposed by (Oey, 1999) for the inshore countercurrent, since it requires a β plane. Wind stress curl is relatively weak in the northern CCS, and is strongest off northern California and in the Southern California Bight (Bakun and Nelson, 1991). Future modeling studies may be able to determine at which locations wind stress curl is most important for driving poleward flow in the northern CCS.

Another factor missing from the CTW model is the β-effect. With varying wind stress, offshore propagation of low modes strengthens the undercurrent and contributes to the shoaling of the undercurrent at seasonal time scales (Philander and Yoon, 1982). Hurlburt and Thompson (1973) were able to model an undercurrent on a β-plane even with with no spatial variability in wind stress. Glider observations in the southern CCS have shown offshore propagation of poleward flow structures consistent with baroclinic Rossby waves (Todd et al., 2011). However, it is unclear how important the β-effect is on seasonal and shorter time scales further north off Washington and British Columbia. At the annual time scale, Rossby wave propagation only occurs south of a critical latitude, estimated to be $\sim$42°N in the CCS (Clarke and Shi, 1991). However, uncertainty in the critical latitude and the possibility of a broader band of frequencies in the average seasonal cycle make this another potential topic for future study.

While the seasonal development of the CUC cannot fully be explained by alongshore wind stress, the model results in this study show that the undercurrent can develop in the northern CCS even when the surface APF at the coast is directed equatorward (Figs. 2.10b, 2.14g). A poleward APF develops at depth over the slope during summer, and its presence

does not depend on the southern boundary condition of the CTW model (Fig. 2.16b-d). Although the observational study of Hickey and Pola (1983) showed a poleward surface APF at the coast during summer, the gradient was relatively weak (∼0.02 m difference between Newport, OR and Neah Bay, WA). The Csanady (1978) model used by Hickey and Pola (1983) does show an equatorward APF at the very northern end of the domain, similar to the model results presented here. It should be noted that the present study focuses on only one year, and therefore does not represent the long-term mean.

The alongshore structure of the APF is consistent with the steady model of McCreary (1981), in which the sea surface reaches a minimum at a latitude north of the maximum equatorward wind stress and south of the overall northward extent of the wind field. Further south over the CA slope in the NCOM-CCS model, the APF is poleward through the entire water column and alongshore density gradients weaken the poleward APF with depth, consistent with previous studies which focused on this region (Mellor, 1986; Pringle and Dever, 2009). In the McCreary (1981) model, the undercurrent deepens at higher latitudes and reaches a maximum amplitude at the latitude where isopycnals peak, similar to the NCOM-CCS structure (Fig. 2.13d). This structure of the APF remains even when the inclusion of a continental shelf weakens the undercurrent (McCreary and Chao, 1985). The same basic structure is shown in the two layer model of Yoshida (1967), in which sea level reaches a minimum at the northern edge of the wind stress forcing and the thermocline peaks at the same latitude. Shipboard observations suggest a peak in isopycnals over the slope that is offset to the north of the strongest upwelling-favorable winds (Muraki, 1974). Observational insight into the seasonal variability of alongshore density gradients in the northern CCS could arise from further analysis of historical hydrographic data.

In the NCOM-CCS model, the largest vertical displacement of isopycnals over the slope occurs at 42°N, north of the strongest mean wind forcing (Fig 2.13). In theory, higher CTW modes are characterized by a stronger baroclinic response over the slope, but these waves are damped more quickly and their strongest response does not penetrate far past the strongest forcing. At the coast, where the first mode response dominates, the reversal in the sea level gradient occurs further north at ∼45°N. This results in the pattern in which the surface APF at the coast can be weak or equatorward in the northern CCS, with a

poleward APF at undercurrent depths due to the presence of alongshore density gradients.

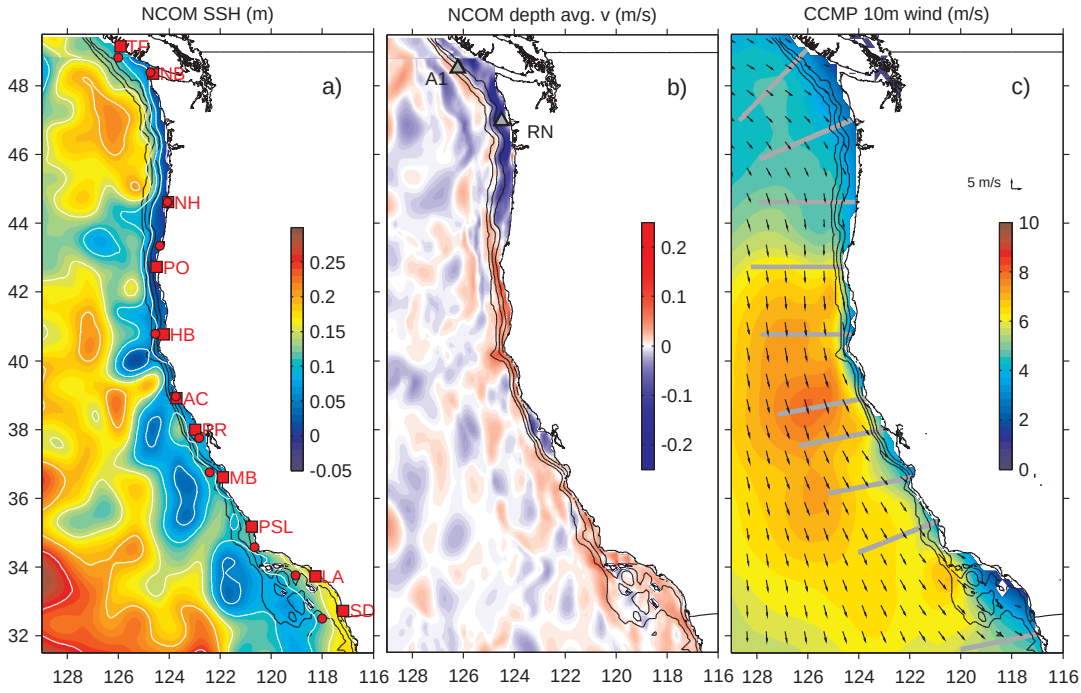

Figure 2.1: Mean model fields (NCOM-CCS, with global NCOM north of 49°N) and atmospheric forcing (CCMP) for the California Current, 15 June – 15 September 2005. The 200-, 500- and 1000-m isobaths are shown as black contours. a) Sea surface height, with 0.05-m contour intervals in white. Red squares indicate tide gauges and red circles show nearby measurements of sea level pressure. b) Northward component of depth averaged velocity. Gray triangles indicate mooring locations. c) Wind speed and velocity vectors. Gray lines indicate cross-shelf segments used in the coastal trapped wave model.

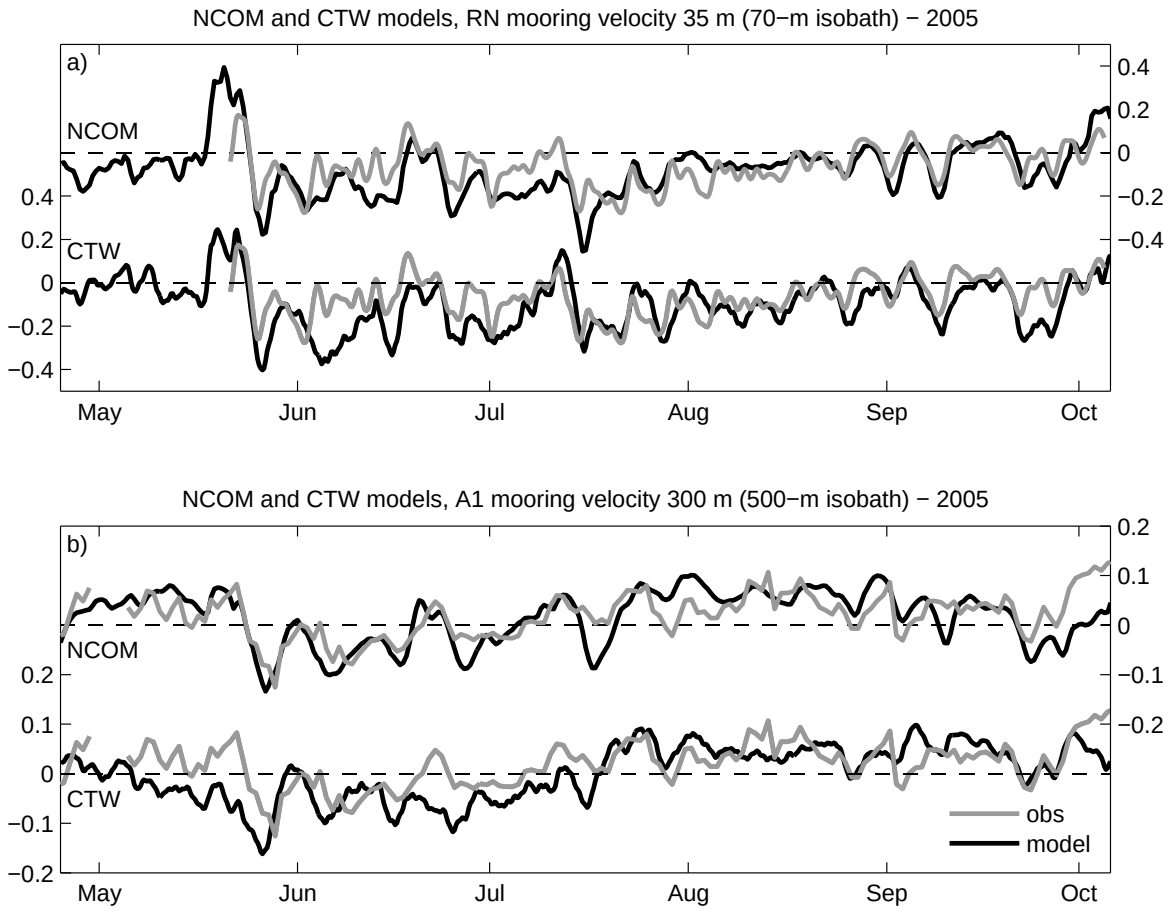

Figure 2.2: Comparison of CTW and NCOM-CCS modeled alongshelf velocity with current meter measurements. a) 35-m depth at the Washington shelf RN mooring site over the 70-m isobath. b) 300-m depth at the BC slope A1 mooring site over the 500-m isobath.

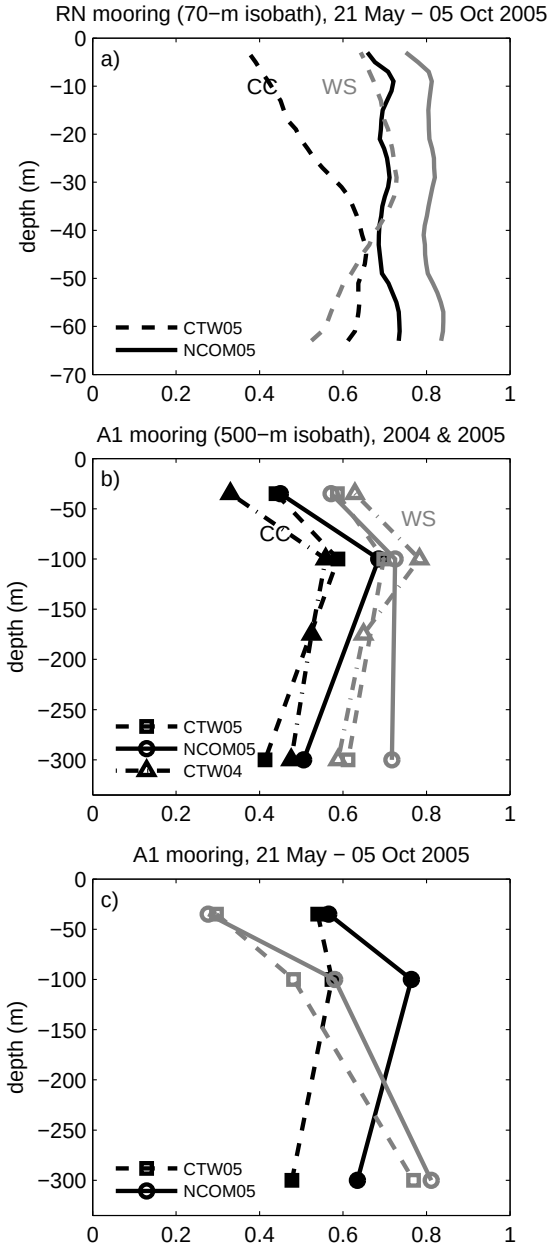

Figure 2.3: Profiles of model validation statistics for a) the RN mooring over the 70-m isobath, b) the A1 mooring over the 500-m isobath for 2004 and 2005, and c) the A1 mooring, but restricted to 21 May–5 Oct 2005 (the deployment period of the RN mooring). Black lines are correlation coefficients (CC); gray lines are Willmott skill scores (WS).

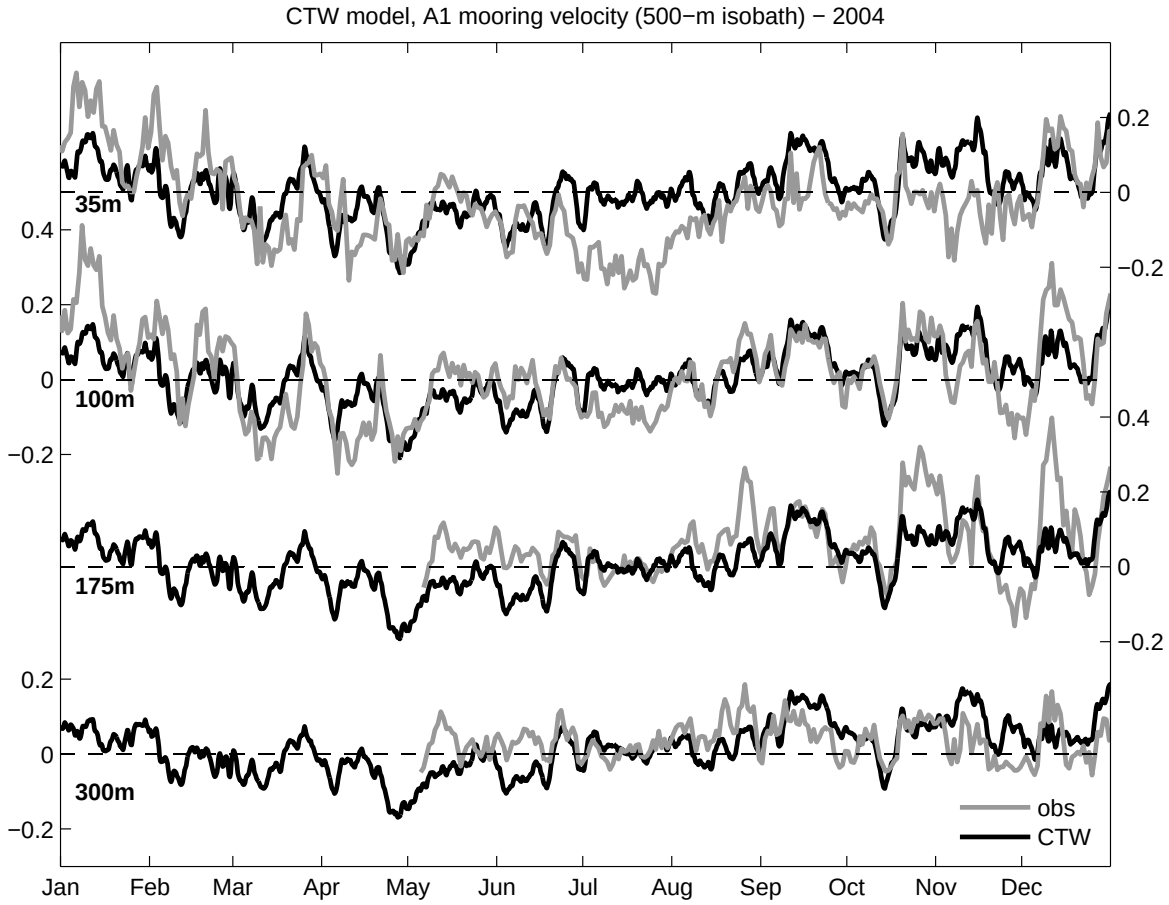

Figure 2.4: Comparison of CTW modeled alongshelf velocity with current meter measurements at the A1 mooring site during 2004. Model time series are extracted from the 500-m isobath at the nominal current meter depths 35 m, 100 m, 175 m and 300 m.

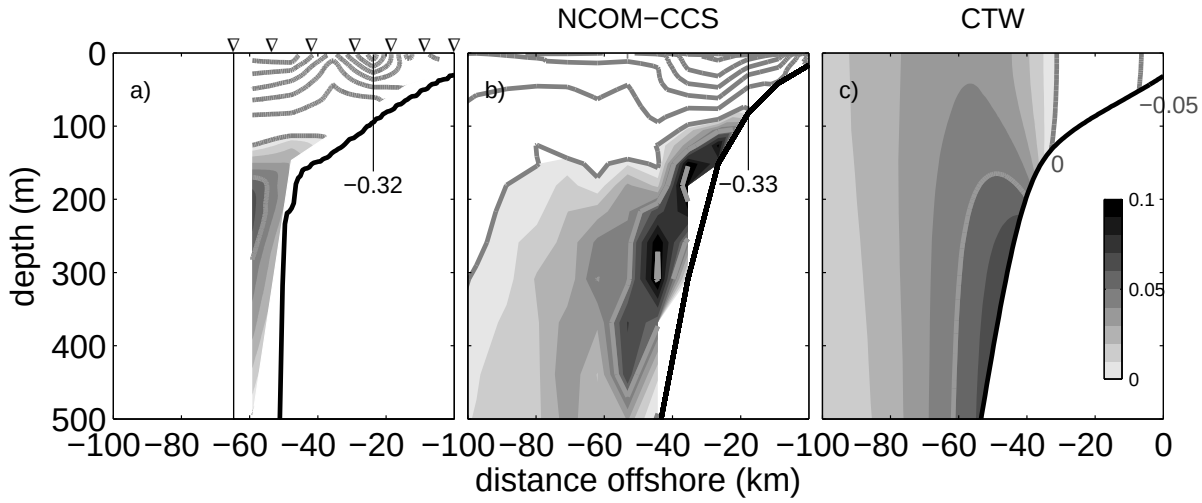

Figure 2.5: Sections of alongshelf velocity off the Washington shelf on 15 September 2005. Contour intervals are 0.05 m s^{-1}, and poleward flow is shown in shades of gray with 0.01 m s^{-1} intervals. Labels indicate the location and magnitude of the strongest equatorward velocity. a) Observed geostrophic velocity referenced to 500 dbar. Triangles indicate locations of CTD casts. b) NCOM-CCS model. c) CTW model.

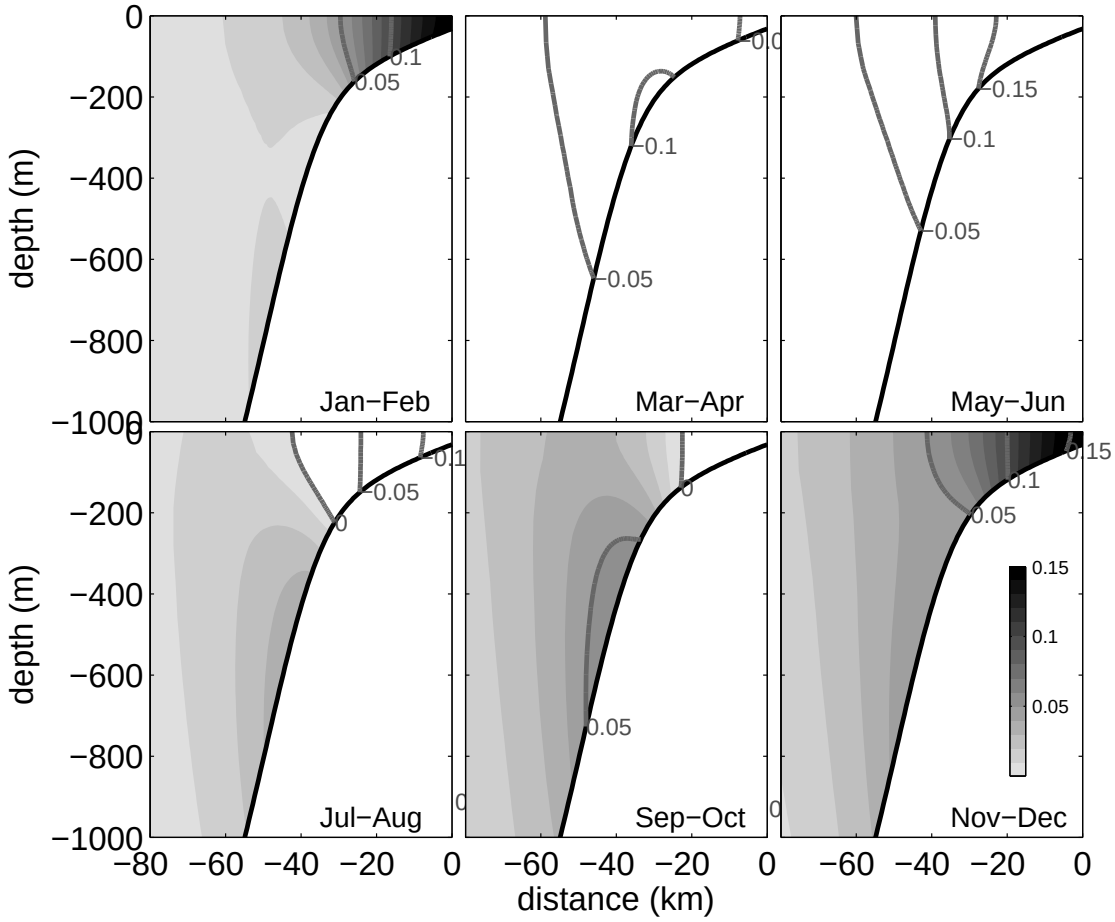

Figure 2.6: Seasonal cycle of alongshore velocity at the northern (British Columbia) segment of the CTW model, from two-month means over the period 1989-2008. Contour intervals are 0.05 m s^{-1}, and poleward flow is shown in shades of gray with 0.01 m s^{-1} intervals.

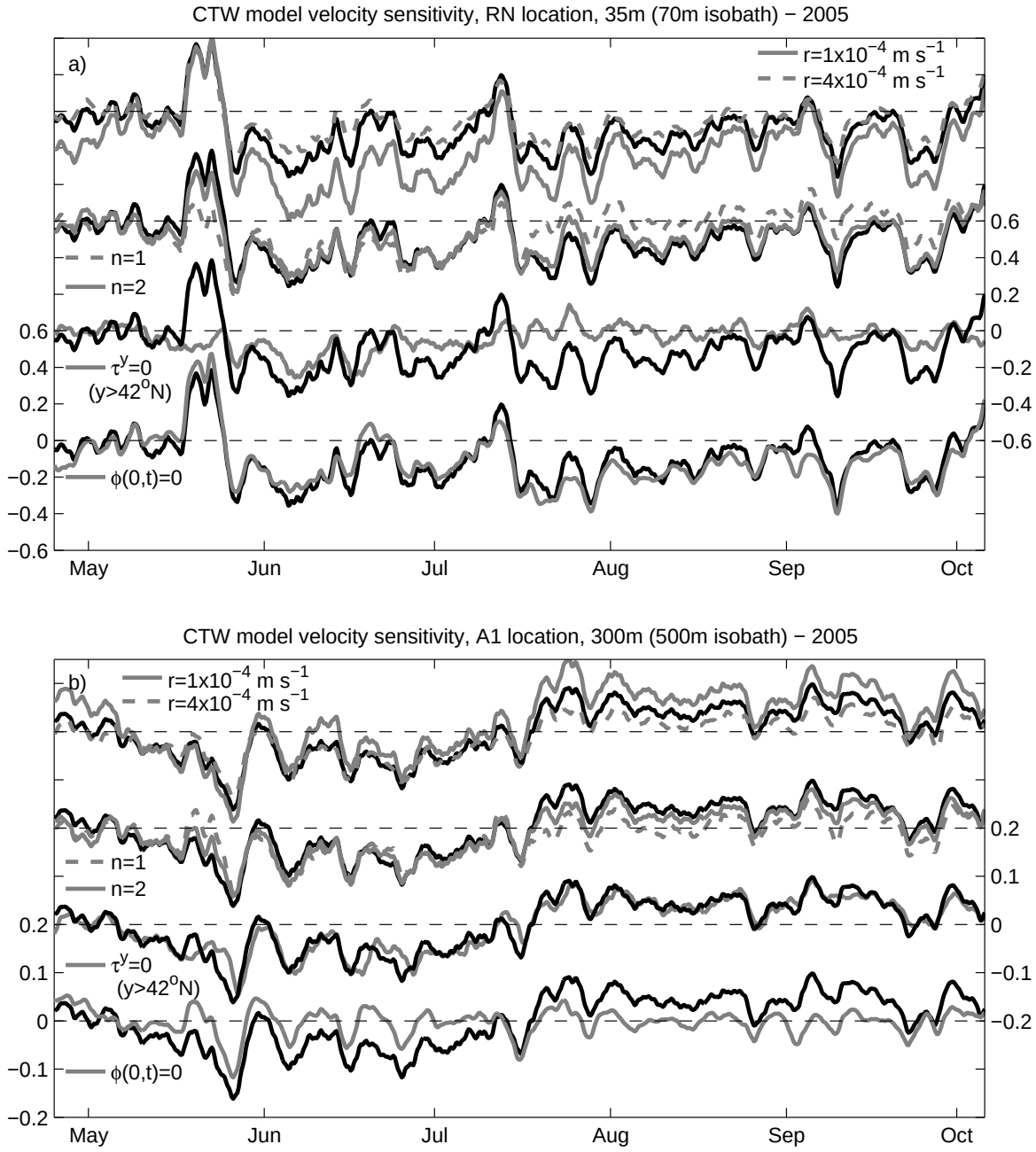

Figure 2.7: Time series of alongshore velocity showing sensitivity to parameters used in the CTW model a) At 35 m over the 70-m isobath at the RN site over the Washington shelf, and b) At 300 m over the 500-m isobath at the A1 site over the British Columbia slope. In each row, the solid black time series is the base run. First row: frictional coefficients $r = 1 \times 10^{-4}$ m s^{-1} (solid gray) and $r = 4 \times 10^{-4}$ m s^{-1} (dashed gray). Second row: calculations with 1 mode (dashed gray) and 2 modes (solid gray). Third row: no energy at the southern boundary (solid gray). Fourth row: no wind forcing north of 42°N (solid gray).

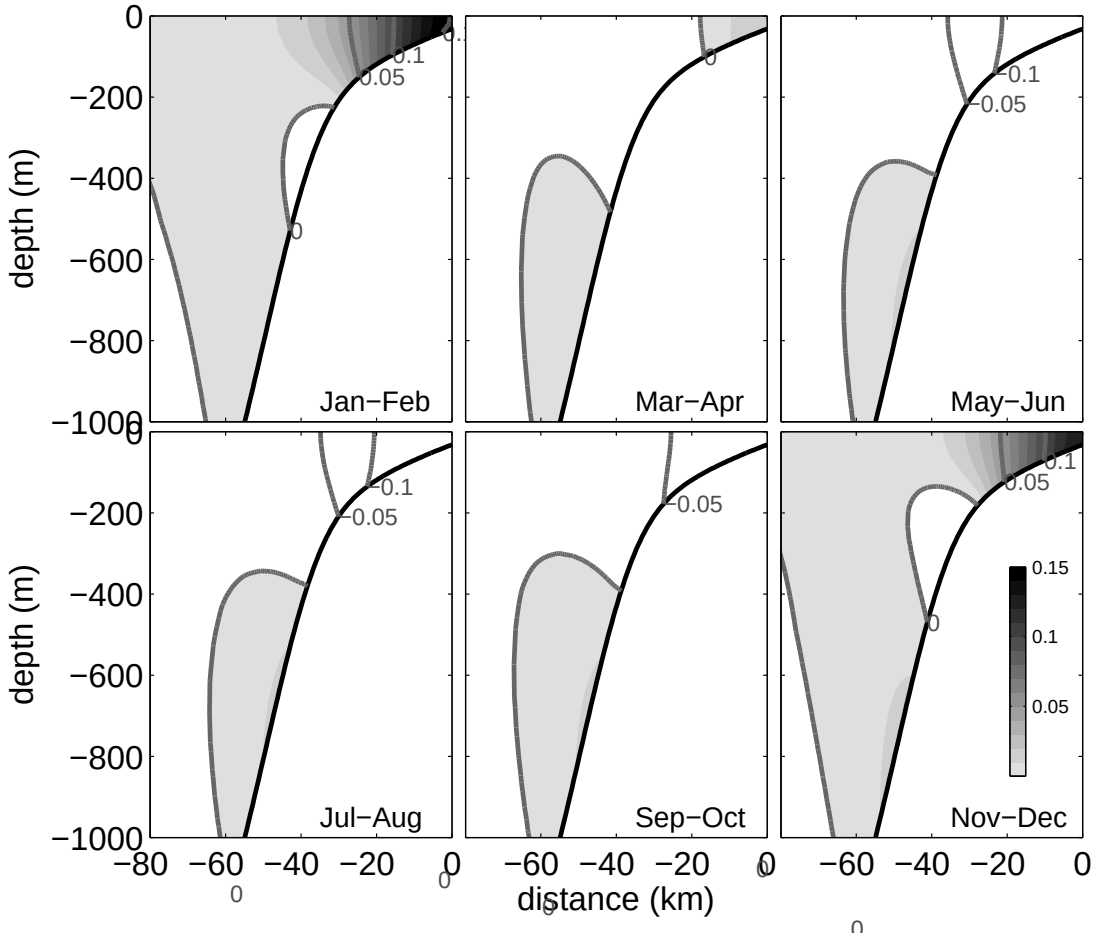

Figure 2.8: As in Fig. 2.6, but with no wave energy at the southern boundary.

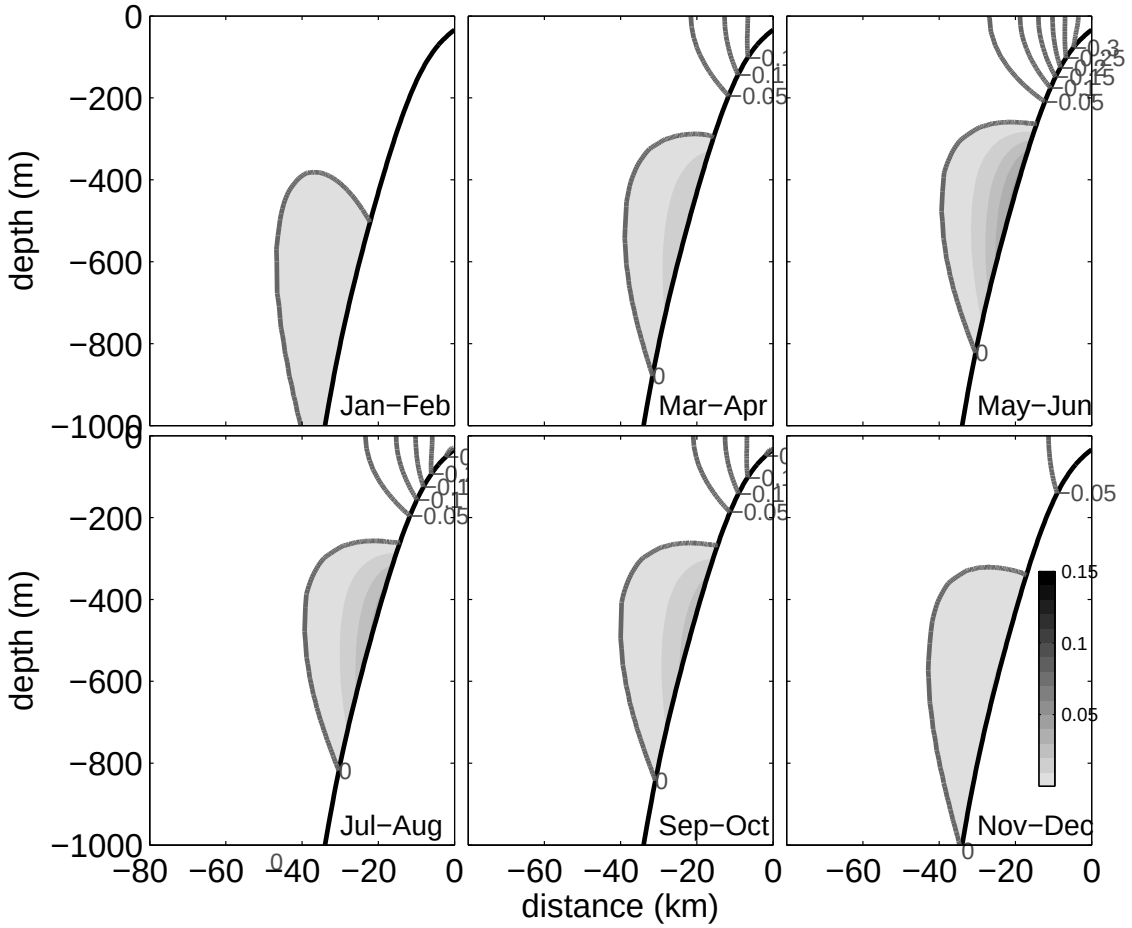

Figure 2.9: As in Fig. 2.6, but with no wave energy at the southern boundary and evaluated at the Humboldt Bay (HB) segment (40.8°N).

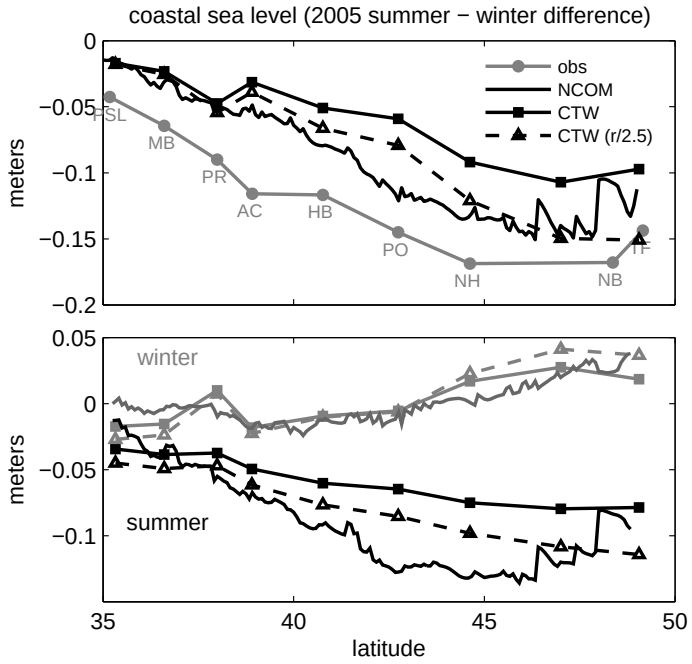

Figure 2.10: Seasonal differences in coastal sea level from Point Conception to Vancouver Island during 2005. a) Difference of seasonal averages from adjusted tide gauge observations (gray) and NCOM-CCS (black line), CTW (squares) and CTW with the drag coefficient reduced by a factor of 1/4 (triangles). Winter is defined as January–March; summer is defined as 15 June – 15 September. b) Summer and winter averages of sea level for the three models, referenced to the latitude-averaged mean winter value.

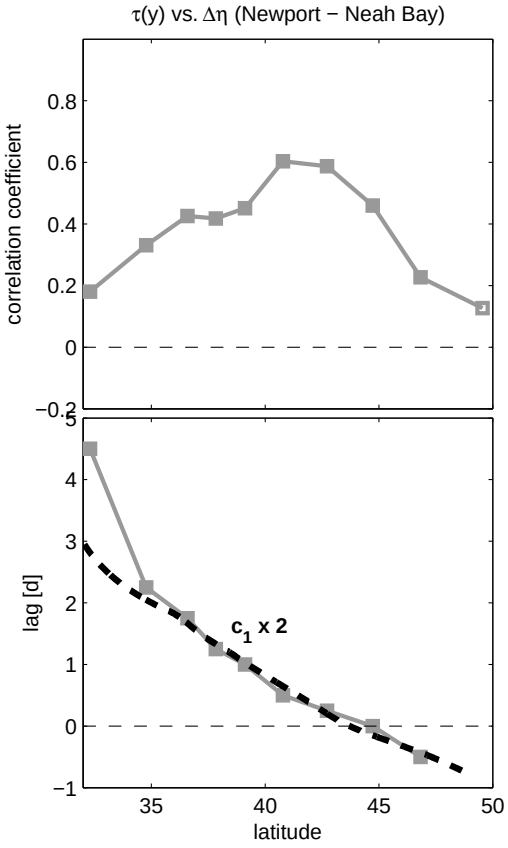

Figure 2.11: a) Correlation coefficient between observed sea level difference (NH-NB) and CCMP wind stress used in the CTW model at various latitudes. Filled squares indicate significance at the 95% confidence level. b) Lag, in days, of maximum lagged correlation.

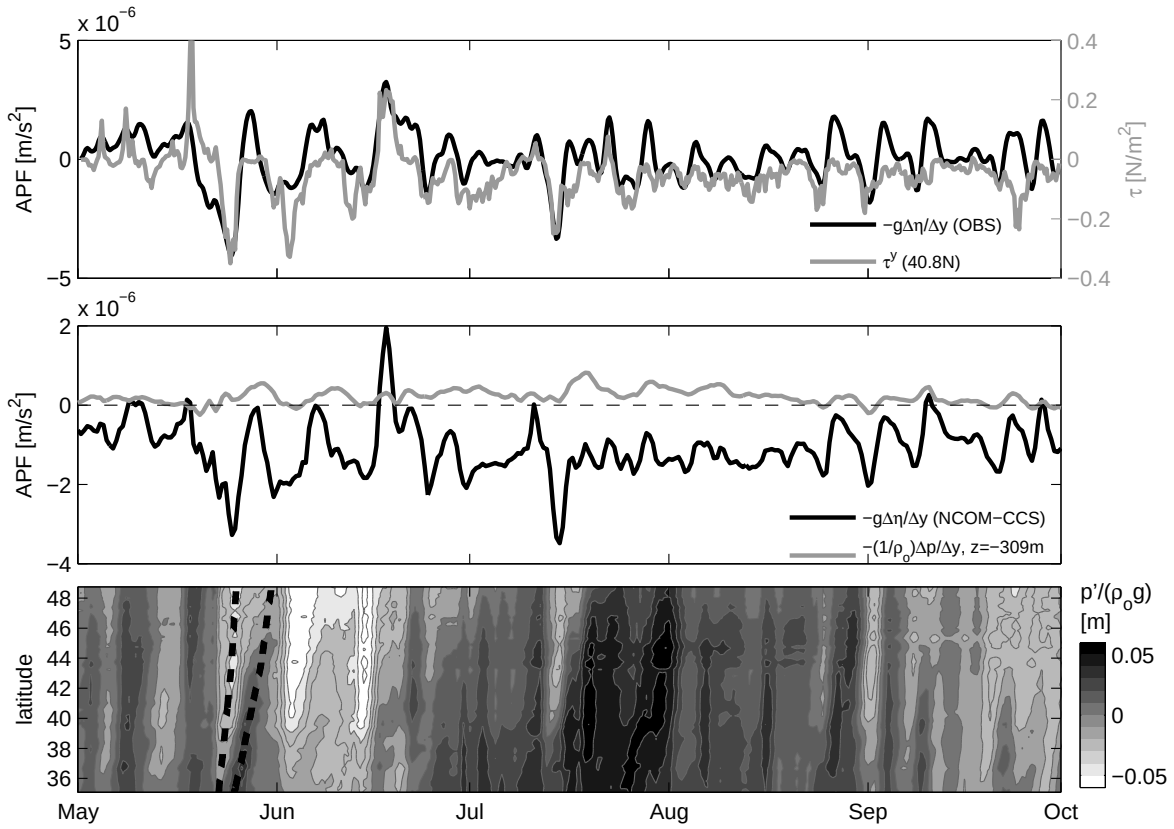

Figure 2.12: Time series from May-September 2005. a) Observed NH-NB sea level gradient (black) and CCMP wind stress near Humboldt Bay, CA at 40.8°N (gray). Sea level gradient is lagged by 0.5 d. b) Sea level gradient calculated from the same coastal locations in NCOM-CCS (black) and bottom pressure gradient at 300 m calculated from points at the same latitudes (gray). c) Bottom perturbation pressure at $z = -309$ m, from Point Conception to Vancouver Island. Dashed lines indicate forced wave characteristics for first and second mode CTWs.

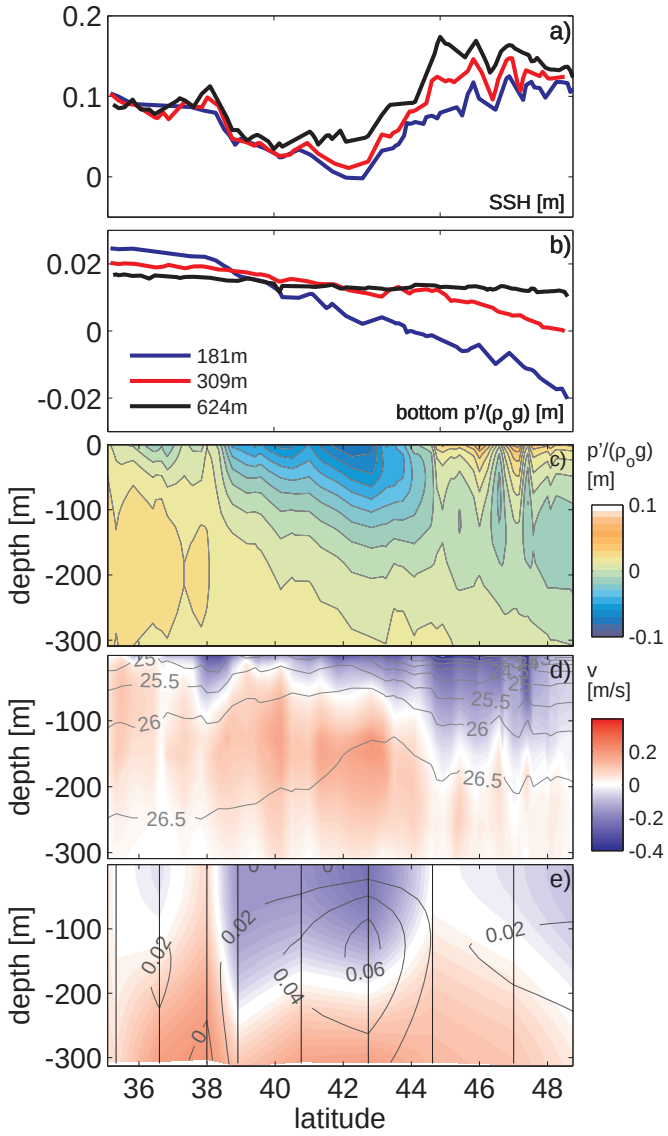

Figure 2.13: Mean alongshore structure over the slope during 15 June – 15 September over the 309-m isobath. a) NCOM-CCS SSH over three isobaths, b) NCOM-CCS bottom perturbation pressure over three isobaths, normalized to units of dynamic height, c) NCOM-CCS perturbation pressure, d) NCOM-CCS alongshore v (colors) and σ_t (contours), e) CTW velocity v and density anomaly (contours).

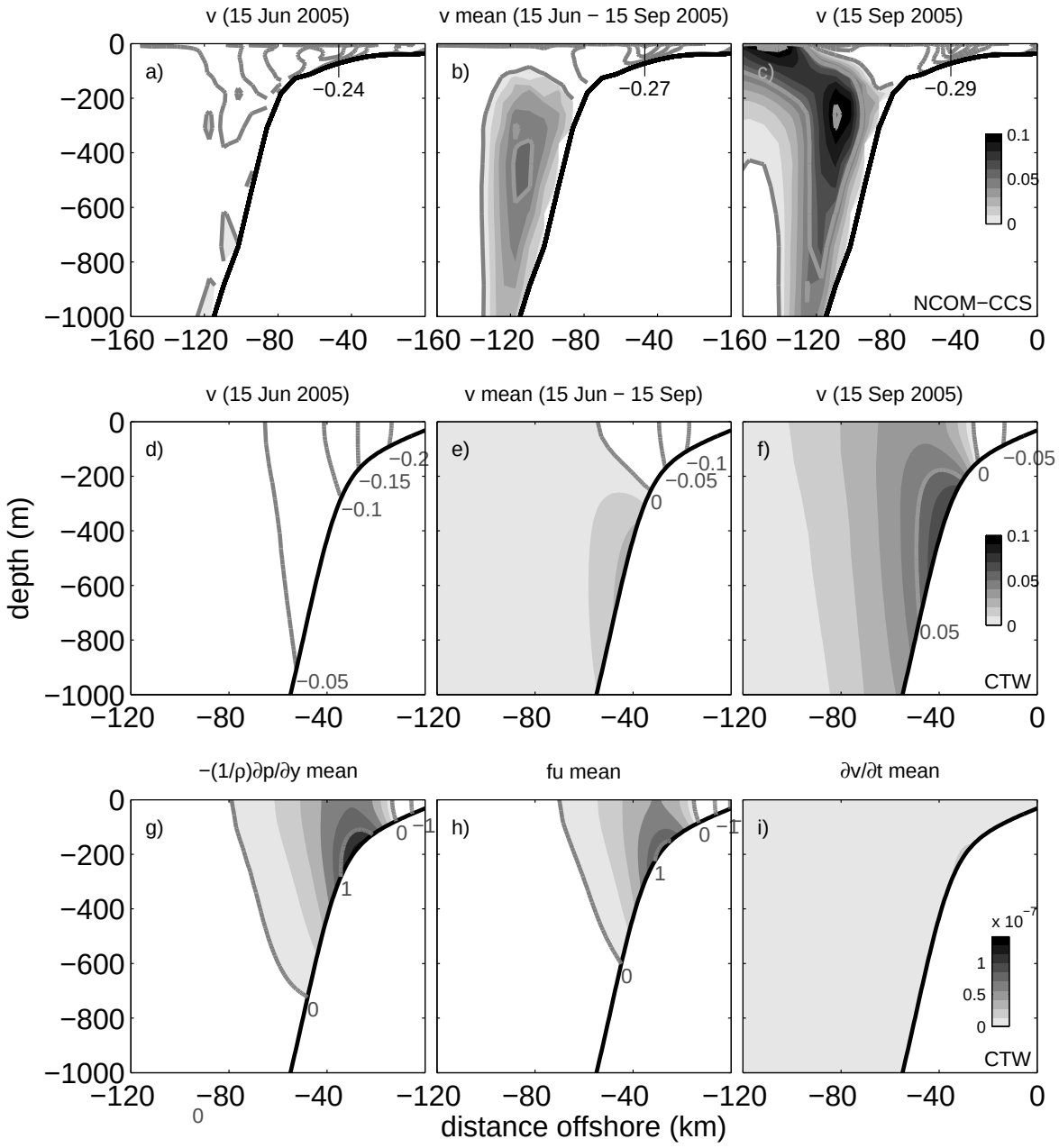

Figure 2.14: Seasonally-averaged model velocity and momentum balance terms for the British Columbia shelf. a) NCOM-CCS v, 05 June 2005. Velocity contour intervals are 0.05 m s^{-1}, with poleward velocity shaded at 0.01 m s^{-1} intervals. b) NCOM-CCS mean v, 15 June–15 September 2005. c) NCOM-CCS v, 15 September 2005. d) CTW v, 05-June-2005. e) Mean CTW v during, 05 June–15 September 2005. f) CTW v, 15 September 2005. g) CTW mean APF. h) CTW mean Coriolis force. i) CTW mean acceleration.

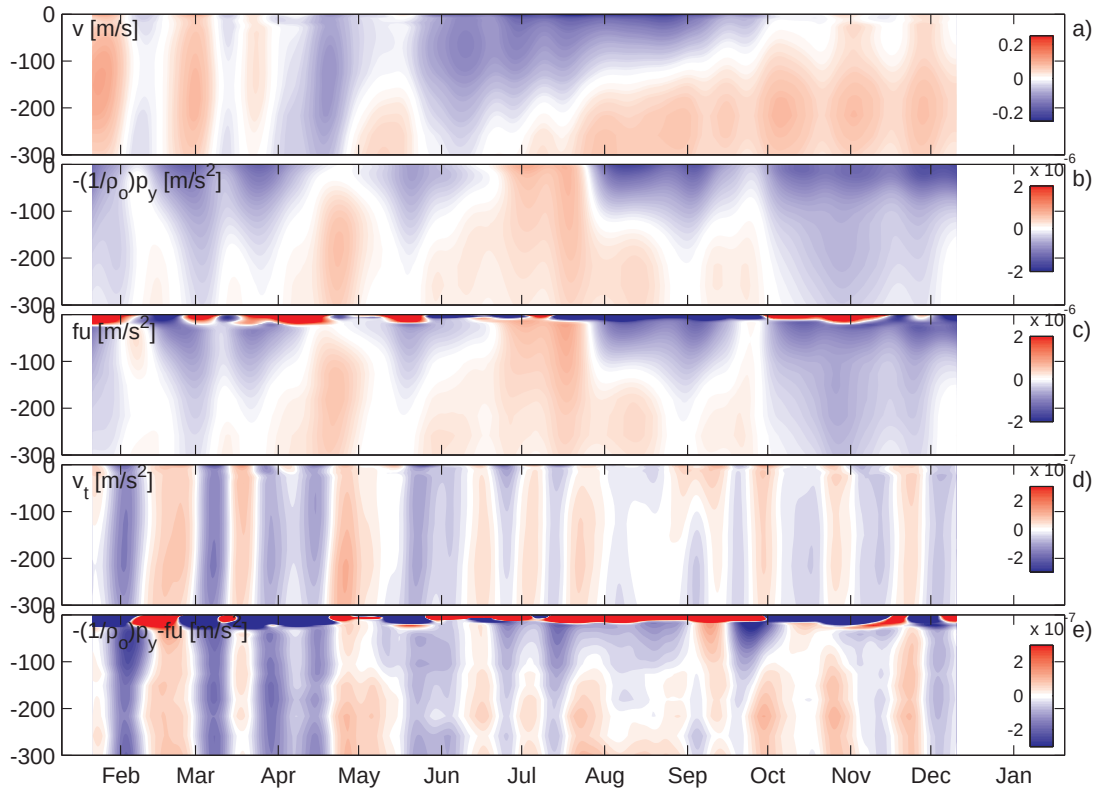

Figure 2.15: Velocity and linear momentum balance terms (20-d period and greater) over the northern CCS slope during 2005 from the NCOM model. a) Alongshore velocity. b) APF. c) Coriolis force. d) Alongshore acceleration. e) Residual of the APF and Coriolis force.

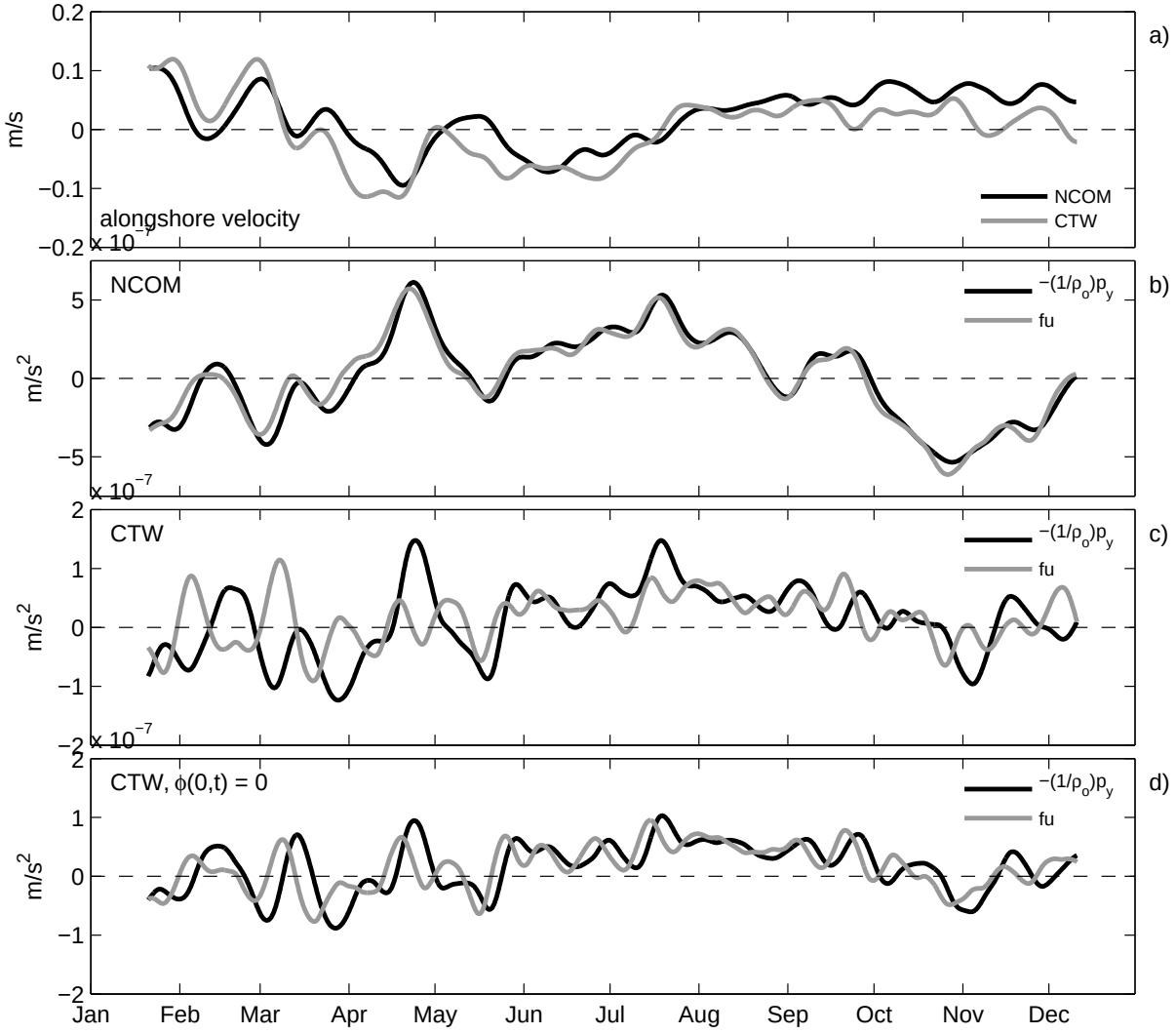

Figure 2.16: Modeled velocity and linear momentum balance terms (20d period and greater) at 181 m depth over the northern CCS slope during 2005. a) Alongshore velocity from the NCOM and CTW models. b) Alongshore PGF and Coriolis force from the NCOM model. c) Alongshore PGF and Coriolis force from the CTW model (note difference in scale from panel b). d) As in panel c, but for the CTW model run with no wave energy at the southern boundary.

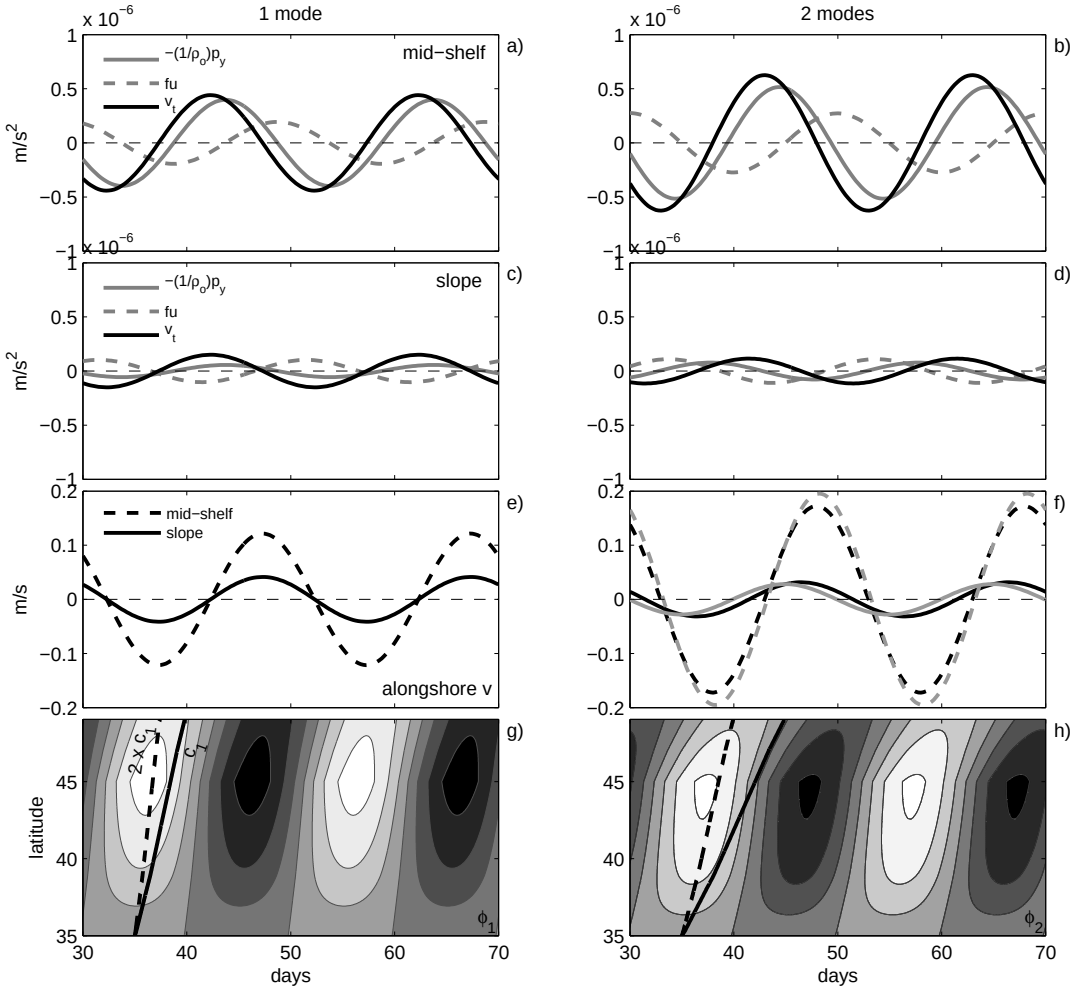

Figure 2.17: Time series from the idealized CTW model, with 20-d periodic wind forcing limited to the region 35-45°N. Wind stress is equatorward during days 30–40 and 50–60. The left column shows results using only one mode; the right column shows results with two modes. a-b) Momentum balance at mid-shelf (35-m depth over the 70-m isobath) at 48°N. c-d) Momentum balance over the slope (300-m depth over the 500-m isobath) at 48N. e-f) Alongshore velocity over the mid-shelf and slope (results with three modes shown in gray). g-h) Magnitude of $\phi_n(y,t)$ for n = 1 and n = 2, respectively. Lighter colors correspond to lower ϕ, lower sea level at the coast and stronger equatorward flow over the shelf. Dashed lines indicate forced wave characteristics (phase speed $2 \times c_n$) and solid lines indicate free wave characteristics (phase speed c_n).

Chapter 3

REGIONAL IMPACT OF SUBMARINE CANYONS DURING SEASONAL UPWELLING

Abstract

Along the coasts of Washington and British Columbia, in the northern California Current system, transport of water from the slope to the continental shelf contributes to high nutrient concentrations during the summer upwelling season. The goal of this study is to identify physical processes which govern the properties and source depth of shelf water. A numerical model hindcast for the region is shown to represent the seasonal development of equatorward flow over the shelf and the poleward California Undercurrent over the slope. Modeled circulation in shelf-break canyons is consistent with previous observational studies, showing correlation between equatorward flow over the outer shelf and dense water at the canyon head, as well as the formation of closed cyclonic eddies. Ageostrophic forces associated with unbalanced pressure gradients are generally directed onshore at the upstream sides of canyons, particularly during upwelling events. At the heads of canyons, however, the presence of dense water is often associated with ageostrophic forces that are directed offshore. Lagrangian particles indicate that canyons are associated with upwelling from depths of ∼150-250 m to the mid shelf. Upwelling from these source depths does not occur at locations away from canyons, or a model run with bathymetry that is uniform in the alongshelf direction. Onshore fluxes of deep salty water through submarine canyons are large enough to influence changes in salinity over the shelf at seasonal time scales. Much of the water upwelled through canyons is found in the bottom boundary layer over the shelf.

3.1 Introduction

The northern California Current system (CCS) is a region where numerous submarine canyons intersect the shelf break (Fig. 3.1a). Upwelling-favorable wind stress during sum-

mer months is relatively weak in this part of the CCS compared with locations further south, but the presence of submarine canyons may contribute to enhanced upwelling in the subsurface water column. Southward flow over the outer continental shelf, typical during summer months in the northern CCS, is associated with large vertical excursions of dense water and flow towards shore near the heads of canyons (Hickey, 1997; Allen et al., 2001). Hickey and Banas (2008) estimate that the flux of nitrate across the shelf break through submarine canyons is comparable to the nitrate input into the euphotic zone by local wind driven coastal upwelling, suggesting that submarine canyons greatly influence regional productivity. Dense water originating from the slope is also low in dissolved oxygen, contributing to seasonal hypoxia over the Washington shelf (Chapter 1, Connolly et al., 2010).

Upwelling events in submarine canyons along the shelf break occur when the overlying flow travels opposite to the direction of coastal trapped wave propagation, which corresponds to equatorward flow in the CCS. Observations indicate that the peak of a southward flow event corresponds with the coldest temperatures above the canyon and the strongest up-canyon flow (Hickey, 1997; Allen et al., 2001). Equatorward flow crosses isobaths at the upstream side of the canyon, and cyclonic vorticity is generated within the canyon as fluid columns become unconstrained by the shelf bottom topography and stretch (Allen, 1996; Hickey, 1997). Weakening of the equatorward flow within the canyon as it is turned onshore is associated with an unbalanced pressure gradient force towards shore (Klinck, 1996; She and Klinck, 2000). Particularly strong cyclonic vorticity is often associated with a closed eddy near the depth of the canyon rim. Observations of the rim-depth eddy show that it is strongest several days following peak upwelling, as isopycnals relax (Hickey, 1997). Surface flow $\sim$100 m above the canyon is unaffected by the canyon bathymetry. Model results show that anti-cyclonic vorticity (but not a closed eddy) is generated on the downstream side of the canyon as water is upwelled onto the shelf and fluid columns are compressed by the bottom (Allen, 1996; Klinck, 1996).

The modification of shelf flow near a shelf break canyon depends on geometry of the canyon and regional environmental conditions. Results from both numerical and laboratory models indicate that the response is sensitive to the direction of the flow, with greater net exchange occurring during upwelling than downwelling (Klinck, 1996; Boyer et al., 2000).

Stratification limits canyon upwelling (Klinck, 1996). Scaling analysis indicates that the upwelling flux through the canyon increases with incident flow velocity, as well as the length of the canyon and its width at the shelf break (Mirshak and Allen, 2005; Allen and Hickey, 2010). A sharp corner (small radius of curvature) at the upstream side of the canyon also increases the upwelling flux. The presence of a rim-depth eddy is largely determined by canyon geometry, and is more likely to occur for a box-shaped canyon than a triangular one (Allen and Hickey, 2010).

Compared with shelf break canyons, few studies have focused on long canyons, such as Juan de Fuca canyon (Fig. 3.1a), which extend all the way to the coastline. Theoretical and laboratory studies suggest that long canyons with strongly converging isobaths may be locations of steady upwelling even with weak equatorward velocity over the shelf (Allen, 2000; Waterhouse et al., 2009). Coastal trapped wave propagation is interrupted by the canyon, and upwelling through the canyon compensates for diminished equatorward flow to the north of the canyon. During strong incident flow, upwelling in long canyons resembles the advection-driven upwelling of shelf break canyons (Waterhouse et al., 2009).

Most studies have focused on a single canyon, and only recently have model studies addressed the impact of numerous canyons on a regional scale. In the northwest Mediterranean, under downwelling conditions, Jordi et al. (2006) showed enhanced cross-shelf transport near submarine canyons and calculated a flushing time for the shelf on the order of three months. On the southern coast of Australia, Kämpf (2010) showed that upwelling in shelf-break canyons contributes to the formation of a pool of dense, nutrient-rich water over the shelf, which can subsequently be upwelled to the euphotic zone. Lagrangian particles showed upwelling from 110–160 m below the depth of the shelf break, and nitrate fluxes were estimated to be enhanced by a factor of 5 over a case with no canyons.

Regional circulation in the northern CCS is characterized by upwelling favorable winds and equatorward flow during spring and summer months. The seasonal cycle of upwelling-favorable wind stress peaks during summer, though downwelling and relaxation events still occur throughout this season (Hickey, 1979, 1998). During summer, much of the event-scale variability is driven by coastal trapped waves generated further south (Battisti and Hickey, 1984). Equatorward flow is present over the slope during April–October, and the

poleward California Undercurrent (CUC) develops below shelf break depth over slope during late summer to early fall (Thomson and Krassovski, 2010). The cyclonic Juan de Fuca eddy, located offshore of Cape Flattery (Fig. 3.1b), appears as a persistent region of dense water with 50 km horizontal scale (Freeland and Denman, 1982; MacFadyen et al., 2008). Estuarine flow from the Strait of Juan de Fuca, tidal rectification and mixing just west of Cape Flattery, and variable winds typical of the upwelling season are important factors in generating the Juan de Fuca eddy (Foreman et al., 2008; MacFadyen and Hickey, 2010).

In this study, a hindcast of summer 2005 in the northern CCS is used to demonstrate the effects of canyon upwelling on shelf-slope exchange in the northern CCS. The model is validated on a regional scale with data from moorings and hydrographic surveys. In particular, it is shown the the seasonal development of the equatorward jet, poleward California Undercurrent and upwelled bottom water are well-represented by the model. Within shelf break canyons, the patterns and timing of modeled upwelling and vorticity are shown to be consistent with previous observational studies in the region. Two methods are used to quantify exchange between the slope and shelf over the course of the upwelling season. Lagrangian particles are tracked from the slope to mid shelf, and their source depths compared for model runs with varying bathymetry and coastline. In addition, salt budgets are calculated for volumes over the continental shelves of Washington and British Columbia, allowing fluxes across the shelf break to be quantified and directly compared with the seasonal increase in salinity over the shelf.

3.2 Methods

3.2.1 Model setup

The numerical model used in this study is an application of the Regional Ocean Modeling System (ROMS) (Shchepetkin and McWilliams, 2005), version 3.4. The domain spans the area 45.5–50°N, 128.5–123.8°W (Fig. 3.1a). Horizontal and vertical resolution are identical to model of Foreman et al. (2008). Horizontal grid spacing ranges from 1 km on the southern British Columbia shelf to 5 km near the southeast corner of the model domain. Realistic atmospheric forcing and oceanic boundary conditions are used to create a hindcast of 2005.

The model is initialized at the start of the year, and analysis focuses on 1 May–15 October 2005, a period when an extensive array of shipboard and moored data available for model validation.

The ocean surface is forced with six-hourly winds from a regional atmospheric model (Mass et al., 2003). Additional variables from this atmospheric model are used to calculate surface heat flux using bulk algorithms (Fairall et al., 2003). For initial and boundary conditions of tracers and subtidal velocity, a composite of model output from 2005 was constructed from three hindcast models. At the southern boundary, daily output the Navy Coastal Ocean Model of the California Current System (NCOM-CCS) is utilized (Schulman et al., 2003). At the northern boundary, which is further north than the extent of the NCOM-CCS model domain, global NCOM is utilized (Kara et al., 2006). The western boundary of the composite contains both NCOM models, transitioning between the two at 47.5°N–48.8°N. In order to simulate estuarine exchange flow in the Strait of Juan de Fuca without modeling the smaller-scale flow in Puget Sound and the Strait of Georgia, the composite also contains low-pass filtered output from a 2005 version of the model described by Sutherland et al. (2011) at the eastern boundary. Freshwater input, most notably the Columbia River, is not included in the model. In addition to the subtidal fields described above, amplitude and phase for the K1, M2, O1 and S2 tidal constituents were obtained from a tidal model of the northeast Pacific (Foreman et al., 2000).

The 3D equations are solved using a 60-s internal time step, with 30 external 2D time steps for each internal time step. Advection of tracers and momentum are calculated using a third-order upstream scheme in the horizontal direction and a fourth-order centered scheme in the vertical. Vertical mixing is parameterized using the generic length scale turbulence closure scheme of Umlauf and Burchard (2003), with stability function constants from the "A" model of Canuto et al. (2001). Boundary conditions for barotopic velocity and sea surface height are described by Flather (1976) and Chapman (1985), respectively. Radiation conditions for baroclinic velocity and tracers are combined with adaptive nudging to all subtidal fields near the model boundary (Marchesiello et al., 2001). At the open boundaries, nudging time scales are 45 d for outgoing signals and 0.125 d for incoming signals. In the model interior, time scales for nudging increase exponentially from 45 d at the boundary to

60 d over a distance of six grid points. There is no nudging further in the interior of the model domain.

Bathymetry data is from the gridded Cascadia dataset (Haugerud, 2000), which has 250-m horizontal resolution. The model has twenty vertical levels and uses the stretching functions of Song and Haidvogel (1994) with θ_S =5.0 and θ_B =0.8. Minimum depth was set to 3 m in order to avoid drying of grid cells. Bathymetry was smoothed to reduce errors in the calculation of pressure gradients near steep topography. The topographic stiffness parameter $r_0 = |\Delta h|/2h$, where h is water depth (Beckmann and Haidvogel, 1993), has a maximum value of 0.24. The smoothed bathymetry retains Barkley, Juan de Fuca and Quinault canyons, which are located where resolution is high (Fig. 3.1a).

3.2.2 Model experiments

To explore sensitivity of modeled circulation to coastline and bathymetry, several model experiments were performed. Forcing and boundary conditions were identical to those described above for all model runs. In one experiment, the entrance to the Strait of Juan de Fuca was replaced with a closed boundary at Cape Flattery. In a second experiment, shelf bathymetry between 46°–49°N was replaced with "uniform" bathymetry where isobaths are defined by a radial coordinates:

$$z = -1500 + 1450 \tanh\left(\frac{R - R_0}{16}\right), \qquad 0 \le (R - R_0) \le 25 \text{ km} \tag{3.1a}$$

$$z = z_0 + z_0\left(\frac{R - R_0 - 25}{55}\right), \qquad (R - R_0) > 25 \text{ km} \tag{3.1b}$$

where z is depth in m, R is radius in km, $z_0 = -172$ m is the depth of the shelf break, and $R_0 = 560$ km. The center of the radial coordinate system was determined by fitting a circle to the 500-m isobath. This uniform bathymetry transitions to the original bathymetry over an alongshore distance of 25 km at 46°N and 40 km at 49°N. In a third experiment, this uniform bathymetry was further modified by adding a long canyon that extends to the coast. The canyon is designed to resemble Juan de Fuca canyon, with maximum depth 250 m, 22-km width at rim depth and 10-km width at the base. All grids in the model

experiments were smoothed in the same manner as the main run described in the previous section.

3.2.3 Particle tracking

Particle pathways were computed using the Lagrangian TRANSport model (North et al., 2008). In order to focus solely on the effects of advection, vertical and horizontal diffusion were set to zero. A 60 s time step was used for calculating particle trajectories from hourly model output. Particles were released at locations over the slope at the 250-m isobath out to 10 km further offshore, with 5-km spacing, between 46.4°N–49.0°N. Release depths range from 40–400 m, at 20 m intervals. Particles were released daily during the time period April–September and tracked for 15 days.

3.2.4 Observations

Observations from moorings and shipboard surveys during the period April–October 2005 are used to validate the model. Mooring data is used from the E2 mooring at the 47-m isobath, the RN mooring over the 70-m isobath, the E3 mooring over the 127-m isobath and the A1 mooring over the 500-m isobath (Fig. 3.1a). Velocity was measured at E2, RN and E3 with downward-looking 300 kHz Workhorse Acoustic Doppler Current Profilers (ADCPs, Teledyne RD Instruments). At E2, hourly ensembles were obtained 12–40 m with 2-m bin spacing. At RN, hourly ensembles were obtained at 3–63 m with 2-m bin spacing. At E3, hourly ensembles were obtained at 12–106 m with 2-m bin spacing. At A1 during this time period, velocity was measured using Aanderaa RCM8 current meters at 34 m, 102 m, and 301 m. The ADCP data were filtered with a cosine-Lanczos filter with half power point of 46 hours and decimated to 6 hr intervals. Each time series was rotated according to the principle axis of the depth-averaged velocity such that u is cross-shelf, positive towards shore, and v is alongshelf, positive in the poleward direction. The A1 velocity data were filtered using a Kaiser filter with 30 hr cutoff, decimated to daily intervals and rotated to the local isobath orientation (25° counter-clockwise).

Temperature and salinity data are used from selected depths at the E2, RN and E3

mooring sites. Temperature and conductivity measurements from 7–8 m off the bottom at E2 and E3 were collected by a SBE37 sensor (Seabird Electronics) at 15 min intervals. Data were averaged to hourly values, then low-pass filtered and decimated in the same manner as the ADCP data. Shipboard profiles of temperature and salinity data were collected by SBE 16*plus* sensors and averaged at 1 dbar intervals.

3.3 Model validation

In this section, the accuracy of the modeled circulation is evaluated using time series of velocity and density, as well as hydrographic data from shipboard surveys, in order to demonstrate the strengths and weaknesses of the model. In particular, the alongshore flow over the shelf and slope is evaluated because the strength and direction of the ambient flow is a key parameter in determining the upwelling flux in canyons. The presence of the Juan de Fuca eddy is evaluated because this mesoscale feature strongly influences regional circulation patterns, including equatorward flow along the outer shelf and upper slope. The density of shelf bottom water is evaluated as an indicator of the strength of seasonal upwelling.

3.3.1 Validation statistics

Several metrics are used to quantitatively summarize model skill. The correlation coefficient (CC) is a common measure of how well the model accounts for intraseasonal fluctuations in the observed time series. Because many of the time series have seasonal trends that bias this metric, the correlation coefficient of the detrended time series (CC_{DT}) is shown here. Significance levels were determined using effective degrees of freedom (Emery and Thomson, 2004, p. 260). The root mean squared error (RMSE) is used to quantify the overall model error for each location and variable. $\mathrm{RMSE} = (\langle (m-o)^2 \rangle)^{1/2}$, where o is an observation, m is a corresponding model variable, and $\langle\ \rangle$ denotes an average. The RMSE has units of the measured variable, and is comprised of three components, $\mathrm{RMSE}^2 = \mathrm{MB}^2 + \mathrm{SDE}^2 + \mathrm{CCE}^2$, where $\mathrm{MB} = \langle m \rangle - \langle o \rangle$ is the mean bias, $\mathrm{SDE} = S_m - S_o$ is the standard deviation error, and $\mathrm{CCE} = [2S_m S_o(1 - CC)]^{1/2}$ is the correlation error. The RMSE provides an intuitive measure of error expressed in units of the modeled variable. Willmott (1981) defines a skill

metric that normalizes the RMSE

$$\mathrm{WS} = 1 - \frac{\mathrm{RMSE}}{\langle(|m - \langle o\rangle| + |o - \langle o\rangle|)^2\rangle}, \tag{3.2}$$

which varies from 0–1. WS is used here to compare overall performance between different models.

3.3.2 Time series

Time series observations over the shelf span the period May–September 2005, allowing for an evaluation of model performance at time scales of weather events (∼2–10 d) and variability in velocity and water properties over several months. To provide a direct comparison with observations, model time series were interpolated to the positions and depths of the ADCP bins or temperature and conductivity sensors. To compare with a larger-scale, coarser-grid model, time series from the NCOM-CCS model were also extracted from the adjacent model grid points with the closest bottom depths. All modeled velocity vectors were rotated into the same coordinate frame as the observed time series.

3.3.2.1 Velocity

Modeled depth-averaged velocity is significantly correlated with observations at all locations over the shelf (Table 3.1, Fig. 3.2a,c,e). The strongest correlation is found at E2, and WS is high at this location for both models. This location is relatively shallow, and is therefore strongly influenced by local wind stress. Despite the relatively high correlation, the E2 location has the strongest mean bias of -0.05 m s^{-1} (Table 3.1, Fig. 3.2b,d,f), which may be due to an equatorward bias in the MM5 winds (Tinis et al., 2006). Over mid-shelf at RN (Fig. 3.2c,d), the correlation is weaker than at E2 and the WS metric indicates that skill is reduced from the NCOM-CCS model. Variability at mid-shelf in this region is strongly influenced by remotely-generated coastal trapped waves (Battisti and Hickey, 1984), so the smaller WS in the model used here is likely due to problems with nudging at the open boundaries. Despite the weak correlation with observations at this location, the model does show a seasonal peak in equatorward flow with correct timing and magnitude during mid-July. The observed mean vertical structure of alongshelf and cross-shelf velocity

is also similar to the observations (Fig. 3.2d). In deeper water offshore of Cape Flattery at E3, modeled variance is weaker than the observed variance (Fig. 3.2), similar to mid-shelf. However, the model shows an overall improvement over NCOM-CCS at this location (Table 3.1). This location is influenced by the outer limb of the Juan de Fuca eddy (Fig. 3.1b), which is associated with complex topography, tides and the estuarine outflow from the Strait of Juan de Fuca (Foreman et al., 2008; MacFadyen and Hickey, 2010). Model skill at E3 is therefore improved over NCOM-CCS due to higher resolution and inclusion of important local processes.

At the A1 site over the British Columbia slope, improvement over NCOM-CCS is found at 35 m but not 300 m (Fig. 3.3, Table 3.1). Modeled fluctuations are uncorrelated with observations at both depths, but the model does have an equatorward shelf break jet at 35 m, and a poleward undercurrent at 300 m. The strength of the equatorward jet is overestimated during periods in July–August (Fig. 3.3a), but the overall mean bias is small (-0.02 m s^{-1}). At 300 m, the RMSE at this depth is dominated by the CCE (0.05 m s^{-1}). The low correlation is likely related to problems incorporating remotely forced coastal trapped waves at the southern boundary, as suggested for mid shelf. The modeled flow at 300 m is equatorward during late May and early June, then becomes predominantly poleward during late July–September, similar to the observed variability over time scales of months (3.3b). This development of poleward flow during summer is representative of the expected seasonal cycle at this location (Thomson and Krassovski, 2010).

3.3.2.2 Near-bottom density

Comparisons with density time series from available near-bottom measurements at the shelf moorings are one measure of the model's representation of upwelling in the subsurface water column (Fig. 3.4). The best agreement with observed density is found 8 m above bottom at E2, the shallowest mooring site (Fig. 3.4a, Table 3.1). After a decrease in density associated with downwelling favorable poleward flow during May (Fig. 3.2a), modeled and observed density increase at this location to value of $\sigma_t \simeq 26.0$ kg m^{-3} by the end of the summer (Fig. 3.4a). Further offshore at E3, the model shows a small improvement over

NCOM-CCS (Table 3.1). The model misses a sharp increase in density during May, and the RMSE is dominated by the mean bias, -0.24 kg m^{-3}. The density bias is likely due to the initial and boundary conditions from the NCOM-CCS model, which tends to be fresher than observations at depth (Liu et al., 2009). Both model and observations indicate a gradual trend of increasing density during June–September, ∼0.25 kg m^{-3} over four months (Fig. 3.4c).

3.3.3 Shipboard surveys

Regional shipboard surveys do not resolve individual events, but provide greater spatial coverage over the Washington shelf. The inner shelf is excluded from this analysis in order to isolate the seasonal upwelling process, rather than the higher-frequency response to local wind stress in shallower water. Bottom temperatures at 40–200 m range from ∼6.5–10.5°C, and most measurements fall between 7–8°C (Fig. 3.5a). Salinity ranges from ∼32.5–34, and most measurements fall between 33.5–34 psu (Fig. 3.5b). A bias is evident in the deep salinity, but not in temperature. The mean bias in salinity determined from shipboard measurements of salinity is -0.28 psu, resulting in a density bias of -0.20 kg m^{-3}, which is consistent with bottom density at the E3 mooring. Since changes in density and density gradients are most relevant for studying upwelling, this bias is not a major concern. Removing the mean bias, the RMSE calculated for the bottom water properties are 0.34°C for temperature, 0.13 psu for salinity and 0.14 kg m^{-3} for density. These errors are smaller than the overall range present in shelf bottom water during April–September (Fig. 3.5).

Maps of shipboard surveys during July and September are used to compare regional patterns of observed and modeled circulation (Fig. 3.6). Temperature is shown instead of salinity or density because the lack of a mean bias facilitates visual comparison. A depth of 50 m is chosen because it covers the mid–outer shelves, and represents seasonal upwelling away from the higher frequency variability of the shallower inner shelf. Note that the surveys take place over 1–2 week periods, which means that small scale spatial variability in the maps may be associated with temporal variability. During July, in both the model and observations, the coldest water (<7.5°C) is present in the Juan de Fuca

eddy and directly adjacent to Cape Flattery. Outflow from the Strait of Juan de Fuca is 0.5–1°C warmer than observations, but upwelled water <8°C is found at 50 m along the Washington coast in both the model and observations. Seasonal changes between the two surveys are evident in the eddy and coastal upwelling regions. The modeled eddy core (<7.5°C) is located further offshore and has a larger horizontal extent during September, as observed. The strongest upwelling along the Washington coast is located further south than during July. Water offshore is several degrees colder than observed, which may indicate an underestimate of surface heat flux. This comparison with shipboard surveys shows that the model is accurately representing upwelling near the coast and in the Juan de Fuca eddy region, as well as changes in the patterns of upwelling at time scales of months.

3.4 Results

Comparison with regional-scale observations in the previous section shows that the primary strength of the model is variability at time scales of months, as shown by the properties of upwelled bottom water and the development of the Juan de Fuca eddy during summer. Modeled velocity compares most favorably with observations of the mean vertical structure and over time scales of months, especially at locations where the shelf break jet interacts with topography and mesoscale features such as the British Columbia slope and the outer shelf offshore of Cape Flattery. The primary weakness of the model is the poor agreement of intraseasonal fluctuations at the event time scale, which are strongly influenced by remote winds outside of the model domain. While timing and strength of individual events may differ from reality, the model can be used for determining factors that contribute to the seasonal increase in density over the shelf.

Comparison with the 2005 observations addressed the scales of upwelling, but not the smaller-scale canyon processes that were hypothesized to contribute to upwelling (see Section 3.1). Although no observations are available at the smaller scales of submarine canyons during this time period, several observational canyon studies have taken place in this region. In Section 3.4.1, the modeled circulation near shelf break canyons is shown under different ambient forcing conditions, using observed relationships between velocity and temperature from previous studies to demonstrate that the model does represent dynamics expected

during canyon upwelling. The impact of canyons on seasonal upwelling is then determined by analyzing the source depths of passive particles that are upwelled onto the shelf (Section 3.4.2) and cross-isobath fluxes over the slope in salt budgets of the shelf (Section 3.4.3). In Section 3.4.4, spatial variability in the cross-shelf momentum balance is shown to be associated with bathymetric features over the slope.

3.4.1 Circulation in shelf break canyons

In this section, time series of modeled velocity and temperature are shown for locations where previous canyon observational studies have taken place in order to 1) demonstrate consistency with past observations and 2) define periods of downwelling, upwelling and relaxation based on the incident velocity near the heads of canyons. Fields of velocity, density and vorticity are used to provide a more complete view of the modeled circulation at Barkley and Quinault canyons during different types of conditions. Downwelling and upwelling events are compared at Barkley Canyon. Circulation in Quinault canyon and the adjacent Washington shelf are compared during upwelling and subsequent relaxation.

3.4.1.1 Downwelling and upwelling – Barkley canyon

Barkley canyon, located at the shelf break off British Columbia, has a width typical of shelf break canyons and close to the local deformation radius (∼10 km). Mooring time series near the head (see Fig. 3.7a,b for location) have demonstrated a correlation between temperature fluctuations within the canyon at 230 m and incident velocity at 100 m (Allen et al., 2001). Model time series from the same location also show a significant correlation between temperature at 230 m and alongshore velocity above the canyon at 100 m (Fig. 3.7c). Although it is difficult to compare model and observations from different years, the temperature fluctuations observed by Allen et al. (2001) have greater magnitude (ranging from 6–7.5°C instead of 6–6.8°C), suggesting that the model may underestimate the upwelling response. However, the decrease of temperature during equatorward flow events indicates that model produces upward displacement of isotherms in the canyon with correct timing in relation to the incident flow. The modeled temperature fluctuations at 230 m

are not correlated with the modeled alongshore velocity at 230 m (Fig. 3.7c), as might be expected if the isotherms were adjusting to geostrophic flow at the same depth. At 230 m, alongshore velocity is generally weak, and poleward flow events lag cold temperatures by several days. As will be seen shortly, these poleward flow events are associated with the formation of a closed rim depth eddy.

The time series indicate a transition from poleward to equatorward velocity at 100 m during 22–26 May (Fig. 3.7c), providing an opportunity to compare canyon circulation during upwelling and downwelling conditions. On 22 May, poleward flow is present near the bottom over the shelf and 180 m over the slope (Fig. 3.7a). Poleward flow is diminished within the canyon, but there is no evidence of a strong component toward or away from the head. After the transition to equatorward flow, on 26 May, temperature at 230 m drops by $\sim$0.3°C (Fig. 3.7c). Over the shelf, near-bottom flow is directed equatorward (Fig. 3.7a). At 180 m, alongshore flow over the slope is relatively weak, and there is a transition to poleward flow further offshore. Flow within the canyon is directed onshore. At the canyon head, near-bottom shelf flow crosses isobaths and turns anti-cyclonically, carrying dense water to the southeast. The comparison between these two events indicates that the circulation transitions rapidly (within four days) between a downwelling situation with little net exchange, and an upwelling situation in which upcanyon flow advects dense water onto the shelf.

The strongest equatorward flow passing over Barkley canyon, and the coldest temperature at 230 m within the canyon, occur on 20 July in the model (Fig. 3.7c). During this time, equatorward flow of magnitude $\sim$0.1 m s^{-1} is present at the shelf break near the bottom and over the slope to the north of the canyon (Fig. 3.8a). A pool of dense water, $\sim$0.2 kg m^{-3} more dense than further offshore, is present at the head of the canyon. Flow crosses isobaths near the canyon head, especially at the south side, and dense water is advected to the southeast over the shelf. Flow patterns are similar to the May upwelling event discussed above, but with denser upwelled water. Three days later on 23 July, equatorward flow over the shelf is weaker (Fig. 3.7c, 3.8b). At 180 m, a cyclonic rim-depth eddy is associated with poleward flow at the canyon head. During peak upwelling on 20 July, cyclonic relative vorticity is associated with the steering of flow towards the canyon head

(Fig. 3.8c). Following peak upwelling on 23 July, the region of strongest relative vorticity detaches from the canyon head and is located at the center of the rim-depth eddy (Fig. 3.8d). The modeled relative vorticity has a peak magnitude of $1.2f$. For comparison, Allen et al. (2001) estimated relative vorticity with magnitude of $0.3f$ in Barkley canyon using a diagnostic model, and $1.7f$ by estimating stretching of isopycnals from hydrographic data (the observational estimate was considered an overestimate due to the assumption of no dissipation). The timing of eddy formation several days following the strongest equatorward flow is consistent with the observational study of Hickey (1997) in Astoria canyon.

3.4.1.2 Upwelling and relaxation – Quinault canyon and the Washington shelf

Quinault canyon, located on the shelf break of Washington, differs from Barkley canyon in that it is ∼30 km wide, 3 times wider than the local deformation radius. However, upwelling has been observed in association with equatorward flow events at this location. Hickey (1989) compared near-bottom alongshore velocity and temperature at two locations over the 150-m isobath (see Fig. 3.9a,b for locations). Unlike the period analyzed in this model study, mean flow was directed poleward during the fall observations. During reversals to equatorward flow, cold water was observed near the head of the canyon and no clear response was found at the open slope location. Similar behavior is evident in the modeled time series at the same locations (Fig. 3.9c). Alongshelf velocity over the open slope is not significantly correlated with temperature at the same point, but does account for 53% of the variance in temperature at the canyon head and 60% of the temperature difference between the head and open slope.

At this location, the strongest upwelling in the model occurs on 16 July (Fig. 3.9c), four days earlier than the peak upwelling at Barkley canyon. This event occurs soon after the onset of strong upwelling-favorable winds (Fig. 3.9d). Like the Barkley canyon event, cross-isobath flow is evident at the head of the canyon and relatively dense bottom water is advected to the southeast (Fig. 3.9a). Offshore flow south of the canyon is associated with relatively warm water at the open slope time series location (Fig. 3.9c). A closed cyclonic eddy is present at 180 m, but the relative vorticity is smaller than in the Barkley canyon

eddy described above. Because Quinault canyon is approximately three times wider than Barkley canyon, the horizontal shear in a rim depth eddy that fills the canyon is weaker for velocity of the same magnitude.

Two weeks later on 31 July, relaxation from persistent upwelling-favorable wind stress results in much different conditions near the canyon (Fig. 3.9b,d). Velocity over the shelf is close to zero and temperature is nearly identical at the open slope and canyon head locations (Fig. 3.9b,c). Poleward flow, the California Undercurrent, is present over the slope and follows the bathymetry of Quinault canyon (Figs. 3.9b). The presence of undercurrent does not necessarily cause the lack of canyon upwelling in this case; shelf flow relaxes at the same time the undercurrent strengthens.

A broader view of the near-bottom and offshore circulation indicates that the poleward undercurrent is weak at all latitudes during 16 July but flows continuously over the slope on 31 July (Fig. 3.10). This difference is consistent with observations over the British Columbia slope (Fig. 3.3b). Currents in Juan de Fuca canyon also vary between the upwelling and relaxation events. Upcanyon velocity is much stronger during the upwelling event on 16 July, as is the near bottom shelf flow to the south of the canyon.

3.4.2 Source depth

In the previous section, modeled equatorward flow events were shown to be associated with dense water at the heads of canyons and at nearby shelf locations. In this section, in order to demonstrate that canyons influence the source depth of upwelled water throughout the season, trajectories are tracked for passive particles that are upwelled from the slope to the mid shelf of Washington. Particles were released daily throughout the water column (40-400 m, every 20 m) during April–September and tracked for 15 d (see Section 3.2.3 for details). The 15-d time scale is used because it encompasses entire upwelling events and allows the canyon upwelling process to be fully set up (Klinck, 1996). Particles transported inshore of the 100-m isobath on the mid shelf are tracked, as opposed to further offshore at the outer shelf, because these locations have greater potential to reach the euphotic zone and/or impact hypoxic events. Particle trajectories from model experiments with different

coastlines and bathymetry (see Section 3.2.2 for details) are also analyzed in order to provide further evidence for the effects of bathymetry on source depth.

The deepest source depths (200–260 m) for the Washington mid shelf in the "main" model run are associated with particles that originate near Quinault canyon and the mouth of Juan de Fuca canyon (Figure 3.11a). Particles with relatively deep source depths (160–180 m) also originate near Barkley canyon, located further north on the British Columbia shelf. A histogram of source depths for all the mapped trajectories shows a peak at 140 m, superimposed on a decrease in the number of particles with depth (Fig. 3.12a). At the end of the 15-d trajectories, upwelled particles are concentrated near the bottom (Fig. 3.12b). 28% of the upwelled particles are found within 10 m of the bottom, and the number of upwelled particles decreases with greater heights above the bottom.

Since it is possible that the upwelling through Juan de Fuca canyon could be influenced by the sharp coastline curvature at Cape Flattery, particles were also tracked for an identical run with a closed boundary at the entrance to the Strait of Juan de Fuca (Fig. 3.11b). Locations of deep upwelling (deeper than 150 m, approximately the depth of the shelf break) are similar to the main case, but no deep particles are upwelled directly adjacent to Cape Flattery. Also, Barkley canyon is no longer a source of deep upwelled water. Even though the trajectories of the deepest upwelled water have similar patterns in this case, the histogram of source depths indicates that the subsurface peak at 140 m is eliminated (Fig. 3.12a). However canyon upwelling is clearly not shut down, and source depths are still found to be as deep as 240 m. As with the main run, the greatest number of upwelled particles over the shelf are found near the bottom after 15 d (Fig. 3.12b). It is important to note that removing the estuarine outflow from the Strait of Juan de Fuca completely changes the character of the regional circulation by removing the Vancouver Island coastal current and the Juan de Fuca eddy (not shown). Differences in source depth occur not only near Cape Flattery, but also at shelf break canyons due to shifts in the equatorward jet. This run therefore highlights the importance of modeling the appropriate incident flow over the canyons at the shelf break.

For comparison to a case without canyons, the model was also run with the same forcing and boundary conditions, but completely modified bathymetry that is uniform in the

alongshelf direction (Fig. 3.11c). In this case there is a large-scale gradient with deeper source depths to the south, but no locations where source depths exceed the depth of the shelf break at ∼150 m (Fig. 3.12a). At the end of the 15-d trajectories, the majority of particles are located 40–70 m above the bottom and none are found in the bottom 10 m (Fig. 3.12b).

In the final model run, a canyon with geometry resembling Juan de Fuca canyon is added to the uniform shelf in order to isolate the effect of this canyon from the other complex bathymetric features of the region. In this case, source depths deeper than 140 m are present, and a secondary peak in source depth occurs at 200 m (Fig. 3.12a). Upwelled particles associated with this enhancement are found near the bottom (Fig. 3.12b). This long canyon geometry not only provides deep source depths, but also brings particles that have been upwelled from the slope close to the inner shelf (Fig. 3.11d).

3.4.3 Salt budget

The previous section showed that submarine canyons influence the source depth of upwelled water, allowing for upwelling of water to mid shelf from below the depth of the shelf break at ∼150 m. However, the source depths of passive particles cannot be directly related to seasonal changes in tracers over the shelf. In this section, cross-isobath fluxes of salt are quantified and shown to be enhanced near canyon topography. Salt budgets for the shelf are analyzed in order to directly compare cross-isobath fluxes over the slope with integrated changes in salt content over the shelf.

3.4.3.1 Formulation

Salt budgets are analyzed for two separate volumes on the British Columbia and Washington shelves (Fig. 3.1a). Each are bounded by a closed coastal boundary, an open offshore edge defined by an isobath, and northern and southern edges oriented approximately perpendicular to the coast. Shelf-slope exchange is defined by fluxes across the 180-m isobath, which is located over the upper slope and is within 20 m of the rim depths of canyons on both the British Columbia and Washington shelves. To show how upwelled water reaches

mid shelf, fluxes across the 120-m isobath are also examined off Washington, where the shelf bathymetry is relatively simple. Salinity is used as tracer because it is conserved in this setting and is not affected by atmospheric sources and sinks at the surface.

In the absence of sources or sinks of fresh water, the salt budget for a volume can be written as

$$\frac{\partial}{\partial t}\int_V S dV = \int_A S(\vec{\mathbf{u}}\cdot\hat{n})dA, \tag{3.3}$$

where V is volume, A is area, $\vec{\mathbf{u}}$ is velocity, and $\hat{n}$ is the unit vector normal to the vertical boundaries. The left hand side of (3.3) represents salt storage, the change in volume integrated salt with respect to time. The right-hand side represents fluxes of salt into the volume due to physical transport. The horizontal coordinates of the vertical open boundaries do not change, but and the total volume V vary in time due to changes in the free surface height. The total area A is the sum of the areas of the offshore edge A_{off}, northern edge A_n, and southern edge A_s.

The salt budget in this model study is decomposed in a similar manner as the three-dimensional heat budget in the observational study of Lentz (1987). Salinity on the offshore, northern and southern edges are decomposed as

$$S_{off} = \langle\langle S_{off}\rangle\rangle + \widetilde{S}_{off}, \tag{3.4a}$$

$$S_n = \langle\langle S_n\rangle\rangle + \widetilde{S}_n, \tag{3.4b}$$

$$S_s = \langle\langle S_s\rangle\rangle + \widetilde{S}_s, \tag{3.4c}$$

where subscripts denote separate edges of the volume, $\langle\langle\ \rangle\rangle$ is a time-varying spatial average over each edge, and $\widetilde{}$ represents a perturbation from the spatial average. Velocity across each edge is decomposed similarly,

$$(\vec{\mathbf{u}}\cdot\hat{n})_{off} = Q_{off}A_{off}^{-1} + \widetilde{u}_{off}, \tag{3.5a}$$

$$(\vec{\mathbf{u}}\cdot\hat{n})_n = Q_n A_n^{-1} + \widetilde{u}_n, \tag{3.5b}$$

$$(\vec{\mathbf{u}}\cdot\hat{n})_s = Q_s A_s^{-1} + \widetilde{u}_s, \tag{3.5c}$$

where Q is the time-varying volume transport through the edge into the volume. In this study, positive Q and $\widetilde{u}$ are directed into the volume.

The advective flux in (3.3) can be decomposed into the flux due to transport and the fluxes associated with perturbations of salinity and velocity fields. The transport salt flux is defined as

$$F_T = Q_{off}\langle\langle S_{off}\rangle\rangle + Q_n\langle\langle S_n\rangle\rangle + Q_s\langle\langle S_s\rangle\rangle, \tag{3.6}$$

Neglecting the changes in volume associated with fluctuations in sea surface and assuming $Q_{off} = -(Q_n + Q_s)$, the transport salt flux can alternatively be expressed as

$$F_T = Q_n\big(\langle\langle S_n\rangle\rangle - \langle\langle S_{off}\rangle\rangle\big) + Q_s\big(\langle\langle S_s\rangle\rangle - \langle\langle S_{off}\rangle\rangle\big). \tag{3.7}$$

The transport salt flux accounts for fluxes of salt associated with net volume transport across each edge. If transports through the northern and southern edges are identical, then F_T represents the advection of a large scale salinity gradient through the volume. Having removed the net transport and mean salinity at each edge, the fluxes associated with the spatial perturbations of velocity and salinity are defined as

$$F_{off} = \int_{A_{off}} \widetilde{u}_{off}\widetilde{S}_{off}dA, \tag{3.8a}$$

$$F_n = \int_{A_n} \widetilde{u}_n\widetilde{S}_n dA, \tag{3.8b}$$

$$F_s = \int_{A_s} \widetilde{u}_s\widetilde{S}_s dA. \tag{3.8c}$$

The terms F_{off}, F_n and F_s will be referred to as the offshore, northern and southern salt fluxes, respectively. The salt budget in (3.3) can then be expressed as

$$\frac{\partial}{\partial t}\int_V SdV = F_T + F_{off} + F_n + F_s. \tag{3.9}$$

As noted by Lentz (1987), this kind of decomposition is useful for calculating heat budgets because the fluxes are not sensitive to the temperature scale used. For this study, it also conveniently removes the effect of a mean bias in the modeled salinity (Section 3.3), since

all terms are based on changes in or differences in salinity. Decomposing the budget in this way is also useful because the cross-isobath exchange associated with canyons is inherently associated with spatial variability at the offshore edge. Isolating the effects of the net volume transport in F_T, as well as the net perturbation fluxes through northern and southern edges ($F_n + F_s$), conveniently separates scales by removing the effects of advection on scales larger than the control volume in this complex three-dimensional system. Discussion will primarily focus on the variability and structure of the cross-isobath salt flux at the offshore edge, F_{off}.

3.4.3.2 Depth distribution of cross-isobath fluxes

To determine where in the water column this cross-isobath flux occurs, spatial variations in the June–September mean of $\widetilde{u}_{off}\widetilde{S}_{off}$ are examined. June–September is chosen for analysis because winds are predominantly upwelling favorable and upwelling through canyons has been shown to occur in the model during this period (Figs. 3.7c, 3.9c,d). The mean offshore salt flux is divided into the flux due to the mean velocity and salinity fields and the eddy flux due to the correlations of velocity and salinity fluctuations

$$\overline{\widetilde{u}\widetilde{S}} = \bar{\widetilde{u}}\bar{\widetilde{S}} + \overline{\widetilde{u}'\widetilde{S}'}, \tag{3.10}$$

where $\bar{}$ denotes the time mean and $'$ denotes fluctuations about the time mean.

Vertical profiles are calculated as averages over the offshore isobaths of the two control volumes (Fig. 3.13). Over the 180-m isobath over the slope, mean profiles of velocity have a three-layer structure over the continental slopes of both Washington and British Columbia (Fig. 3.13a). Flow is directed offshore within ∼15–20 m of the surface and bottom, consistent with a surface Ekman transport associated with equatorward wind stress and a weaker bottom Ekman layer associated with poleward flow over the upper slope. The onshore "return flow" that compensates for this offshore transport in the boundary layers is centered at 140-m depth. Cross-isobath flow is weakest in the 20–100 m depth range.

Positive values of $\overline{\widetilde{u}_{off}\widetilde{S}_{off}}$ occur in the upper 20 m of the water column, where there is offshore flow of relatively fresh water in the surface Ekman layer, and also at the depths of the interior return flow at 80–160 m (Fig. 3.13b). The mean onshore flux of relatively

salty water in this lower layer exceeds the offshore flux in the bottom boundary layer by a factor of 1.5–2.0, and contributes ∼33–51% as much to F_{off} as the offshore flux of relatively fresh water in the surface layer. The eddy flux makes a small contribution to the total flux near the surface, but is much smaller than the flux associated with the mean fields. The June–September mean of F_{off} is dominated by the mean fields of velocity and salinity at all depths.

To determine the depth distribution of the salt flux further onshore over the shelf, mean vertical profiles were also calculated over the 120-m isobath off Washington, where the bathymetry slopes upward towards the coast at all locations (unlike the more complex bathymetry of the British Columbia shelf). This isobath runs close to Quinault canyon, but does not bend sharply towards the coast like the 180-m isobath (Fig. 3.1). In contrast to the slope, the onshore return flow that compensates for the surface Ekman transport at the 120-m isobath occurs primarily in the bottom boundary layer, along with onshore flux of salt (Fig. 3.13c,d). There is also a weak interior flow that contributes to a small onshore salt flux at 70–100 m. After salt and other tracers cross the 180-m isobath in the layer centered at 140 m over the slope, the onshore bottom boundary layer over the outer shelf provides a mechanism for retention and further movement towards shore.

3.4.3.3 Locations cross-isobath fluxes in the lower water column

The horizontal distribution of $\overline{\widetilde{u}_{off}\widetilde{S}_{off}}$ at 140 m, the depth of the peak return flow over the slope, is not uniform (Fig. 3.14). Sites of onshore salt flux include the southern sides of Quinault and Barkley canyons, which were the focus of Section 3.4.1 due to the presence of past observations. Onshore flux at this depth occurs exclusively on the southern sides of canyons and other locations where slope isobaths bend inward toward the coast. Further onshore over the 120-m isobath off Washington, onshore flux in the bottom boundary layer at 117-m depth is also spatially variable, but is not restricted to the south sides of topographic depressions. There is a location of offshore recirculation downstream of Quinault canyon, towards the open slope time series location shown in Figure 3.9. The spatial distribution of the offshore salt flux shows that upwelling from the slope to the shelf occurs primarily near

topographic depressions such as canyons, and that the onshore bottom boundary layer over the shelf is important for transporting tracers that have been upwelled through canyons further onshore.

3.4.3.4 Time-varying budget

The spatial distribution of $\widetilde{u}_{off}\widetilde{S}_{off}$ indicates large positive values near the surface due to offshore flux of relatively fresh water, with smaller values in the lower part of the water column that are associated with topographic variability. To demonstrate the importance of the deeper onshore salt flux in the lower part of the water column, the offshore flux F_{off} is separated into the lower and upper halves of the water column, and compared with changes in salt over over the shelf. The cumulative changes in salt, averaged over the shelves during June–September, are ∼0.3–0.4 psu for the Washington and British Columbia shelves (Fig. 3.15a,b). The cumulative offshore flux in the lower half of the water column contributes the same amount over the Washington shelf, and slightly less over the British Columbia shelf due to a downturn during September.

Compared with the offshore flux in the lower water column, the time rate of change in salt (the storage term) is associated with higher-frequency variability at the time scales of wind events (Fig. 3.15c,d). Much of this higher frequency variability is associated with fluctuations in F_{off} closer to the surface (Fig. 3.15e,f). A large positive component of F_{off} in the upper half of the water column, also shown in the vertical profiles (Fig. 3.13), increases throughout the upwelling season until October off the Washington shelf (Fig. 3.15e). This trend throughout the summer is balanced by a loss of salt, which associated with the sum of the transport flux and the flux through the northern and southern edges ($F_T + F_n + F_s$). These terms are associated with alongshore variability in salinity and velocity, and this balance is therefore associated with the three dimensional structure of coastal upwelling in this region. On the Washington shelf, the upwelling front is typically broader and more dense to the south (Figs. 3.1b, 3.6c,d). As relatively fresh water is advected offshore in the surface boundary layer, contributing to positive F_{off} near the surface, salty water is brought closer to the surface where there is strong equatorward flow and advected away from

the shelf to the south, contributing to loss of salt. Off British Columbia, a similar pattern of increasing F_{off} at the surface is present until early September (Fig. 3.15f). Qualitative changes in all terms of the budget during September may be related to the lateral expansion of the Juan de Fuca eddy, which is not a focus of this study.

The time series show that the large positive component of F_{off} near the surface over the slope is largely balanced by fluxes associated with alongshore variability at the seasonal time scale. The cross-isobath flux in the lower part of the water column, whose spatial variability is strongly linked to the canyon topography, contributes enough salt to account for the seasonal increase through most of the summer upwelling season.

3.4.4 Cross-shelf momentum balance

The salt budgets in the previous section showed that fluxes over the slope, and in particular through submarine canyons, are important for quantifying seasonal changes in tracers over the shelf during the upwelling season. Onshore fluxes occur above the bottom boundary layer, in the lower part of the water column on the downstream sides of canyons. In this section, spatial and temporal variability in the cross-shelf momentum balance is examined to demonstrate where and why geostrophic balance breaks down in the alongshore flow, producing a net force across isobaths. The equation governing conservation of cross-shelf momentum, u, is

$$\underbrace{\frac{\partial u}{\partial t}}_{\text{ACCEL}} = \underbrace{-\nabla\cdot(\vec{\mathbf{u}}u)}_{\text{ADV}}\underbrace{-\frac{1}{\rho_0}\frac{\partial p}{\partial x}+fv}_{\text{AGEO}}+\underbrace{\frac{\partial}{\partial z}\left(K_M\frac{\partial u}{\partial z}\right)}_{\text{VVISC}}, \tag{3.11}$$

where p is pressure and K_M is the eddy viscosity. The ACCEL term represents unsteady acceleration at a fixed point, ADV represents momentum advection, AGEO is the ageostrophic term obtained by summing the pressure gradient and Coriolis forces, and VVISC is the viscous force associated with vertical mixing of momentum. For an alongshore current in geostrophic balance, all of these terms are equal to zero. To investigate where and how geostrophic balance breaks down over the slope, allowing for significant cross-isobath tracer flux to occur, the spatial distribution of the mean terms in (3.11) are analyzed for the period June–September.

Average vertical profiles during this time were calculated for the 180-m isobath over the slopes of British Columbia and Washington (Fig. 3.16a,b). The profiles are averaged over the same segments used to calculate average cross-isobath velocity profiles and salt fluxes in previous section, with the cross-isobath direction defined as component normal to the isobath. Acceleration is small when averaged over the long four-month time period of June–September, resulting in a steady balance. The largest magnitudes of terms in (3.11) are found in the surface boundary layer, where the ageostrophic term is balanced by the viscous term. These two terms also balance near the bottom, though with smaller magnitudes. All terms are small at depths of 20–120 m, indicating the presence of geostrophic balance in a large portion of the upper interior water column. At 120–170 m, the ageostrophic term is positive and balanced by the advection term. The ageostrophic force indicates a net unbalanced pressure-gradient force towards shore, which is associated with steady acceleration of fluid parcels in the onshore direction. The ageostophic force and momentum advection occur in the same part of the water column as onshore salt flux (Fig. 3.13b).

Since the cross-isobath salt fluxes are not evenly distributed over the slope are enhanced near canyons (Fig. 3.14), it is also important to also consider horizontal variations in the cross-shelf momentum balance. At at 180 m near Barkley and Quinault canyons, close to the rim depths of both canyons, the ageostrophic term is highly variable in space (Fig. 3.16c,d). This term is positive where the isobaths curve towards shore at the upstream (in terms of the equatorward shelf flow) sides of the canyons, as well as other locations where the bathymetry extends out towards the open ocean. The ageostrophic force is negative at the heads of both canyons. Note that the ageostrophic term is primarily balanced by the advection term in these maps, and the viscous term is confined to a narrow region that does not extend more than one grid point offshore (not shown). This spatial pattern indicates that positive mean ageostrophic forces (i.e. unbalanced pressure gradients in the onshore direction) are not co-located with the largest onshore fluxes, but are located at the upstream sides of the canyons.

To investigate whether variability in the magnitude and structure of the ageostrophic term can be linked to the velocity and temperature fluctuations near canyons shown in Section 3.4.1, empirical orthogonal functions (EOFs) are analyzed at 180 m near Barkley

canyon. The spatial structure of the first mode is characterized by strongest variability at the head of the canyon, near the upstream side (Fig. 3.17a). A zero crossing is aligned perpendicular to the canyon axis. The structure and amplitude of the first mode shows that it is associated with three major events (Fig. 3.17c). As shown earlier in Fig. 3.7c, these same events are associated with poleward flow within the canyon near the head, indicative of a closed eddy. The highest amplitude of this first mode occurs on July 23, concurrent with high values of vorticity following the peak of the strongest upwelling event of the summer at Barkley canyon (Fig. 3.8c). The structure of the EOF indicates that ageostrophic forces are directed inward towards the center of the eddy during these events. Dense water near the canyon head following upwelling contributes to an offshore-directed ageostrophic force there.

The second EOF mode is characterized by strongest variability on the upstream side of the canyon (Fig. 3.17b). This second mode is associated with onshore ageostrophic force throughout the canyon (except for the very tip of the head) during periods preceding the mode-1 peaks (Fig. 3.17b,c). These events coincide with the appearance of southward flow above the canyon and cold water near the canyon head (Fig. 3.8c), for example on 20 July. The amplitude reverses throughout August, indicating the tendency for an offshore ageostrophic force during this period when there is weak equatorward flow over the outer shelf (Fig. 3.8c) and a strong poleward California Undercurrent (Fig. 3.3b).

3.5 Summary and Discussion

In this study, a regional numerical model is used to estimate the impact of submarine canyons on seasonal upwelling in the subsurface water column over the continental shelf. Seasonal changes in the density of shelf bottom water in the model are consistent with moored and hydrographic observations. Correlations between equatorward flow over the outer shelf and cold water near the canyon heads, consistent with past observational studies, indicate that the model includes the dynamics of upwelling in shelf break canyons. The small-scale canyon dynamics are related to the regional-scale upwelling process by examining the source depth of passive upwelled particles and analyzing of the contribution of cross-isobath fluxes to the salt budget over shelf. Key results are summarized below:

- Submarine canyons are associated with enhanced upwelling of tracers and particles from the slope to the shelf. In contrast to other slope locations, canyons allow for upwelling from source depths greater than 150 m over the slope to the near-bottom water over mid shelf.

- Enhanced onshore flux over the slope occurs in the lower part of the interior water column on the downstream side of canyons and topographic depressions. This flux is an important contributor to seasonal changes in volume-averaged salinity over the shelf.

- Mean cross shelf momentum balances indicate a net balance between an onshore ageostrophic force and momentum advection over the slope. In Barkley canyon, the onshore ageostrophic force on the upstream side is enhanced during southward flow. Offshore ageostrophic forces near the canyon head are enhanced when closed eddies are present in the periods following upwelling.

Submarine canyons allow for direct upwelling from the slope to the near-bottom water at mid shelf. Source depths for mid-shelf water in the main model run occur as deep as 260 m, but show a pronounced peak in frequency at 140 m (Fig. 3.12a). The vertical structure of the cross-isobath salt flux also shows a subsurface maximum at 140 m (Fig. 3.13a,b). The Lagrangian and Eulerian methods both suggest that water continues further onshore in the bottom boundary layer. Particles are concentrated near the bottom after 15 days (Fig. 3.12a), where onshore flow is located in the bottom boundary layer (Fig. 3.13c,d). The time scale for particles to reach the inner shelf is longer than 15 days, and it is likely that much of the upwelled water is advected further south. In a Lagrangian study of upwelling during the same year off Oregon, Rivas and Samelson (2011) found that few particles were upwelled from the slope to the inner shelf over the course of 6-month trajectories. Many originated at the north boundary, and canyon upwelling off Washington and British Columbia likely influences the properties of this water.

The modeled salt budgets indicate that the increase in salt over the shelf throughout the upwelling season is associated with mean advection of the mean salinity field (Section

3.4.3.3). This suggests that the dynamics inferred from model studies with steady forcing (Klinck, 1996; She and Klinck, 2000; Allen and Hickey, 2010), can be extended to regions with high variability such as the northern CCS, where wind fluctuations at periods of 5–10 days are common during the summer upwelling season. The lack of a strong eddy flux contribution is consistent with the study of Kämpf (2009), who modeled the response to a superposition of oscillatory and mean ambient flow, and found the net upwelling associated with the oscillatory component to be small when averaged over several cycles.

Spatial patterns in the mean cross-shelf momentum balance (Section 3.4.4) can be understood in terms of an equatorward shelf jet encountering the canyon bathymetry. The northern (upstream) side is where positive relative vorticity is generated. As fluid columns stretch in order to conserve potential vorticity, momentum is transfered from the equatorward jet to the onshore upwelling stream through advection, and the associated reduction of equatorward v at canyon depths leads to an unbalanced onshore pressure-gradient force at the same location. The focused steady acceleration of fluid parcels towards shore at the upstream side of the canyon highlights the importance of realistic bathymetry at this location. Scaling analysis of canyon upwelling has suggested that the upstream radius of curvature is a crucial parameter in determining flow separation and total upwelling flux (Allen and Hickey, 2010).

The negative ageostrophic force at the heads of the canyons is explained using similar reasoning. Upwelling of dense water at the canyon head can reduce, or even reverse, the onshore component of the pressure-gradient force associated with the equatorward jet. At the same time, the onshore upwelling flow encounters shallower water and turns anticyclonically to follow isobaths, transferring momentum from the upwelling stream back into the equatorward shelf jet. Even though the signs of the terms in the cross-shelf momentum balance are highly variable along the slope, vertical profiles averaged along the 180-m isobath show that the net forcing is directed onshore (Fig. 3.16c,d). A reversal in the direction of the ageostrophic force to offshore at the heads of canyons is consistent with the dynamical balance shown in the modeling study of She and Klinck (2000). In contrast to earlier studies (e.g. Klinck, 1996), the model of She and Klinck (2000) included a rim-depth eddy and emphasized the importance of momentum advection, which are also features of

the modeled dynamics presented here.

In addition to the shelf break canyons whose dynamics are well-studied, the present study highlights the regional importance of Juan de Fuca canyon, a long canyon that cuts through the shelf and extends into a large estuary. Upcanyon flow was modeled during upwelling and relaxation events (Fig. 3.10). This is consistent with the winter and fall observations of Cannon (1972), which showed persistent up-canyon flow interrupted by reversals only during storm events. During relaxation, the Juan de Fuca eddy is more retentive, and poleward flow near Cape Flattery is associated with an offshore cross-shelf pressure gradient force, which decelerates the upcanyon transport of fluid parcels. Tidally rectified vertical velocities may be important near Cape Flattery, as suggested by Foreman et al. (2008), but upwelling is present in the experiment without Cape Flattery and also using simplified shelf topography with a long canyon (Fig. 3.11b,d). This experiment indicates a relatively deep source depth of $\sim$200 m for the geometry of Juan de Fuca canyon. Particles upwell close to the inner shelf, much closer to shore than particles that upwell through the shelf break canyons. Theoretical and laboratory studies of long canyons suggest the convergence of isobaths in long canyons allows for significant upwelling during weak, steady flow and should therefore be especially important at the seasonal time scales considered here (Allen, 2000; Waterhouse et al., 2009). Dynamical understanding of these types of canyons may would be improved by numerical studies of parameters such as length, width and stratification, which are beyond the scope of this study.

One dynamical aspect of upwelling in shelf break canyons that is not currently well understood is the influence of a poleward undercurrent. Because the pressure-gradient force associated with geostrophic poleward flow is directed offshore, it is sometimes assumed that the development of the California Undercurrent shuts down canyon upwelling in the northern CCS after June (Hickey and Banas, 2008). The model in this study has an undercurrent that develops after June, consistent with observations over the British Columbia slope (Fig. 3.3b). However, there is significant temporal variability in the undercurrent, and the strongest modeled canyon upwelling events occur during mid-July when the undercurrent is relaxed. Time series of modeled temperature from Barkley and Quinault canyons also indicate that upwelling occurs during September (Figs. 3.7c, 3.9c). The vertical displacement

of isotherms is consistently related to the incident flow over the outer shelf throughout the summer. Since event-scale variability over the slope is largely driven by the same first-mode coastal trapped waves that affect the outer shelf, whether locally or remotely generated (Chapter 2), the undercurrent is often weak when shelf flow is equatorward. Therefore, the presence of event-scale variability means that canyon-enhanced upwelling of slope water from below the shelf break to the mid shelf does occur during late summer, the time of year when the undercurrent is usually present.

Table 3.1: Model-observation statistics for mooring time series of alongshore velocity (v) and density (σ_t). Correlations of detrended time series (CC_{DT}) significant at 95% confidence are shown in bold. Values of Willmot skill (WS) higher than that of NCOM-CCS (WS_{NCOM}) are shown in bold. Root-mean-squared error (RMSE), mean bias (MB), standard deviation error (SDE) and correlation coefficient error (CCE) are expressed in units of m s^{-1} for v, and units of kg m^{-3} for σ_t.

site	variable	depth	CC_{DT}	WS	WS_{NCOM}	RMSE	MB	SDE	CCE
E2	v	avg.	**0.78**	**0.83**	0.82	0.10	-0.05	-0.04	0.08
RN	v	avg.	**0.52**	0.69	0.81	0.08	-0.02	-0.02	0.07
E3	v	avg.	**0.46**	**0.72**	0.60	0.06	-0.01	-0.01	0.06
A1	v	35 m	0.24	**0.72**	0.36	0.11	-0.02	0.00	0.10
A1	v	300 m	0.25	0.63	0.82	0.05	-0.00	0.01	0.05
E2	σ_t	39 m	**0.85**	**0.95**	0.94	0.23	0.03	-0.10	0.21
E3	σ_t	120 m	0.00	**0.49**	0.45	0.25	-0.24	-0.04	0.08

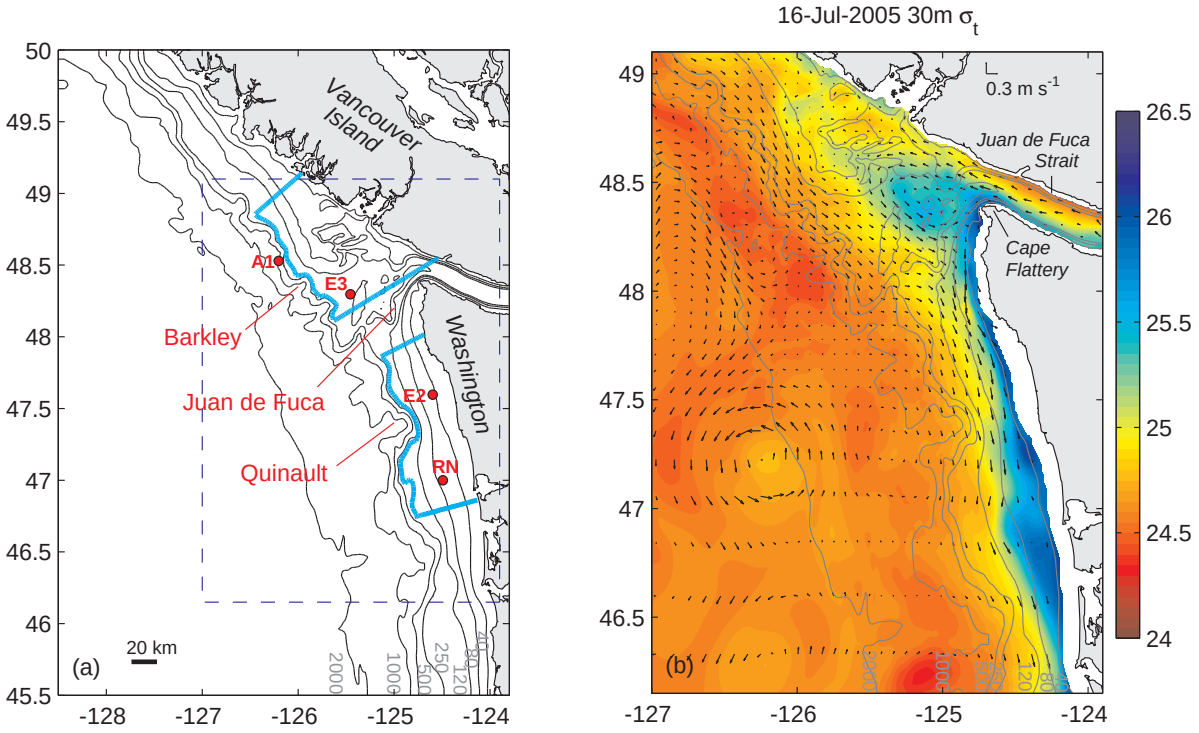

Figure 3.1: a) Model domain and bathymetry. Canyons that are the focus of this study and locations of mooring observations are labeled. Dashed lines delineate the subset of the domain used for analysis. Cyan contours outline volumes used for salt budgets in Section 3.4.3. b) Modeled density and velocity at 30-m depth on 16 July 2005. Arrows are shown for every sixth grid point.

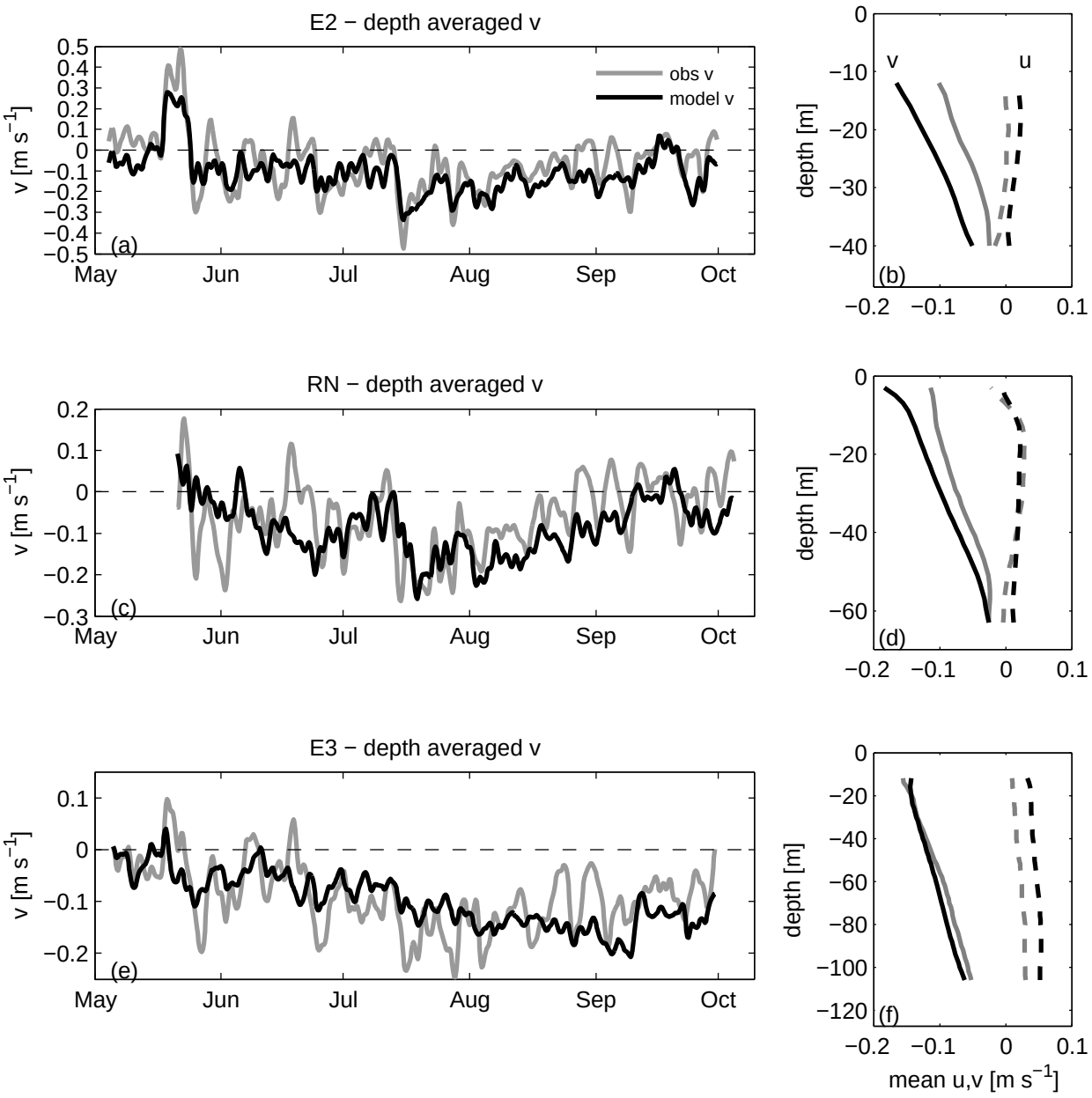

Figure 3.2: Modeled and observed depth-averaged velocity time series (a,c,e) and mean velocity profiles (b,d,f) at three mooring locations over the shelf. Note the difference in scale between the time series.

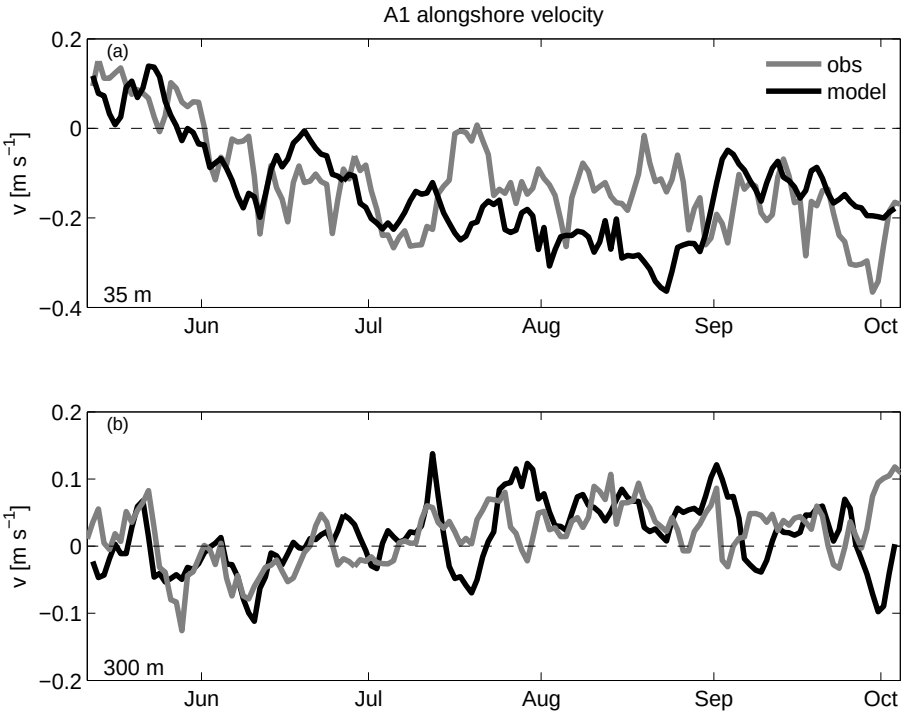

Figure 3.3: Modeled and observed velocity time series at the A1 mooring site over the British Columbia slope at depths a) 35 m, and b) 300 m. Note the difference in scale.

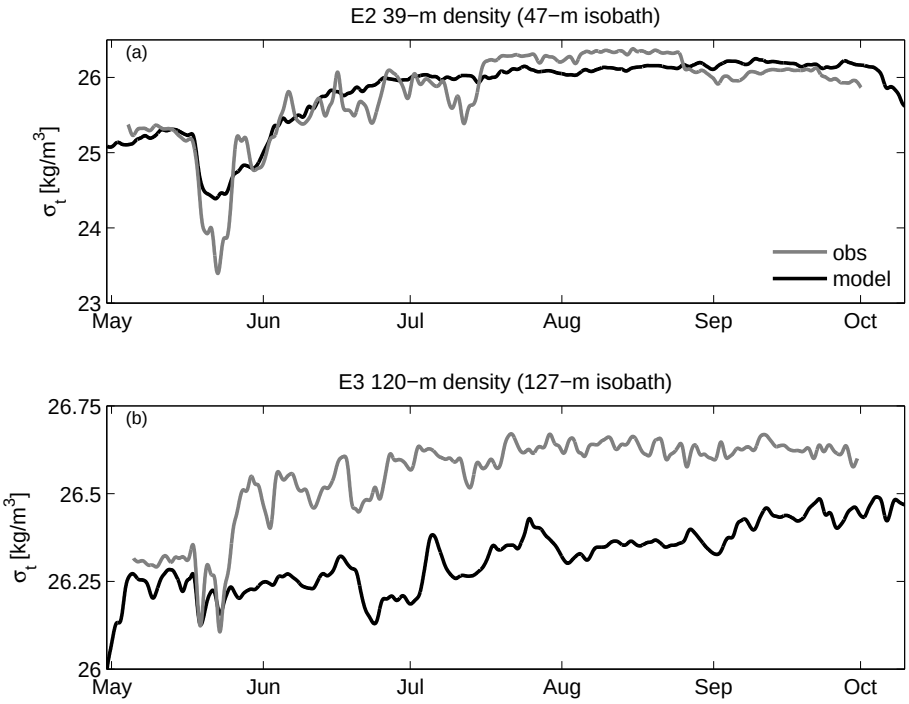

Figure 3.4: Modeled and observed near-bottom density time series at the a) E2 and b) E3 mooring sites. Note the difference in scale between the panels.

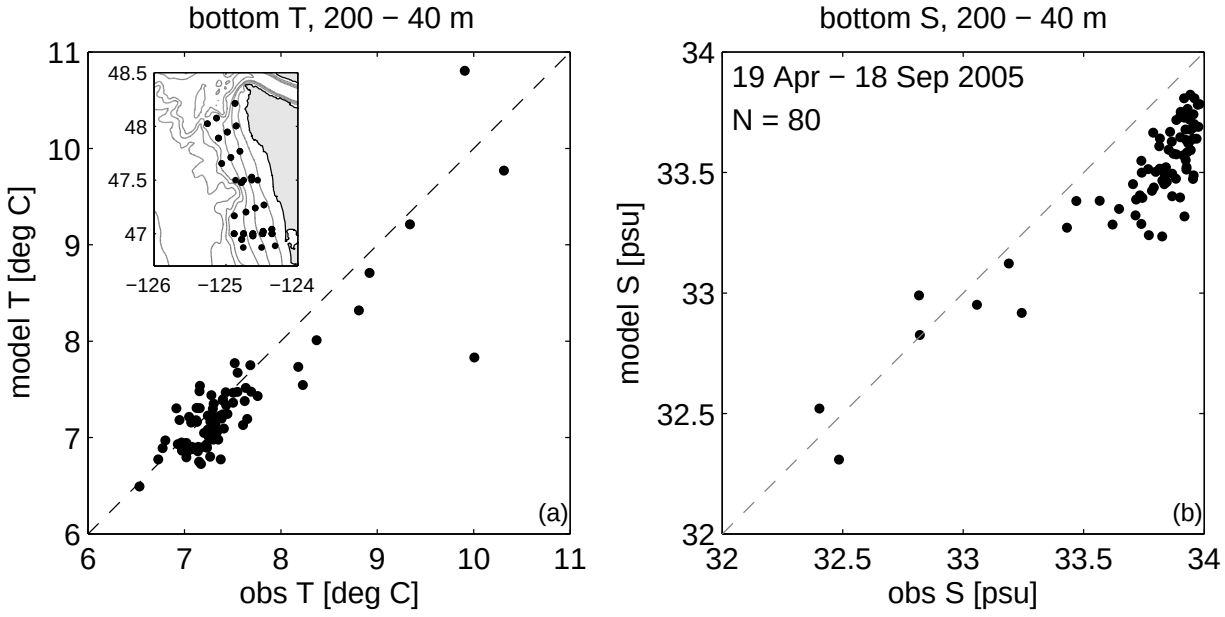

Figure 3.5: Comparisons of modeled and observed near-bottom temperature (a) and salinity (b) from shipboard surveys over the Washington shelf during 2005. Locations are shown in the inset in the upper left corner of panel a. Bottom depths include shallower than 40 m and deeper than 200 m are excluded in order to isolate the mid shelf–upper slope region. Measurements span the time period 19 April—18 September 2005.

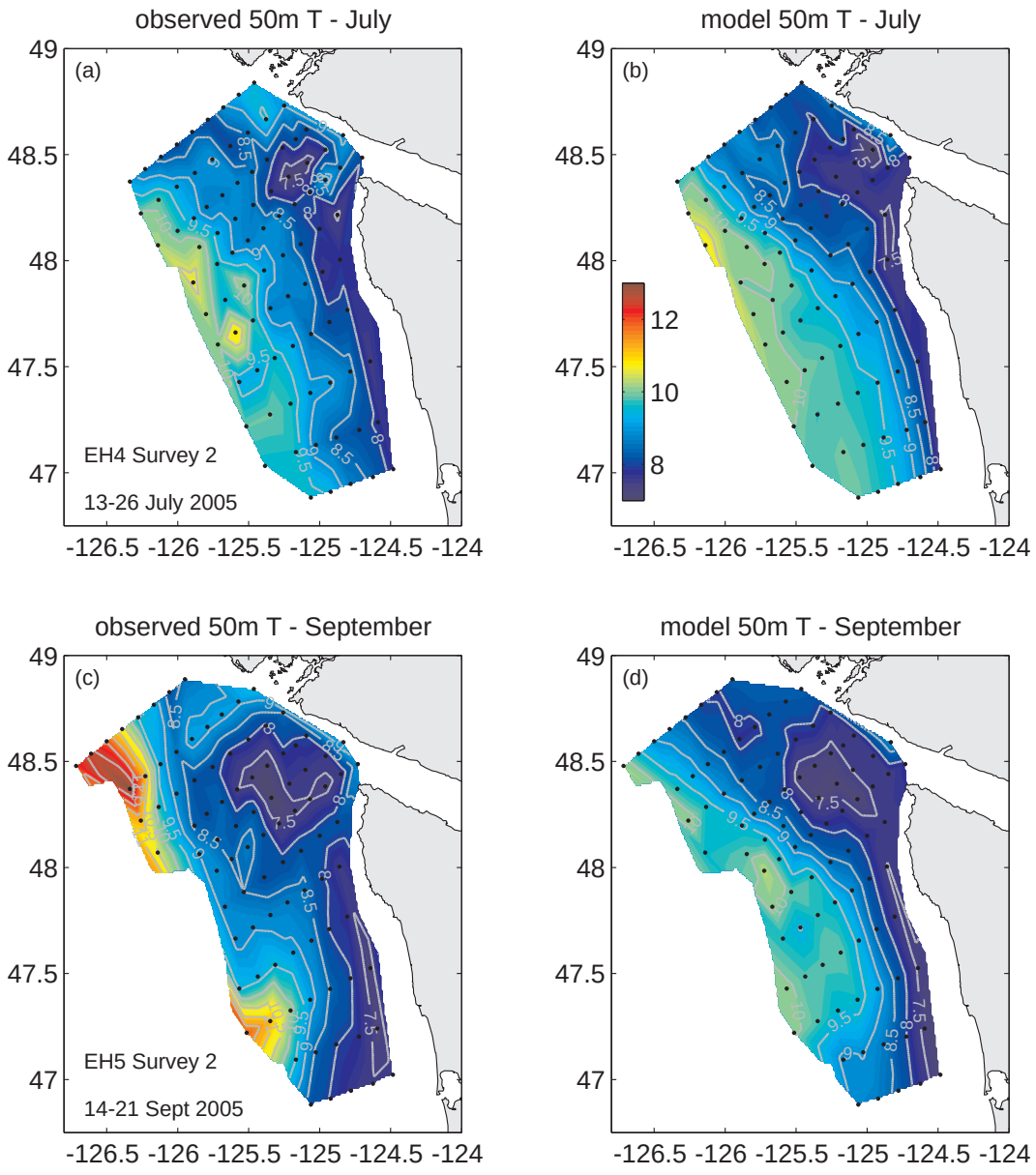

Figure 3.6: Maps of modeled and observed temperature at 50 m during July (a–b) and September (c–d) 2005. Model output is subsampled to the same locations and times as the observations.

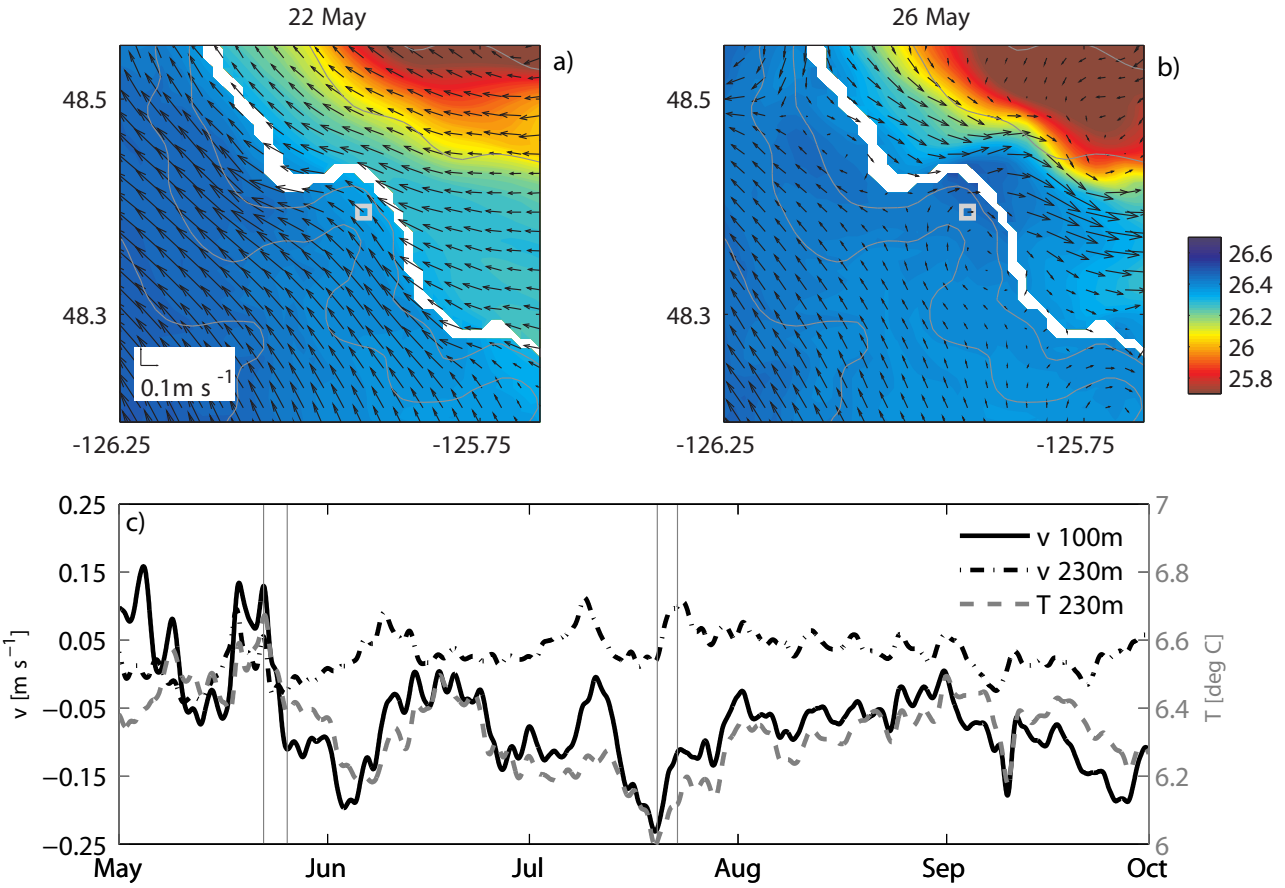

Figure 3.7: Modeled circulation near Barkley canyon. a) Velocity (arrows) and density (color) on 22 May 2005, in the bottom grid cell over the shelf and at 180 m further offshore. Every other velocity vector is shown. b) As in panel, but on 26 May. c) Time series of velocity and temperature at the location shown by the gray square in panels a and b. Alongshore velocity above rim depth at 100 m (solid black) and below rim depth at 230 m (dashed black), and temperature at 230 m (gray). Times of events shown in panels a and b, as well as Fig. 3.8, are shown as vertical gray lines.

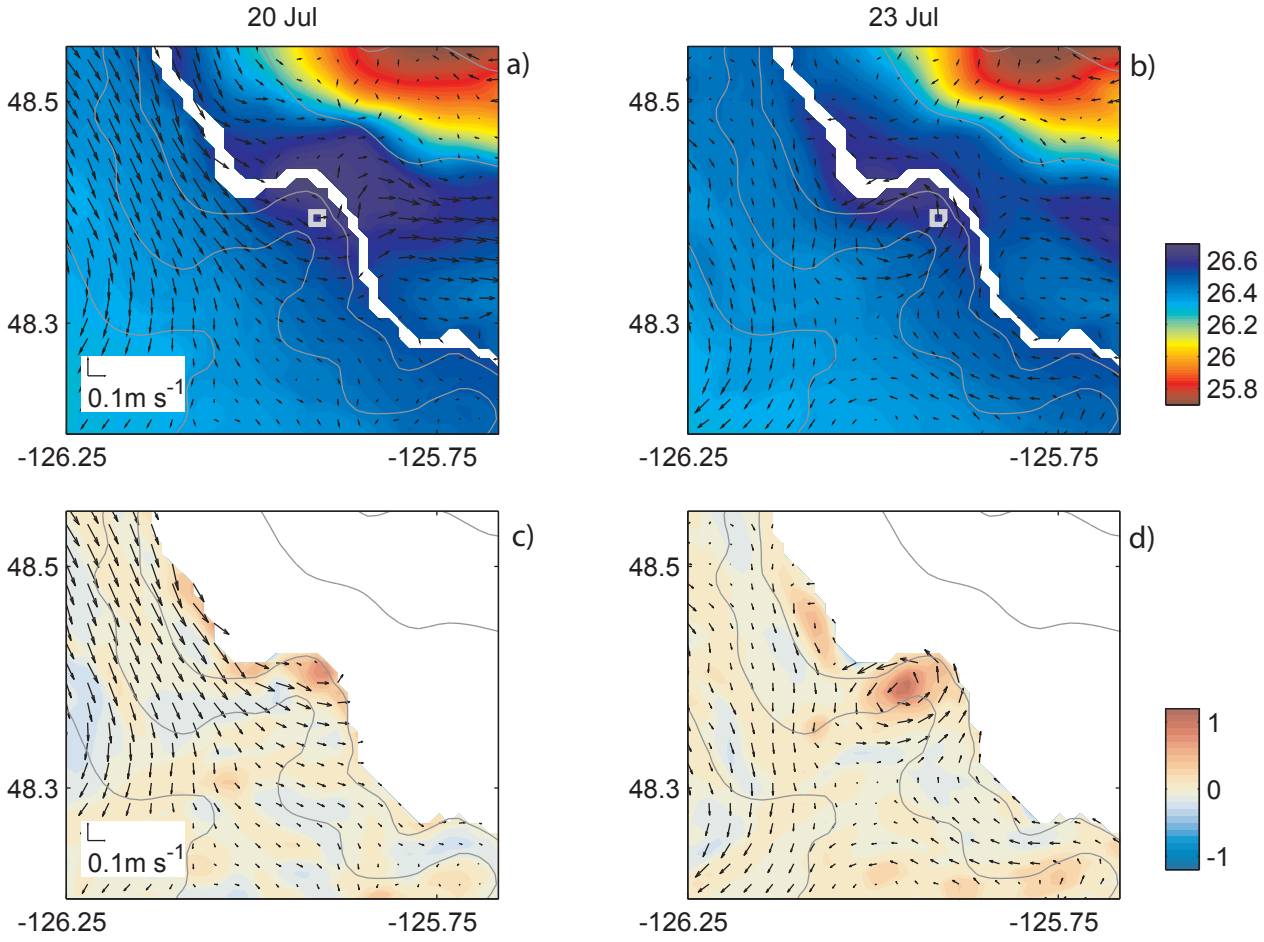

Figure 3.8: a) Velocity (arrows) and density (color) near Barkley canyon on 20 July 2005, in the bottom grid cell over the shelf and at 180 m further offshore. Every other velocity vector is shown. b) As in panel a, but on 23 July. c) Velocity (arrows) and relative vorticity (colors) at 180 m on 20 July. Vorticity is normalized by the Coriolis parameter f. d) As in panel c, for 23 July.

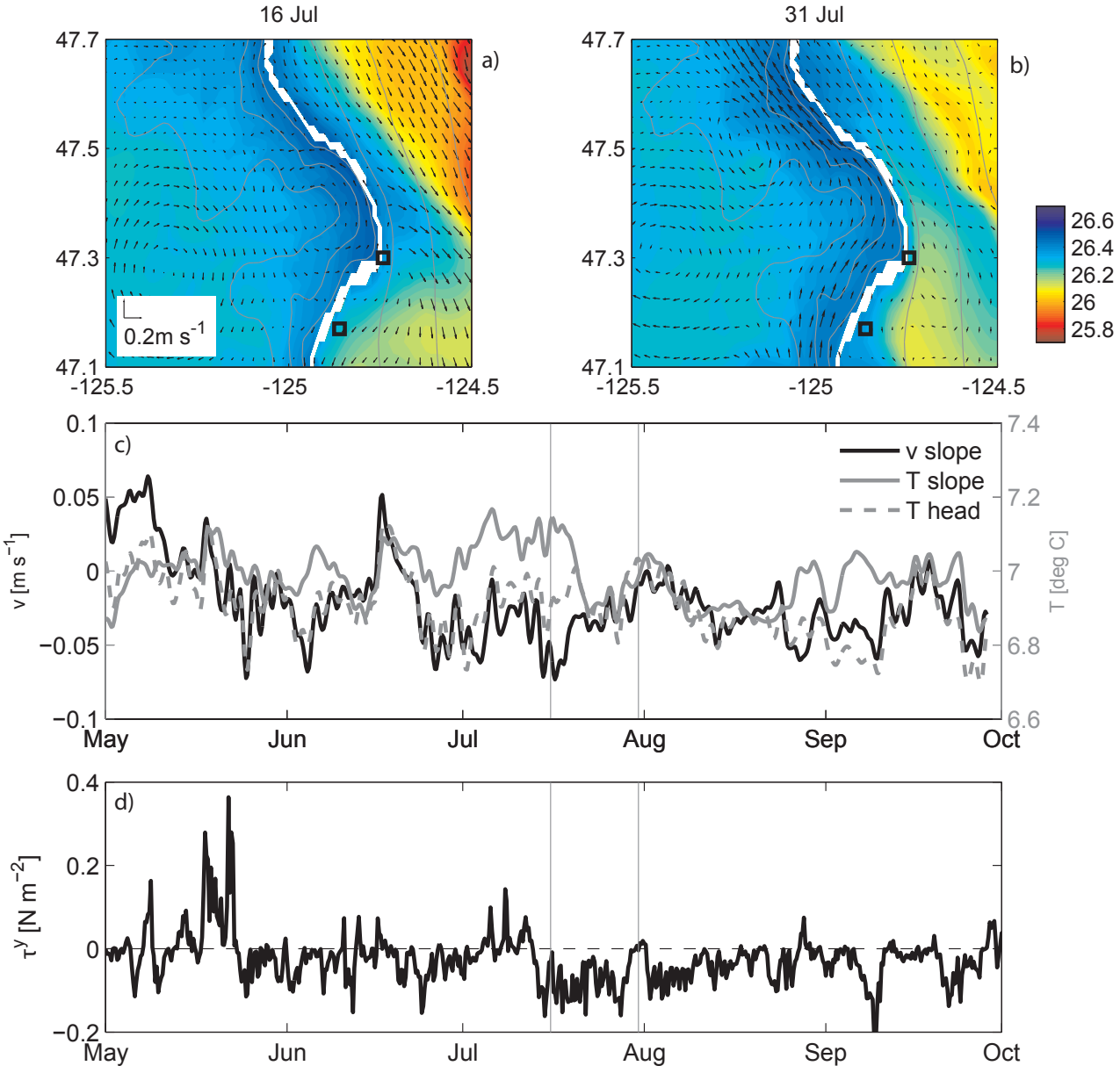

Figure 3.9: a) Velocity (arrows) and density (color) near Quinault canyon on 20 July 2005, in the bottom grid cell over the shelf and at 180 m further offshore. Every other velocity vector is shown. b) As in panel a, but for 31 July. c) Velocity and temperature over the 150-m isobath near Quinault canyon. Near-bottom alongshore velocity over the open slope (black), and near-bottom temperature over the open slope (solid gray) and near the head (dashed gray). Times of events shown in panels a and b are indicated by vertical gray lines. d) Alongshore wind stress from the model forcing over the Washington shelf.

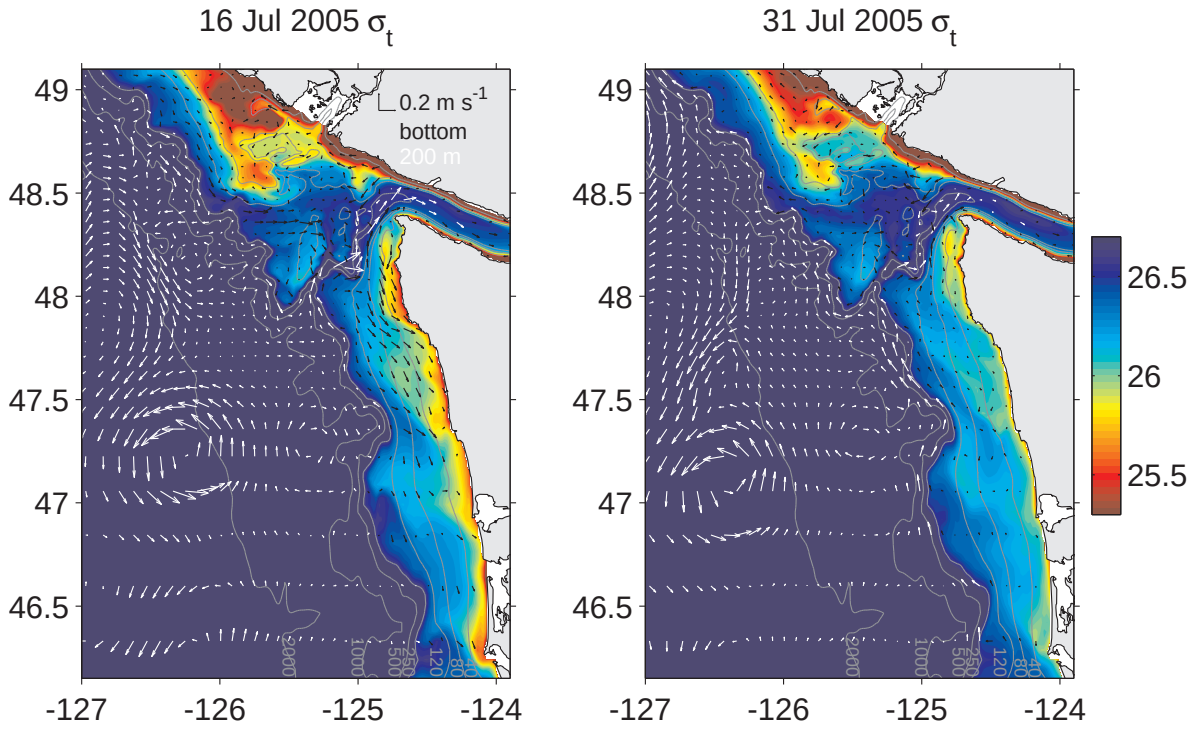

Figure 3.10: Modeled bottom density (colors), bottom velocity (black arrows) and 200-m velocity (white arrows) on 16 July (a) and 31 July 2005. Arrows are shown for every sixth grid point. Note that the range of the colorbar is narrower than the full range of bottom density.

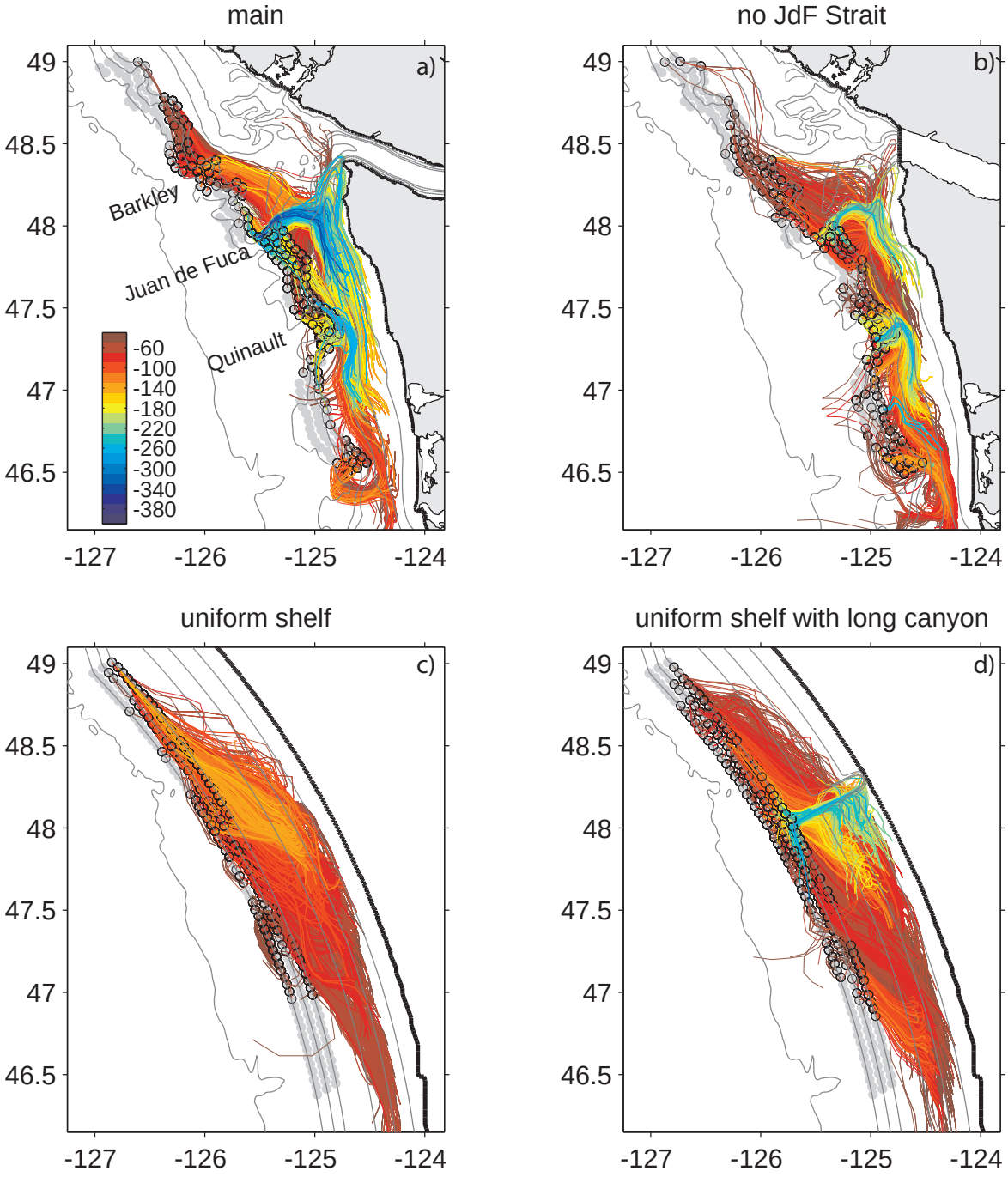

Figure 3.11: Trajectories of passive particles released during April–September over the slope (at locations indicated by gray circles) that pass within the 100-m isobath over the Washington shelf (46.25°N–48.1°N) within 15 days, colored by source depth at the starting point over the slope (black open circles). Trajectories with the deepest sources depth are plotted on top. a) main model run, b) no Strait of Juan de Fuca, c) uniform shelf, d) uniform shelf with long canyon.

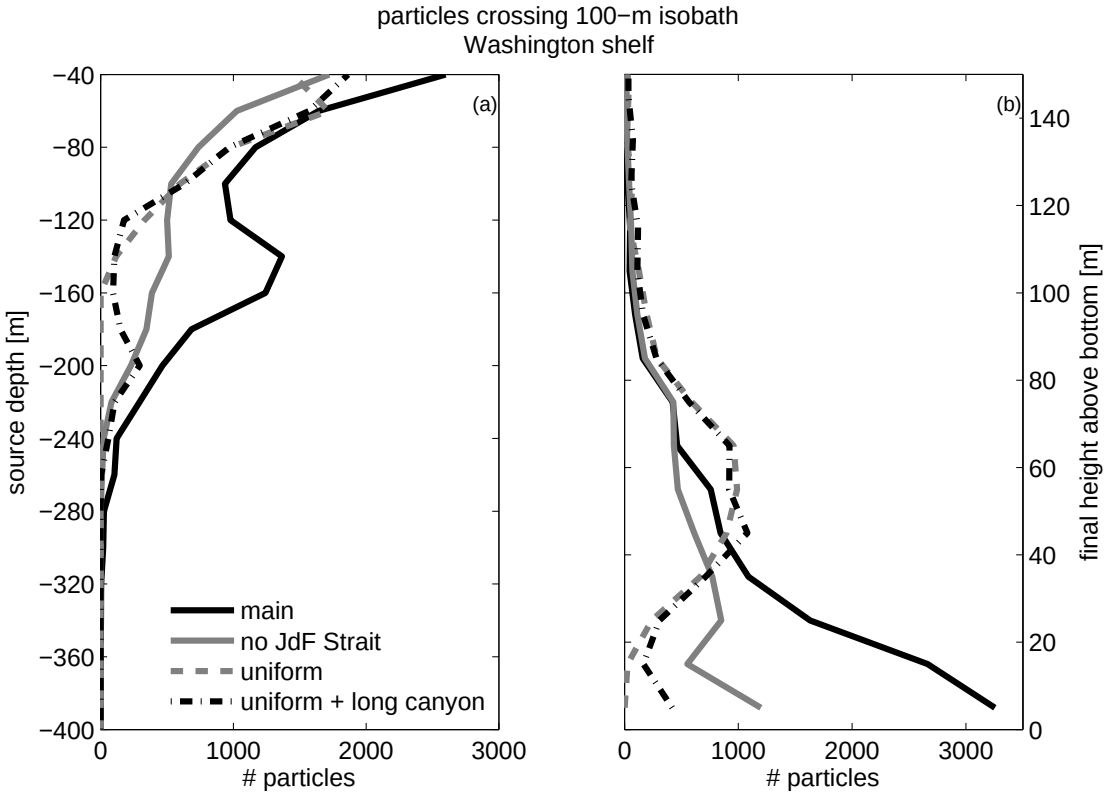

Figure 3.12: a) Histograms of source depths for trajectories shown in Fig. 3.11. Particles were released every 20 m between 40–400 m at locations over the slope. b) Histograms of the final height above bottom for the same particles, in 10-m bins.

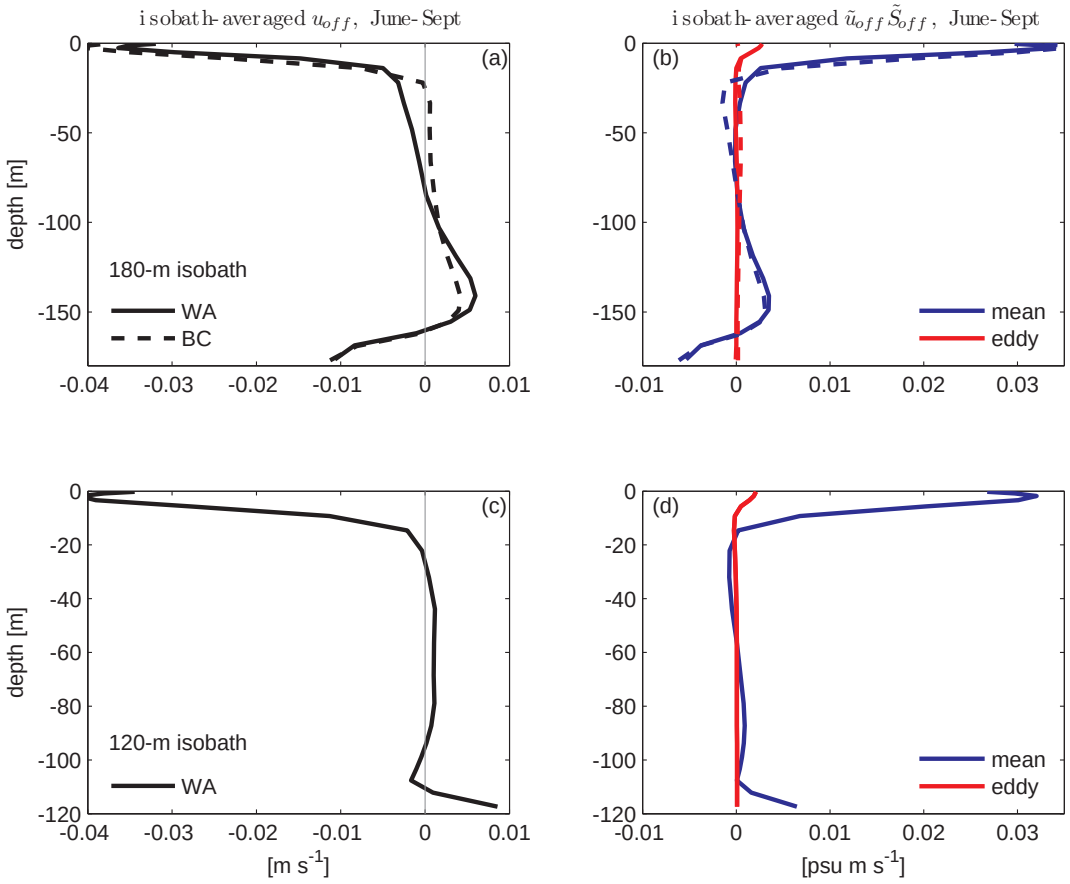

Figure 3.13: Mean profiles of cross-isobath velocity u_{off} and cross-isobath perturbation salt flux $\left(\widetilde{u}_{off}\widetilde{S}_{off}\right)$ during June–September. a) u_{off} averaged over the 180-m isobath off Washington (solid) and British Columbia (dashed). b) Perturbation salt flux averaged over the 180-m isobath off Washington (solid) and British Columbia (dashed): mean $\left(\bar{\widetilde{u}}\bar{\widetilde{S}}, \text{blue}\right)$ and eddy $\left(\overline{\widetilde{u}'\widetilde{S}'}, \text{red}\right)$ components. c–d) As in panels a–b, but for the 120-m isobath, and off the Washington shelf only.

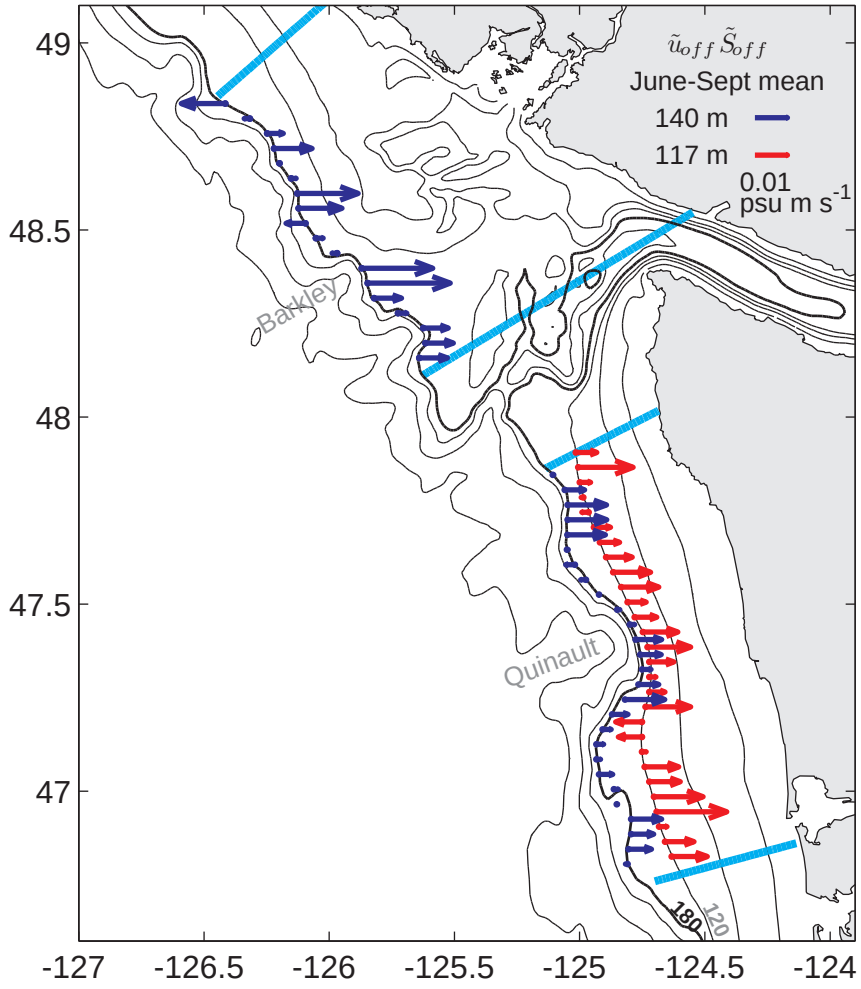

Figure 3.14: Mean horizontal distribution of the cross-isobath perturbation salt flux $\left(\widetilde{u}_{off}\widetilde{S}_{off}\right)$ during June–September at chosen depths above the bottom boundary layer. Blue: 140-m depth over the 180-m isobath. Red: 117-m depth (bottom grid cell) over the 120-m isobath off Washington. Northern and southern edges of the British Columbia and Washington control volumes are shown in light blue.

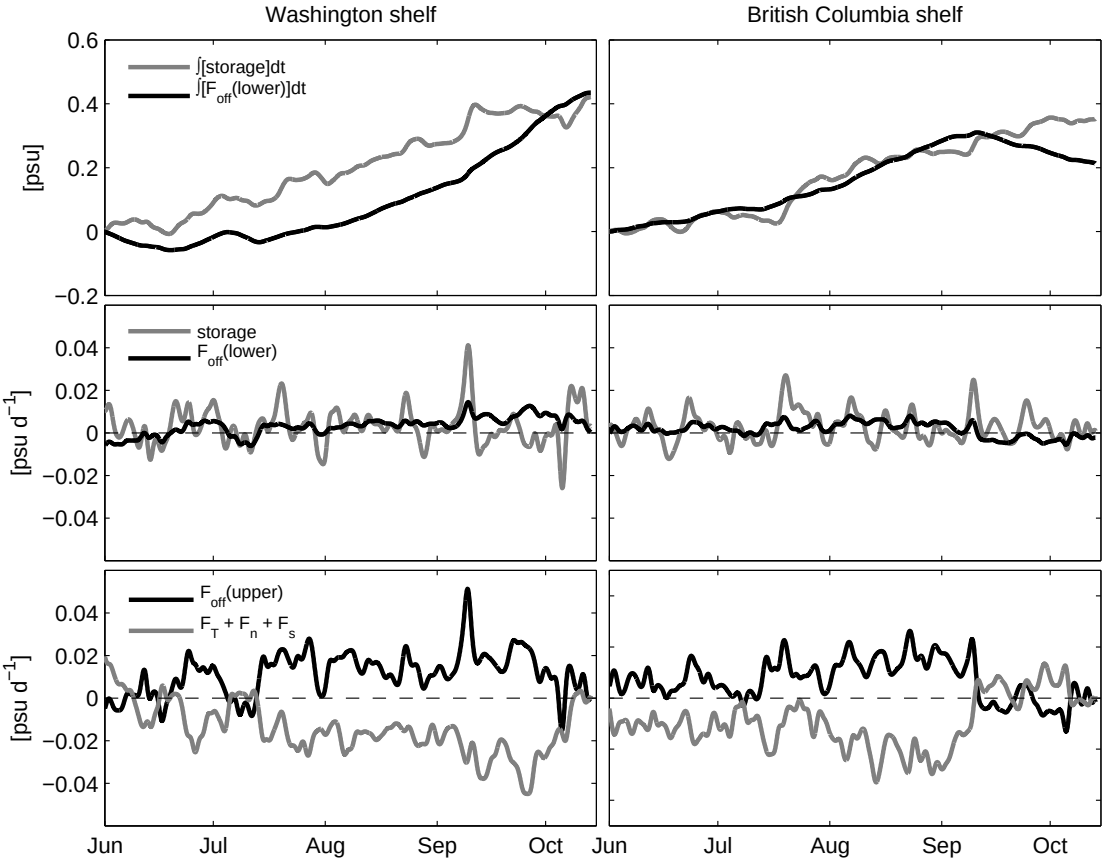

Figure 3.15: Time series of terms in the salt budget (3.9) for the Washington shelf (a,c,e) and British Columbia shelf (b,d,f). Locations of the volumes are shown in Fig. 3.1. All time series have been normalized by total volume. a–b) Cumulative change in salt (gray) and cumulative offshore salt flux across the 180-m isobath in the lower half of the water column (black). c–d) Salt storage, or rate of change in salt (grey), and offshore salt flux across the 180-m isobath in the lower half of the water column (black). e–f) Offshore salt flux across the 180-m isobath in the upper half of the water column (black) and the sum of the northern, southern and transport salt fluxes (grey).

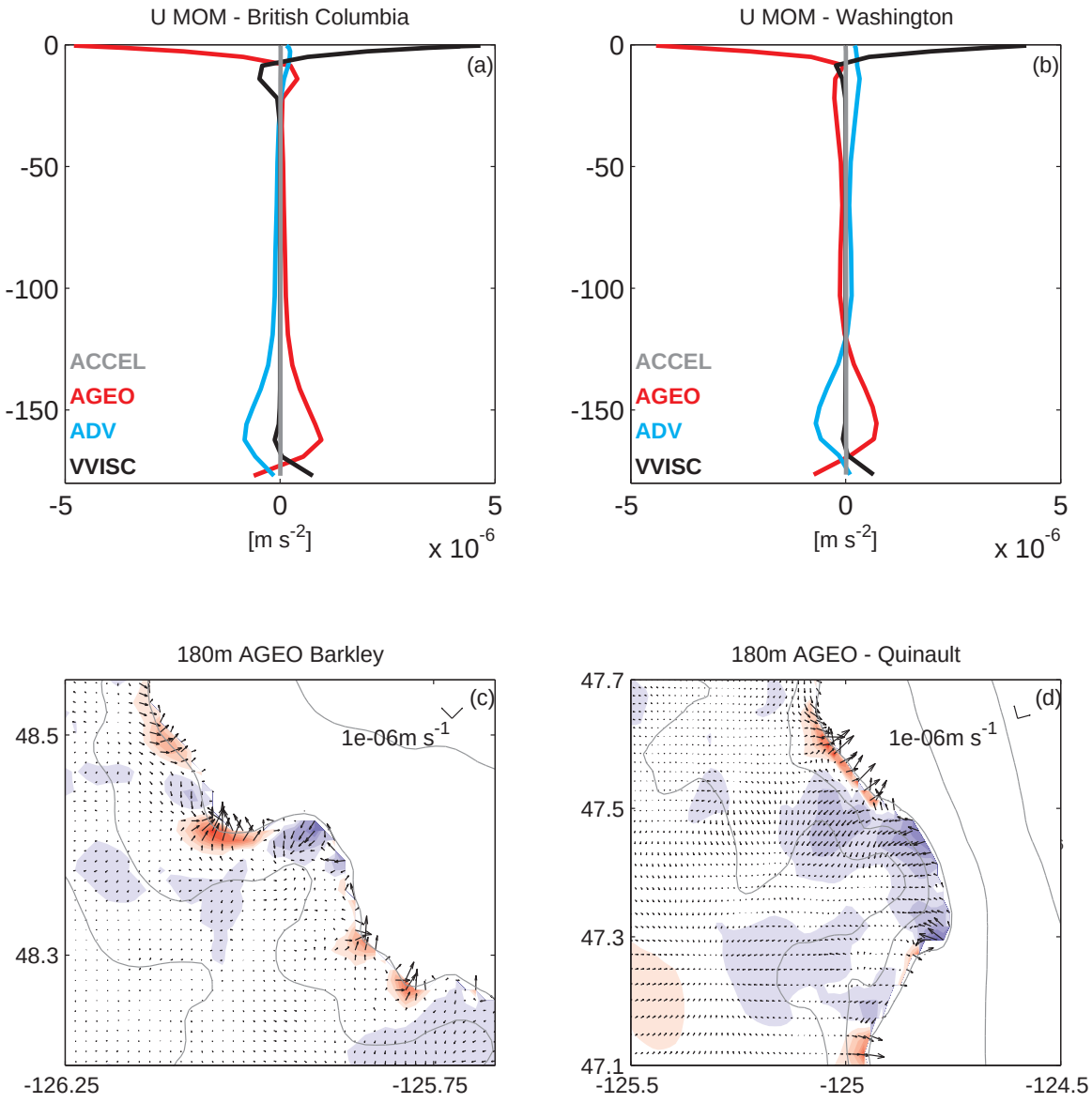

Figure 3.16: June–September mean of cross-shelf momentum balance terms. a) Average profiles of the cross-isobath components for the 180-m isobath on the offshore edge of the British Columbia shelf. b) As in panel a, but for the Washington shelf. c) Mean AGEO term at 180 m near Barkley canyon. Vectors indicate the direction and magnitude of the resultant force, and colors indicate the magnitude of the cross-shelf component in m s^{-2}. Along-shelf and cross-shelf directions are indicated by the scale bar in the upper right-hand corner. d) As in panel c, but for the area surrounding Quinault canyon.

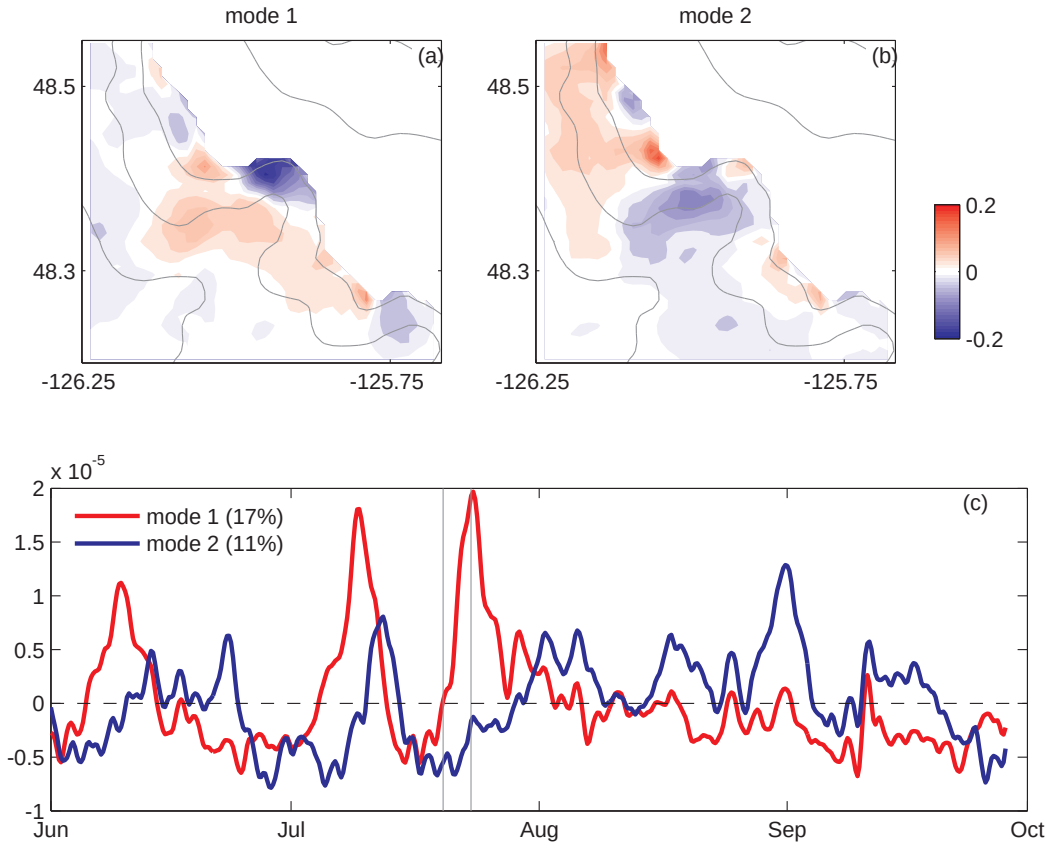

Figure 3.17: Cross-shelf momentum balance EOFs at 180 m near Barkley canyon: a) mode 1, b) mode 2. c) Amplitudes of mode 1 (red) and mode 2 (blue). Numbers in parentheses indicate the percentage of variance accounted for by each mode. Grey lines indicate 20 July and 23 July, the events shown in Fig. 3.8.

BIBLIOGRAPHY

Allen, J. S., P. A. Newberger, and J. Federiuk, 1995: Upwelling circulation on the Oregon continental shelf. Part I: Response to idealized forcing. *J. Phys. Oceanogr.*, **25**, 1843–1866.

Allen, S., C. Vindeirinho, R. Thomson, M. Foreman, and D. Mackas, 2001: Physical and biological processes over a submarine canyon during an upwelling event. *Can. J. Fish. Aquat. Sci.*, **58**, 671–684.

Allen, S. E., 1996: Topographically generated, subintertial flow within a finite length canyon. *J. Phys. Oceanogr.*, **26**, 1608–1632.

Allen, S. E., 2000: On subinertial flow in submarine canyons: Effect of geometry. *J. Geophys. Res.*, **105 (C1)**, 1285–1297.

Allen, S. E. and B. M. Hickey, 2010: Dynamics of advection-driven upwelling over a shelf break submarine canyon. *J. Geophys. Res.*, **115**, C08 018, doi:10.1029/2009JC005731.

Anderson, L. A., 1995: On the hydrogen and oxygen content of marine phytoplankton. *Deep Sea Res. I*, **42 (9)**, 1675–1680.

Archer, D. and A. Devol, 1992: Benthic oxygen fluxes on the Washington shelf and slope: A comparison of in situ microelectrode and chamber flux measurements. *Limnol. Oceanogr.*, **37**, 614–629.

Arntz, W. E., J. Tarazona, V. A. Gallardo, L. A. Flores, and H. S. Salzwedel, 1991: Benthos communities in oxygen deficient shelf and upper slope areas of the Peruvian and Chilean Pacific coast, and changes caused by El Niño. *Modern and Ancient Continental Shelf Anoxia*, R. V. Tyson and T. H. Pearson, Eds., The Geological Society, 131–154.

Atlas, R., R. N. Hoffman, J. Ardizzone, S. M. Leidner, J. C. Jusem, D. K. Smith, and D. Gombos, 2010: A cross-calibrated, multiplatform ocean surface wind velocity product

for meteorological and oceanographic applications. *Bull. Amer. Meteor. Soc.*, **92**, 157–174.

Bakun, A., 1973: Coastal upwelling indices, west coast of North America, 1946-71. Tech. Rep. NMFS SSRF-671, NOAA, 114 pp.

Bakun, A. and C. S. Nelson, 1991: The seasonal cycle of wind-stress curl in subtropical eastern boundary current regions. *J. Phys. Oceanogr.*, **21**, 1815–1834.

Bakun, A. and S. A. Weeks, 2004: Greenhouse gas buildup, sardines, submarine eruptions and the possibility of abrupt degradation of intense marine upwelling ecosystems. *Eco. Letts.*, **7**, 1015–1023.

Banas, N. S., E. V. Lessard, R. M. Kudela, P. MacCready, T. D. Peterson, B. M. Hickey, and E. Frame, 2009: Planktonic growth and grazing in the Columbia River plume region: A biophysical model study. *J. Geophys. Res.*, **114**, C00B06, doi:10.1029/2008JC004993.

Barber, R. T. and F. P. Chavez, 1983: Biological consequences of El Niño. *Science*, **222**, 1203–1210.

Barron, C. N., A. B. Kara, P. J. Martin, R. C. Rhodes, and L. F. Smedstad, 2006: Formulation, implementation and examination of vertical coordinate choices in the Global Navy Coastal Ocean Model (NCOM). *Ocean Modelling*, **11**, 347–375.

Barth, J. A., S. D. Pierce, and R. M. Castelao, 2005: Time-dependent, wind-driven flow over a shallow midshelf submarine bank. *J. Geophys. Res.*, **110**, C10S05.

Batteen, M. L., 1997: Wind-forced modeling studies of currents, meanders, and eddies in the California Current system. *J. Geophys. Res.*, **102**, 985–1010.

Battisti, D. S. and B. M. Hickey, 1984: Application of remote wind-forced coastal trapped wave theory to the Oregon and Washington coasts. *J. Phys. Oceanogr.*, **14**, 887–903.

Beckmann, A. and D. B. Haidvogel, 1993: Numerical simulation of flow around a tall isolated seamount. Part I: Problem formulation and model accuracy. *J. Phys. Oceanogr.*, **23**, 1736–1753.

Bianucci, L., K. L. Denman, and D. Ianson, 2011: Low oxygen and high inorganic carbon on the Vancouver Island Shelf. *J. Geophys. Res.*, **116**, C07011.

Bograd, S. J., C. G. Castro, E. D. Lorenzo, D. M. Palacios, H. Baily, W. Gilly, and F. P. Chavez, 2008: Oxygen declines and the shoaling of the hypoxic boundary in the California Current. *Geophys. Res. Letts.*, **35**, doi:10.1029/2008GL034185.

Bopp, L., C. Le Qur, M. Heimann, A. C. Manning, and P. Monfray, 2002: Climate-induced oceanic oxygen fluxes: Implications for the contemporary carbon budget. *Global Biogeochem. Cycles*, **16**, 1022, doi:10.1029/2001GB001445.

Botsford, L. W., D. A. Armstrong, and J. M. Shenker, 1989: Oceanographic influences on the dynamics of commercially fished populations. *Coastal oceanography of Washington and Oregon*, M. R. Landry and B. M. Hickey, Eds., Elsevier, 511–565.

Boyer, D. L., X. Zhang, and N. Pérenne, 2000: Laboratory observations of rotating, stratified flow in the vicinity of a submarine canyon. *Dyn. Atmos. Oceans*, **31**, 47–72.

Boyer, T. P., et al., 2006: *World Ocean Database 2005*. U.S. Government Printing Office, Washington, D.C., DVDs, 190 pp.

Brandes, J. A. and A. H. Devol, 1995: Simultaneous nitrate and oxygen respiration in coastal sediments: Evidence for discrete diagenesis. *J. Mar. Res.*, **53**, 771–797.

Brink, K. H., 1982: A comparison of long coastal trapped wave theory with observations off Peru. *J. Phys. Oceanogr.*, **12**, 897–913.

Brink, K. H., 1989: Energy conservation in coastal-trapped wave calculations. *J. Phys. Oceanogr.*, **19**, 1011–1016.

Brink, K. H., 1991: Coastal-trapped waves and wind-driven currents over the continental shelf. *Annu. Rev. Fluid Mech.*, **23**, 389–412.

Brink, K. H., 1998: Deep-sea forcing and exchange processes. *The Sea*, K. H. Brink and A. R. Robinson, Eds., John Wiley and Sons, Inc., Vol. 11, 151–167.

Brink, K. H. and D. C. Chapman, 1987: Programs for computing properties of coastal-trapped waves and wind-driven motions over the continental shelf and slope - Second Edition. Tech. Rep. WHOI-87-24, Woods Hole Oceanographic Institution.

Broecker, W., 1974: "NO" a conservative water-mass tracer. *Earth and Planetary Science Letters*, **23**, 100–107.

Brüchert, V., et al., 2006: Biogeochemical and physical control on shelf anoxia and water column hydrogen sulphide in the Benguela coastal upwelling system off Namibia. *Past and Present Water Column Anoxia*, L. N. Neretin, Ed., Springer, 161–193.

Bruland, K. W., M. C. Lohan, A. M. Aguilar-Islas, G. J. Smith, B. Sohst, and A. Baptista, 2008: Factors influencing the chemistry of the near-field Columbia River plume: Nitrate, silicic acid, dissolved Fe, and dissolved Mn. *J. Geophys. Res.*, **113**, C00B02.

Cannon, G. A., 1972: Wind effects on currents observed in Juan de Fuca submarine canyon. *J. Phys. Oceanogr.*, **2**, 281–285.

Canuto, V. M., A. Howard, Y. Cheng, and M. S. Dubovikov, 2001: Ocean turbulence. Part I: One-point closure model—Momentum and heat vertical diffusivities. *J. Phys. Oceanogr.*, **31**, 1413–1426.

Carpenter, J. H., 1965a: The accuracy of the Winkler method for dissolved oxygen. *Limnol. Oceanogr.*, **10**, 135–140.

Carpenter, J. H., 1965b: The Chesapeake Bay Institute technique for the Winkler dissolved oxygen method. *Limnol. Oceanogr.*, **10**, 141–143.

Carritt, D. E. and J. H. Carpenter, 1966: Comparison and evaluation of currently employed modifications of the Winkler method for determining dissolved oxygen in seawater; a NASCO report. *J. Mar. Res.*, **24**, 286–318.

Castelao, R. M. and J. A. Barth, 2005: Coastal ocean response to summer upwelling favorable winds in a region of alongshore bottom topography variations off Oregon. *J. Geophys. Res.*, **110**, C10S04.

Castro, C. G., F. P. Chavez, and C. A. Collins, 2001: Role of the California Undercurrent in the export of denitrified waters from the eastern tropical North Pacific. *Global Biogeochemical Cycles*, **15**, 819–830.

Chan, F., J. A. Barth, J. Lubchenco, A. Kirincich, H. Weeks, W. T. Peterson, and B. A. Menge, 2008: Emergence of anoxia in the California Current large marine ecosystem. *Science*, **319**, 920.

Chapman, D. C., 1985: Numerical treatment of cross-shelf open boundaries in a barotropic coastal ocean model. *J. Phys. Oceanogr.*, **15**, 1060–1075.

Chapman, D. C., 1987: Application of wind-forced, long, coastal-trapped wave theory along the California coast. *J. Geophys. Res.*, **92(C2)**, 1798–1816.

Clarke, A. J. and C. Shi, 1991: Critical frequencies at ocean boundaries. *J. Geophys. Res.*, **96**, 10,731–10,738.

Clarke, A. J. and S. Van Gorder, 1986: A method for estimating wind-driven frictional, time-dependent, stratified shelf and slope water flow. *J. Phys. Oceanogr.*, **16**, 1013–1028.

Codispoti, L. A., J. A. Brandes, J. P. Christensen, A. H. Devol, S. W. A. Naqvi, H. W. Paerl, and T. Yoshinari, 2001: The oceanic fixed nitrogen and nitrous oxide budgets: Moving targets as we enter the anthropocene? *Sci. Mar.*, **65 (Supl. 2)**, 85–105.

Codispoti, L. A., T. Yoshinari, and A. H. Devol, 2005: Suboxic respiration in the oceanic water column. *Respiration In Aquatic Ecosystems*, P. A. del Giorgio and P. J. l. B. Williams, Eds., Oxford University Press, 225–247.

Collins, C. A., L. M. Ivanov, and O. V. Mel'nichenko, 2003: Seasonal variability of the California Undercurrent: Statistical analysis based on the trajectories of floats with neutral buoyancy. *Phys. Oceanogr.*, **13**, 135–147.

Connolly, T. P., B. M. Hickey, S. L. Geier, and W. P. Cochlan, 2010: Processes influencing seasonal hypoxia in the northern California Current System. *J. Geophys. Res.*, **115**, C03021, doi:10.1029/2009JC005283.

Csanady, G., 1978: The arrested topographic wave. *J. Phys. Oceanogr.*, **8**, 47–62.

Csanady, G. T., 1985: "Pycnobathic" currents over the upper continental slope. *J. Phys. Oceanogr.*, **15**, 306–315.

Davis, J. C., 1975: Minimal dissolved oxygen requirements of aquatic life with emphasis on Canadian species: a review. *J. Fish. Res. Board Can.*, **32**, 2295–2332.

Deutsch, C., H. Brix, T. Ito, H. Frenzel, and L. Thompson, 2011: Climate-forced variability of ocean hypoxia. *Science*, **333**, 336–339.

Deutsch, C., S. Emerson, and L. Thompson, 2006: Physical-biological interactions in North Pacific oxygen variability. *J. Geophys. Res.*, **111**, C09S90.

Devol, A. H. and J. P. Christensen, 1993: Benthic fluxes and nitrogen cycling in sediments of the continental margin of the eastern North Pacific. *J. Mar. Res.*, **51**, 345–372.

Diaz, R. J. and J. Rosenberg, 1995: Marine benthic hypoxia: a review of its ecological effects and the behavioural responses of benthic macrofauna. *Oceanography and Marine Biology: an Annual Review*, **33**, 245–303.

Divins, D. L. and D. Metzger, 2008: Integrated models of coastal relief. Tech. rep., Natl. Geophys. Data Cent., http://www.ngdc.noaa.gov/mgg/coastal/coastal.html.

Ekman, V. W., 1905: On the influence of the earth's rotation on ocean currents. *Ark. Mat. Aston. Fys.*, **2 (11)**, 1–53.

Emerson, S., Y. Watanabe, T. Ono, and S. Mecking, 2004: Temporal trends in apparent oxygen utilization in the upper pycnocline of the North Pacific: 1980–2000. *J. Oceanogr.*, **60**, 139–147.

Emery, W. J. and R. E. Thomson, 2004: *Data analysis methods in physical oceanography.* 2d ed., Elsevier Science B. V., Amsterdam, The Netherlands, 638 pp.

Fairall, C. W., E. F. Bradley, J. E. Hare, A. A. Grachev, and J. B. Edson, 2003: Bulk parameterization of air-sea fluxes: Updates and verification for the COARE algorithm. *J. Climate*, **16**, 571–591.

Federiuk, J. and J. S. Allen, 1995: Upwelling circulation on the Oregon continental shelf. Part II: Simulations and comparisons with observations. *J. Phys. Oceanogr.*, **25**, 1867–1889.

Flather, R. A., 1976: A tidal model of the northwest European continental shelf. *Mem. Soc. Roy. Sci. Liege*, **10**, 141–164.

Foreman, M. G. G., W. Callendar, A. MacFadyen, B. M. Hickey, R. E. Thomson, and E. Di Lorenzo, 2008: Modeling the generation of the Juan de Fuca Eddy. *J. Geophys. Res.*, **113**, C03 006, doi:10.1029/2006JC004 082.

Foreman, M. G. G., W. R. Crawford, J. Y. Cherniawsky, R. F. Henry, and M. R. Tarbotton, 2000: A high-resolution assimilating tidal model for the northeast Pacific Ocean. *J. Geophys. Res.*, **105 (C12)**, 28 629–28 651.

Freeland, H. J. and K. L. Denman, 1982: A topographically controlled upwelling centre off southern Vancouver Island. *J. Mar. Res.*, **40**, 1069–1093.

Frölicher, T. L., F. Joos, G.-K. Plattner, M. Steinacher, and S. C. Doney, 2009: Natural variability and anthropogenic trends in oceanic oxygen in a coupled carbon cycle–climate model ensemble. *Global Biogeochem. Cycles*, **23**, GB1003.

Garfield, N., C. A. Collins, R. G. Paquette, and E. Carter, 1999: Lagrangian exploration of the California Undercurrent, 1992–95. *J. Phys. Oceanogr.*, **29**, 560–583.

Grantham, B. A., F. Chan, K. J. Nielsen, D. Fox, J. A. Barth, A. Huyer, J. Lubchenco, and B. A. Menge, 2004: Upwelling-driven nearshore hypoxia signals ecosystem and oceanographic changes in the northeast Pacific. *Nature*, **429**, 749–754.

Gray, J. S., R. S. Wu, and Y. Y. Or, 2002: Effects of hypoxia and organic enrichment on the marine environment. *Mar. Ecol. Prog. Ser.*, **238**, 249–279.

Gruber, N. and J. L. Sarmiento, 1997: Global patterns of marine nitrogen fixation and denitrification. *Global Biogeochem Cycles*, **11**, 235–266.

Haidvogel, D. B. and K. H. Brink, 1986: Mean currents driven by topographic drag over the continental shelf and slope. *J. Phys. Oceanogr.*, **16**, 2159–2171.

Hales, B., L. Karp-Boss, A. Perlin, and P. A. Wheeler, 2006: Oxygen production and carbon sequestration in an upwelling coastal margin. *Global Biogeochemical Cycles*, **20**, doi:10.1029/2005GB002 517.

Haney, R. L., 1991: On the pressure gradient force over steep topography in sigma coordinate ocean models. *J. Phys. Oceanogr.*, **21**, 610–619.

Hartnett, H. E. and A. H. Devol, 2003: Role of a strong oxygen-deficient zone in the preservation and degradation of organic matter: A carbon budget for the continental margins of northwest Mexico and Washington State. *Geochim. Cosmochim. Acta*, **67**, 247–264.

Haugerud, R. A., 2000: Digital elevation model (DEM) of Cascadia, latitude 39N–53N, longitude 116W–133W. Open File Rep. 99-369, U. S. Geol. Surv., Menlo Park, Calif.

Hetland, R. D. and S. F. DiMarco, 2008: How does the character of oxygen demand control the structure of hypoxia on the Texas–Louisiana continental shelf? *J. Mar. Syst.*, **70**, 49–62.

Hickey, B., S. Geier, N. Kachel, and A. MacFadyen, 2005: A bi-directional river plume: The Columbia in summer. *Cont. Shelf Res.*, **25**, 1631–1656.

Hickey, B., A. MacFadyen, W. Cochlan, R. Kudela, K. Bruland, and C. Trick, 2006: Evolution of chemical, biological, and physical water properties in the northern California Current in 2005: Remote or local wind forcing? *Geophys. Res. Lett.*, **33**, L22S02, doi: 10.1029/2006GL026782.

Hickey, B. M., 1979: The California current system - hypotheses and facts. *Prog. Oceanogr.*, **8**, 191–279.

Hickey, B. M., 1989: Patterns and processes of circulation over the Washington continental

shelf and slope. *Coastal oceanography of Washington and Oregon*, M. R. Landry and B. M. Hickey, Eds., Elsevier, 41–115.

Hickey, B. M., 1997: The response of a steep-sided, narrow canyon to time-variable wind forcing. *J. Phys. Oceanogr.*, **27**, 697–726.

Hickey, B. M., 1998: Coastal oceanography of western North America from the tip of Baja California to Vancouver Island. *The Sea*, A. R. Robinson and K. H. Brink, Eds., John Wiley and Sons, Inc., Vol. 11, 345–393.

Hickey, B. M. and N. S. Banas, 2008: Why is the northern end of the California Current System so productive? *Oceanography*, **21 (4)**, 90–107.

Hickey, B. M. and N. E. Pola, 1983: The seasonal alongshore pressure gradient on the west coast of the United States. *J. Geophys. Res.*, **88**, 7623–7633.

Hickey, B. M., et al., 2010: River Influences on Shelf Ecosystems: Introduction and synthesis. *J. Geophys. Res.*, **115**, C00B17, doi:10.1029/2009JC005452.

Hill, A. E., B. M. Hickey, F. A. Shillington, P. T. Strub, K. H. Brink, E. D. Barton, and A. C. Thomas, 1998: Eastern ocean boundaries. *The Sea*, A. R. Robinson and K. H. Brink, Eds., John Wiley and Sons, Inc., Vol. 11, 29–67.

Hill, J. K. and P. A. Wheeler, 2002: Organic carbon and nitrogen in the northern California current system: comparison of offshore, river plume, and coastally upwelled waters. *Prog. Oceanogr.*, **53**, 369–387.

Hodur, R. M., 1997: The Naval Research Laboratory's Coupled Ocean/Atmosphere Mesoscale Prediction System (COAMPS). *Mon. Wea. Rev.*, **125**, 1414–1430.

Hurlburt, H. E. and J. D. Thompson, 1973: Coastal upwelling on a β-plane. *J. Phys. Oceanogr.*, **3**, 16–32.

Huthnance, J. M., 1984: Slope currents and JEBAR. *J. Phys. Oceanogr.*, **14**, 795–810.

Huyer, A., 1983: Coastal upwelling in the California current system. *Prog. Oceanogr.*, **12**, 259–284.

Huyer, A., J. A. Barth., P. M. Kosro, R. K. Shearman, and R. L. Smith, 1998: Upper-ocean water mass characteristics of the California Current, Summer 1993. *Deep-Sea Res. II*, **45**, 1411–1442.

Jordi, A., G. Basterretxea, A. Orfila, and J. Tintoré, 2006: Analysis of the circulation and shelf-slope exchanges in the continental margin of the northwestern Mediterranean. *Ocean Sci.*, **2**, 173–181.

Jumars, P. A. and K. Banse, 1989: Benthos and its interaction with bottom boundary layer processes. *Coastal oceanography of Washington and Oregon*, M. R. Landry and B. M. Hickey, Eds., Elsevier, 349–365.

Kämpf, J., 2009: On the interaction of time-variable flows with a shelfbreak canyon. *J. Phys. Oceanogr.*, **39**, 248–260.

Kämpf, J., 2010: On preconditioning of coastal upwelling in the eastern Great Australian Bight. *J. Geophys. Res.*, **115**, C12 071, doi:10.1029/2010JC006294.

Kara, A. B., C. N. Barron, M. P. J., L. F. Smedstad, and R. C. Rhoades, 2006: Validation of interannual simulations from the 1/8 degree global Navy Coastal Ocean Model (NCOM). *Ocean Modelling*, **11**, 376–398.

Karstensen, J., L. Stramma, and M. Visbeck, 2008: Oxygen minimum zones in the eastern tropical atlantic and pacific oceans. *Prog. Oceanogr.*, **77**, 331–350.

Kelly, K. A., M. J. Caruso, and J. A. Austin, 1993: Wind-forced variations in sea surface height in the northeast Pacific Ocean. *J. Phys. Oceanogr.*, **23**, 2392–2411.

Kirincich, A. R., J. A. Barth, B. A. Grantham, B. A. Menge, and J. Lubchenco, 2005: Wind-driven inner-shelf circulation off central Oregon during summer. *J. Geophys. Res.*, **110**, doi:10.1029/2004JC002 611.

Klinck, J. M., 1996: Circulation near submarine canyons: A modeling study. *J. Geophys. Res.*, **101 (C1)**, 1211–1223.

Knepel, K. and K. Bogren, 2002: Determination of orthophosphate by flow injection analysis. QuikChem® Method 31-115-01-1-H, Lachat Instruments, 14 pp., Milwaukee, WI.

Kosro, P. M., W. T. Peterson, B. M. Hickey, R. K. Shearman, and S. D. Pierce, 2006: Physical versus biological spring transition: 2005. *Geophys. Res. Letts.*, **33**, L22S03, doi:10.1029/2006GL027 072.

Landry, M. R., J. R. Postel, W. K. Peterson, and J. Newman, 1989: Broad-scale distributional patterns of hydrographic variables on the Washington shelf. *Coastal oceanography of Washington and Oregon*, M. R. Landry and B. M. Hickey, Eds., Elsevier, 1–40.

Large, W. G. and S. Pond, 1981: Open ocean momentum flux measurements in moderate to strong winds. *J. Phys. Oceanogr.*, **11**, 324–336.

Lathuilière, C., V. Echevin, M. Lévy, and G. Madec, 2010: On the role of the mesoscale circulation on an idealized coastal upwelling system. *J. Geophys. Res.*, **115**, C09018, doi:10.1029/2009JC005827.

Lentz, S. J., 1987: A heat budget for the northern California shelf during CODE 2. *J. Geophys. Res.*, **92 (C13)**, 14 491–14 509.

Lentz, S. J., 1995: Sensitivity of the inner-shelf circulation to the form of the eddy viscosity profile. *J. Phys. Oceanogr.*, **25**, 19–28.

Lessard, E. J. and E. R. Frame, 2008: The influence of the Columbia River plume on patterns of phytoplankton growth, grazing and chlorophyll on the Washington and Oregon coasts. *Ocean Sciences Meeting Abstracts*, ASLO/AGU, 234.

Liu, K. K. and I. R. Kaplan, 1989: The eastern tropical Pacific as a source of ^{15}N-enriched nitrate in seawater off southern California. *Limnol. Oceanogr.*, **34**, 820–830.

Liu, Y., P. MacCready, B. M. Hickey, E. P. Dever, P. M. Kosro, and N. S. Banas, 2009: Evaluation of a coastal ocean circulation model for the Columbia River plume in summer 2004. *J. Geophys. Res.*, **114**, C00B04, doi:10.1029/2008JC004929.

Lohan, M. C. and K. W. Bruland, 2008: Elevated Fe(II) and dissolved Fe in hypoxic shelf waters off Oregon and Washington: an enhanced source of iron to coastal upwelling regimes. *Environ. Sci. Technol.*, **42**, 6462–6468.

Lynn, R. L. and J. J. Simpson, 1987: The California Current system: the seasonal variability of its physical characteristics. *J. Geophys. Res.*, **92**, 12 947–12 966.

MacFadyen, A. and B. M. Hickey, 2010: Generation and evolution of a topographically linked, mesoscale eddy under steady and variable wind-forcing. *Cont. Shelf Res.*, **30**, 1387–1402.

MacFadyen, A., B. M. Hickey, and W. Cochlan, 2008: Influences of the Juan de Fuca Eddy on circulation, nutrients, and phytoplankton production in the northern California Current System. *J. Geophys. Res.*, **113**, C08008, doi:10.1029/2007JC004412.

MacFadyen, A., B. M. Hickey, and M. G. G. Foreman, 2005: Transport of surface waters from the Juan de Fuca eddy region to the Washington coast. *Cont. Shelf Res.*, **25**, 2008–2021.

Mackas, D. L., K. L. Denman, and A. F. Bennett, 1987: Least squares multiple tracer analysis of water mass composition. *J. Geophys. Res.*, **92 (C3)**, 2907–2918.

Marchesiello, P., J. C. McWilliams, and A. Shchepetkin, 2001: Open boundary conditions for long-term integration of regional oceanic models. *Ocean Modelling*, **3**, 1–20.

Marchesiello, P., J. C. McWilliams, and A. Shchepetkin, 2003: Equilibrium structure and dynamics of the California Current System. *J. Phys. Oceanogr.*, **33**, 753–783.

Mass, C. F., et al., 2003: Regional environmental prediction over the Pacific Northwest. *Bull. Amer. Meteor. Soc.*, **84**, 1353–1366.

McClatchie, S., R. Goericke, R. Cosgrove, G. Auad, and R. Vetter, 2010: Oxygen in the Southern California Bight: Multidecadal trends and implications for demersal fisheries. *Geophys. Res. Lett.*, **37**, L19 602, doi:10.1029/2010GL044497.

McCreary, J. P. and S.-Y. Chao, 1985: Three-dimensional shelf circulation along an eastern ocean boundary. *J. Mar. Res.*, **43**, 13–36.

McCreary, J. P., Jr., 1981: A linear stratified model of the coastal undercurrent. *Phil. Trans. R. Soc. Lond.*, **A302**, 385–413.

McManus, D. A., 1972: Bottom topography and sediment texture near the Columbia River mouth. *The Columbia River Estuary and Adjacent Ocean Waters*, A. T. Pruter and D. L. Alverson, Eds., University of Washington Press, 241–253.

Mellor, G. L., 1986: Numerical simulation and analysis of the mean coastal circulation off California. *Cont. Shelf Res.*, **6**, 689–713.

Middelburg, J. J., K. Soetaert, P. M. J. Herman, and C. H. R. Heip, 1996: Denitrification in marine sediments: A model study. *Global Biogeochem. Cycles*, **10**, 661–673, doi:10.1029/96GB02562.

Mirshak, R. and S. E. Allen, 2005: Spin-up and the effects of a submarine canyon: Applications to upwelling in astoria canyon. *J. Geophys. Res.*, **110**, C02 013.

Miyasaka, T. and H. Nakamura, 2005: Structure and formation mechanisms of the northern hemisphere summertime subtropical highs. *J. Climate*, **18**, 5046–5065.

Monteiro, P. M. S., A. van der Plas, V. Morholz, A. Pascall, and W. Joubert, 2006: Variability of natural hypoxia and methane in a coastal upwelling system: Oceanic physics or shelf biology? *Geophys. Res. Letts.*, **33**, L16 614, doi:10.1029/2006GL026 234.

Muraki, H., 1974: Poleward shift of the coastal upwelling region off the California coast. *J. Oceanogr. Soc. Jpn.*, **30**, 49–53.

Naqvi, S. W. A., H. Naik, D. A. Jayakumar, M. S. Shailaja, and P. V. Narvekar, 2006: Seasonal oxygen deficiency over the western continental shelf of India. *Past and Present Water Column Anoxia*, L. N. Neretin, Ed., Springer, 195–224.

Nittrouer, C. A., 1978: The process of detrital sediment accumulation in a continental shelf environment: An examination of the Washington shelf. Ph.D. thesis, University of Washington, 243 pp.

North, E. W., Z. Schlag, R. R. Hood, M. Li, L. Zhong, T. Gross, and V. S. Kennedy, 2008: Vertical swimming behavior influences the dispersal of simulated oyster larvae in a coupled particle tracking and hydrodynamic model of Chesapeake Bay. *Mar. Ecol. Prog. Ser*, **359**, 99–115.

Oey, L.-Y., 1999: A forcing mechanism for the poleward flow off the southern California coast. *J. Geophys. Res.*, **104**, 13 529–13 539.

Pares-Sierra, A. and J. J. O'Brien, 1989: The seasonal and interannual variability of the California Current system: A numerical model. *J. Geophys. Res.*, **94**, 3159–3180.

Pauly, D. and V. Christensen, 1995: Primary production required to sustain global fisheries. *Nature*, **374**, 255–257.

Pelland, N. A., C. C. Eriksen, and C. M. Lee, 2012: Subthermocline eddies over the Washington continental slope as observed by Seagliders, 2003-09, submitted to *J. Phys. Oceanogr.*

Perry, M. J., J. P. Bolger, and D. C. English, 1989: Primary production in Washington coastal waters. *Coastal oceanography of Washington and Oregon*, M. R. Landry and B. M. Hickey, Eds., Elsevier, 117–138.

Philander, S. G. H. and J.-H. Yoon, 1982: Eastern boundary currents and coastal upwelling. *J. Phys. Oceanogr.*, **12**, 862–879.

Pierce, S. D., J. A. Barth, R. K. Shearman, and A. Y. Erofeev, 2012: Declining oxygen in the Northeast Pacific. *J. Phys. Oceanogr.*, **42**, 495–501.

Pierce, S. D., J. A. Barth, R. E. Thomas, and G. W. Fleischer, 2006: Anomalously warm July 2005 in the northern California Current: Historical context and the significance of cumulative wind stress. *Geophys. Res. Letts.*, **33**, L22S04, doi:10.1029/2006GL027149.

Pierce, S. D., R. L. Smith, P. M. Kosro, J. A. Barth, and C. D. Wilson, 2000: Continuity of the poleward undercurrent along the eastern boundary of the mid-latitude north Pacific. *Deep-Sea Res.*, **47**, 811–829.

Pringle, J. M. and E. P. Dever, 2009: Dynamics of wind-driven upwelling and relaxation between Monterey Bay and Point Arena: Local-, regional-, and gyre-scale controls. *J. Geophys. Res.*, **114**, C07003, doi:10.1029/2008JC005016.

Reid, J. L. and A. W. Mantyla, 1976: The effect of the geostrophic flow upon coastal sea elevations in the northern North Pacific Ocean. *J. Geophys. Res.*, **81**, 3100–3110.

Ricker, W. E., 1984: Computation and uses of central trend lines. *Can. J. Zool.*, **62**.

Rivas, D. and R. M. Samelson, 2011: A numerical modeling study of the upwelling source waters along the Oregon coast during 2005. *J. Phys. Oceanogr.*, **41**, 88–112.

Robinson, C., O. Serret, G. Tilstone, E. Teira, M. V. Zubkov, A. P. Rees, and E. M. S. Woodward, 2002: Plankton respiration in the Eastern Atlantic Ocean. *Deep Sea Res. I*, **49**, 787–813.

Rykaczewski, R. R. and J. P. Dunne, 2010: Enhanced nutrient supply to the California Current Ecosystem with global warming and increased stratification in an earth system model. *Geophys. Res. Lett.*, **37**, L21606, doi:10.1029/2010GL045019.

Ryther, J. H., 1969: Photosynthesis and fish production in the sea. *Science*, **166**, 72–76.

Schulman, I., J. C. Kindle, S. deRada, S. C. Anderson, B. Penta, and P. J. Martin, 2003: Development of a hierarchy of nested models to study the California Current system. *Proc. Eighth International Conf., Estuarine and Coastal Modeling*, M. L. Spaulding, Ed., ASCE, 74–87.

Schwing, F. B., N. A. Bond, S. J. Bograd, T. Mitchell, M. A. Alexander, and N. Mantua, 2006: Delayed coastal upwelling along the U.S. West Coast in 2005: A historical perspective. *Geophys. Res. Lett.*, **33**, L22S01, doi:10.1029/2006GL026911.

Schwing, F. B., M. O. Farrell, J. M. Steger, and K. Baltz, 1996: Coastal upwelling indices, West Coast of North America, 1946–1995. Tech. Rep. NOAA-TM-NMFS-SWFSC-231, NOAA, 144 pp.

Schwing, F. B. and R. Mendelssohn, 1997: Increased coastal upwelling in the California Current System. *J. Geophys. Res.*, **102 (C2)**, 3421–3438, doi:10.1029/96JC03591.

Shchepetkin, A. F. and J. C. McWilliams, 2005: The regional oceanic modeling system (ROMS): a split-explicit, free-surface, topography-following-coordinate oceanic model. *Ocean Modelling*, **9**, 347 – 404.

She, J. and J. M. Klinck, 2000: Flow near submarine canyons driven by constant winds. *J. Geophys. Res.*, **105 (C12)**, 28 671–28 694.

Siedlecki, S. A., A. Mahadevan, and D. E. Archer, 2012: Mechanism for export of sediment-derived iron in an upwelling regime. *Geophys. Res. Lett.*, **39 (3)**, L03601, doi: 10.1029/2011GL050366.

Smith, P. and K. Bogren, 2001: Determination of nitrate and/or nitrite in brackish or seawater by flow injection analysis colorimeter. QuickChem® Method 31-107-04-1-E, Lachat Instruments, 12 pp., Milwaukee, WI.

Smith, R. L., 1981: A comparison of the structure and variability of the flow field in three coastal upwelling regions: Oregon, Northwest Africa, and Peru. *Coastal Upwelling*, F. A. Richards, Ed., American Geophysical Union, Washington, D. C., 107–118.

Song, Y. and D. Haidvogel, 1994: A semi-implicit ocean circulation model using a generalized topography-following coordinate system. *Journal of Computational Physics*, **115**, 228–244.

Strub, P. and C. James, 2000: Altimeter-derived variability of surface velocities in the California Current System: 2. seasonal circulation and eddy statistics. *Deep Sea Res. II*, **47**, 831–870.

Strub, P. T., J. S. Allen, A. Huyer, and R. L. Smith, 1987: Large-scale structure of the spring transition in the coastal ocean over western North America. *J. Geophys. Res.*, **92**, 1527–1544.

Suginohara, N., 1974: Onset of coastal upwelling in a two-layer ocean by wind stress with longshore variation. *Journal of Oceanography*, **30**, 23–33, 10.1007/BF02112888.

Suginohara, N., 1982: Coastal upwelling: Onshore–offshore circulation, equatorward coastal jet and poleward undercurrent over a continental shelf-slope. *J. Phys. Oceanogr.*, **12**, 272–284.

Suginohara, N. and Y. Kitamura, 1984: Long-term coastal upwelling over a continental shelf–slope. *J. Phys. Oceanogr.*, **14**, 1095–1104.

Sutherland, D. A., P. MacCready, N. S. Banas, and L. F. Smedstad, 2011: A model study of the Salish Sea estuarine circulation. *J. Phys. Oceanogr.*, **41**, 1125–1143.

Sverdrup, H. U., M. W. Johnson, and R. H. Fleming, 1942: *The Oceans, Their Physics, Chemistry, and General Biology*. New York: Prentice-Hall, 1087 pp.

Swartzman, G., B. Hickey, P. M. Kosro, and C. Wilson, 2005: Poleward and equatorward currents in the Pacific Eastern Boundary Current in summer 1995 and 1998 and their relationship to the distribution of euphausiids. *Deep-Sea Res. II*, **52**, 73–88.

Thomas, A. C. and P. Brickley, 2006: Satellite measurements of chlorophyll distribution during spring 2005 in the California Current. *Geophys. Res. Letts.*, **33**, L22S05, doi:10.1029/2006GL026 588.

Thomson, R. E. and M. V. Krassovski, 2010: Poleward reach of the California Undercurrent extension. *J. Geophys. Res.*, **115**, C09027, doi:10.1029/2010JC006280.

Tinis, S. W., R. E. Thomson, C. F. Mass, and B. M. Hickey, 2006: Comparison of MM5 and meteorological buoy winds from British Columbia to Northern California. *Atmos. Ocean.*, **44**, 65–81.

Todd, R. E., D. L. Rudnick, M. R. Mazloff, R. E. Davis, and B. D. Cornuelle, 2011: Poleward flows in the southern California Current System: Glider observations and numerical simulation. *J. Geophys. Res.*, **116 (C2)**, C02026, doi:10.1029/2010JC006536.

Trowbridge, J. H., D. C. Chapman, and J. Candela, 1998: Topographic effects, straits and the bottom boundary layer. *The Sea*, K. H. Brink and A. R. Robinson, Eds., John Wiley and Sons, Inc., Vol. 11, 63–88.

Umlauf, L. and H. Burchard, 2003: A generic length-scale equation for geophysical turbulence models. *J. Mar. Res.*, **61**, 235–265.

Walsh, J. J., 1981: A carbon budget for overfishing off Peru. *Nature*, **290**, 300–304.

Wang, D. P. and C. N. K. Mooers, 1976: Coastal-trapped waves in a continuously stratified ocean. *J. Phys. Oceanogr.*, **6**, 853–863.

Ware, D. M. and R. E. Thomson, 2005: Bottom-up ecosystem trophic dynamics determine fish production in the northeast Pacific. *Science*, **308**, 1280–1284.

Waterhouse, A. F., S. E. Allen, and A. W. Bowie, 2009: Upwelling flow dynamics in long canyons at low Rossby number. *J. Geophys. Res.*, **114**, C05004, doi: 10.1029/2008JC004956.

Welschmeyer, N. A., 1994: Fluorometric analysis of chlorophyll *a* in the presence of chlorophyll *b* and pheopigments. *Limnol. Oceanogr.*, **39**, 1985–1992.

Werner, F. E. and B. M. Hickey, 1983: The role of a longshore pressure gradient in Pacific Northwest coastal dynamics. *J. Phys. Oceanogr.*, **13**, 395–410.

Whitney, F. A., H. J. Freeland, and M. Robert, 2007: Persistently declining oxygen levels in the interior waters of the eastern subarctic Pacific. *Prog. Oceanogr.*, **75**, 179–199.

Willmott, C. J., 1981: On the validation of models. *Phys. Geogr.*, **2**, 184–194.

Wyrtki, K., 1975: Fluctuations of the dynamic topography in the Pacific Ocean. *J. Phys. Oceanogr.*, **5**, 450–459.

Yoshida, K., 1955: Coastal upwelling off the California coast. *Rec. Oceanogr. Works Jpn.*, **2 (2)**, 8–20.

Yoshida, K., 1967: Circulation in the eastern tropical oceans with special references to upwelling and undercurrents. *Jap. J. Geophys.*, **4**, 1–75.

Yoshida, K., 1980: The coastal undercurrent – A role of longshore scales in coastal upwelling dynamics. *Prog. Oceanogr.*, **9**, 83–131.

VITA

Thomas Connolly was born in New York, NY in 1980. His interest in science and mathematics developed during high school in the suburbs of Philadelphia, PA. He was introduced to fluid mechanics and oceanography while pursuing a Bachelor of Science in Environmental Engineering at Stanford University. Before coming to Seattle for graduate school, he worked as a surf instructor, sea kayak guide, marine naturalist, and more while living in Delphi, Ireland and Monterey, CA. In 2012, he earned a doctor of philosophy at the University of Washington in Oceanography, and was awarded a United States Geological Survey postdoctoral scholarship at the Woods Hole Oceanographic Institution.